SOLIDIFICATION OF IRON BASE ALLOYS
AT LARGE DEGREES OF UNDERCOOLING

INTERIM REPORT

AMMRC CR 69-14/1

by

W. E. Brower, Jr. and M. C. Flemings

for

Contract Period

January, 1968 - January, 1969

Department of Metallurgy
Massachusetts Institute of Technology
Cambridge, Massachusetts   02139

July 15, 1969

DA-46-68-C-0044

U. S. Army Materials and Mechanics Center
Watertown, Massachusetts   02172

SOLIDIFICATION OF IRON BASE ALLOYS
AT LARGE DEGREES OF UNDERCOOLING

INTERIM REPORT

AMMRC CR 69-14/1

by

W. E. Brower, Jr. and M. C. Flemings

for

Contract Period

January, 1968 - January, 1969

Department of Metallurgy
Massachusetts Institute of Technology
Cambridge, Massachusetts 02139

July 15, 1969

DA-46-68-C-0044

U. S. Army Materials and Mechanics Center
Watertown, Massachusetts 02172

ABSTRACT

A levitation melting and splat cooling apparatus has been modified to permit chill casting and liquid quenching. It was utilized in this work to investigate the effect of cooling rate on solidification structure and mechanical behavior of iron base alloys.

The degree of microstructural refinement of several alloys was determined quantitatively and qualitatively over a range of cooling rates from $1°C$/second to $10^6°C$/second. Alloys studied include Fe-25% Ni, 440C, 4330, Fe-4.3%C, Fe containing SiO_2 inclusions and Fe containing FeO inclusions.

SiO_2 inclusions in Fe alloy were observed to be measurably coarsened after isothermal solid state heat treatment at $1400°C$.

The fracture behavior of inclusion bearing pure iron was investigated using the scanning electron microscope. Studies were on two alloys, Fe containing SiO_2 inclusions, and Fe containing FeO inclusions. In both alloys, the ductile fracture surface revealed dimples containing spherical inclusions. Extreme inclusion-matrix interface separation giving a "ball in a trough" appearance resulted from a rotational deformation mode during necking down of the test bar. Dimples immediately associated with the inclusions were smaller the smaller the inclusion. Fracture surfaces of the two alloys were similar. Microcracks associated with FeO inclusions in the Fe-0.07% O alloy were observed in the as-cast structure, while no microcracks associated with the SiO_2 inclusions in the Fe-0.05% Si alloy were observed in the as-cast structure.

FeO inclusions exhibit shrinkage cavities. These result because the inclusions form as a liquid and solidify after the iron. Inclusion-matrix separation of FeO inclusions is also observed because of contraction of the FeO inclusions on cooling. Shrinkage cavities or inclusion-matrix separations were not observed in the alloy containing SiO_2 inclusions (in the as-cast condition). Inclusion-matrix separation was, however, observed for both types of inclusions in the plastically deformed region of a test bar after testing.

TABLE OF CONTENTS

LIST OF ILLUSTRATIONS

LIST OF TABLES

INTRODUCTION

This report summarizes one of several related research activities on inclusions at Massachusetts Institute of Technology. The work is primarily on levitation melted and rapidly solidified (including splat-cooled) samples. It deals with effects of solidification variables on (1) dendrite and inclusion structures, (2) influence of high temperature homogenization treatments on inclusions, and (3) influence of inclusions on fracture behavior of iron.

The work is an outgrowth of a program on undercooled iron base alloys, that has had important technological, as well as fundamental, findings. A most important fundamental result has been that structure coarsening ("ripening") determines final dendrite arm spacing in both undercooled melts and in usual commercial castings and ingots. Dendrite arm spacing is of major importance in determining properties of castings and of wrought material produced from cast ingots and so determination of the mechanism of establishment of dendrite arm spacing has been of considerable applied as well theoretical interest.

Most recent work on this program, prior to that reported herein, has been on extension of the dendrite coarsening ideas to inclusion morphology and growth. This work has shown that inclusions coarsen (Ostwald ripen) during solidification, just as do dendrites. Inclusions also are "pushed" by growing dendrites, and float, join and coalesce during

solidification. Initial work has been reported[4] and continuing work will be summarized in a later report. Work to date has been primarily on iron-copper alloys with silica inclusions.

Chapter I deals with effects of cooling rate on dendrite and inclusion structure. A levitation melting, undercooling, and splat cooling device is employed in this work. Design and construction of the unit are described herein; portions of this description have been given in the previous annual contract report[4]. Some particularly interesting results from this work include the linear relationship, on log-log scale, extending over many orders of magnitude, between dendrite arm spacing and cooling rate (Figures 14 and 15) and between inclusion diameter and cooling rate (Figure 22).

Chapter II deals with isothermal coarsening of SiO_2 inclusions in nearly pure iron. It is of interest that appreciable coarsening of these inclusions occurs after a relatively few hours at 1400°C. This is approximately the temperature used in long time heat treatments by Quigley and Ahearn. It therefore seems probable that some of the beneficial effects of these high temperature heat treatments on properties are due to their influence on inclusions.

Chapter III summarizes work on mechanical behavior of several inclusion bearing irons. This chapter includes a number of scanning electron micrographs of fracture surfaces and polished sections, showing

inclusions and relation of inclusions to fracture. Inclusions were found in a large fraction of the dimples on all fracture surfaces (e.g., Figure 2, Chapter III). An interesting difference between FeO and SiO_2 inclusions in as-cast material was shown to be that the FeO inclusions exhibit solidification shrinkage cavities and tend to pull away from the matrix during cooling (e.g., Figure 11, Chapter III).

REFERENCES

1. Castings and Solidification Section, Department of Metallurgy, M.I.T., "Solidification of Iron Base Alloys at Large Degrees of Undercooling", U. S. Army Materials Research Agency, Contract No. DA-19-020-AMC-0231(X), Interim Report, October 1, 1963-September 30, 1964.

2. T. Z. Kattamis, M. C. Flemings, "Solidification of Iron Base Alloys at Large Degrees of Undercooling", U. S. Army Materials Research Agency, Contract No. DA-19-020-AMC-0231(X), Interim Report, October 1, 1964-September 30, 1965.

3. T. Z. Kattamis, M. C. Flemings, "Solidification of Iron Base Alloys at Large Degrees of Undercooling", U. S. Army Materials Research Agency, Contract No. DA-19-020-AMC-0231(X), Interim Report, October 1, 1965-September 30, 1966.

4. M. C. Flemings, M. Myers, and W. E. Brower, Jr., "Solidification of Iron Base Alloys at Large Degrees of Undercooling", U.S. Army Materials and Mechanics Research Center, Contract No. DA-19-020-AMC-0231(X), Interim Report, October 1, 1966-December 31, 1967.

5. T. Z. Kattamis, M. C. Flemings, "Dendrite Structure and Grain Size of Undercooled Melts", Trans. Met. Soc. AIME, November, 1966, pp. 1523-1532.

6. T. Z. Kattamis, M. C. Flemings, "Solidification of Highly Undercooled Castings", Trans. AFS, Vol. 75, 1967, pp. 191-198.

7. T. Z. Kattamis, M. C. Flemings, "Structure of Undercooled Eutectics", to be published.

Chapter I

VARIATION OF STRUCTURE WITH COOLING RATE

Introduction and Literature Survey

Interest in higher cooling rates during solidification has led in recent years to the development of a quenching technique known as splat cooling, reviewed in Duwez's Cambell Memorial Lecture[1]. Duwez and co-workers have investigated many alloy systems by the "shock tube" technique of splat cooling[2,3,4,5]. Predecki has measured[6] and Ruhl has calculated[7] the cooling rates during splat cooling by the shock tube method to be 10^7-10^9 °C/sec. Non-equilibrium structures that result from this technique are either non-equilibrium single phase alloys, i.e., extended solid solubility[2], single phase eutectic alloys[3], or new non-equilibrium phases unobtainable for the given alloy by slower quenching techniques, i.e., new intermetallic compounds[4] and amorphous metal alloys[5]. Ruhl and Cohen[8] have produced a new phase in the iron-carbon system using the shock tube technique. The splat resulting from this technique is a layer of small flakes approximately one micron thick. In general, this type of splat, although extremely well suited to X-ray and electron diffraction analysis, is not suitable for optical microscopy or mechanical testing in the as cast condition.

The other predominant splat cooling technique, used in this work, is the "hammer and anvil" technique which results in approximately a one inch diameter by 100 micron thick disc. Strachan has measured the cooling rate during splat cooling in the hammer and anvil device used in this work to be on the order of 10^6 °C/sec.[9]. The hammer and anvil yields a splat

that is 100 times slower cooled but 100 times larger than the product of
the shock tube. Both optical microscopy and mechanical property measure-
ments can be performed on the hammer and anvil type splat. Some examples
of non-equilibrium structures that have been obtained from the hammer and
anvil splat cooler are: amorphous Fe-C-P alloys[10], single phase Ni-32%Sn
eutectic alloy[11] and extension of the equilibrium solid soludility of
copper in silver[12]. Ruhl and Cohen's epsilon phase in the iron-carbon
system, however, was unobtainable on the hammer and anvil type splat cooler
used in this work.

The main goal of the splat cooling technique employed in this
research was the achievement of ultra-fine dendrite structures and
inclusions as compared with slowly solidified structures. Refinement of
dendrite structure has been shown, for several alloys, to be solely a
function of cooling rate (or "local solidification time")[13], and hence the
only way to achieve ultra-fine structures is, apparently, by very fast
cooling.

Fine dendrite arm spacings in cast alloys are desirable, since
it has been shown that the homogenization time for an alloy with non-
equilibrium solute segregation is proportional to the square of the
secondary dendrite arm spacing[14]. It is also known that the mechanical
properties of a heat treated casting depend on the homogeniety obtained[15,16,17].
Furthermore, as cast segregation is present in wrought material and is
deleterious to properties[18,19]. Dendrite arm spacings ranging from 50
microns down to less than 1 micron have been achieved with the increased
cooling rates available in the present apparatus. Segregation in the
form of non-metallic inclusions is also refined by higher cooling rates.

To establish continuous trends of structural variation with cooling rate, solidification techniques with cooling rates intermediate between conventionally solidified, slowly cooled large castings and ultra rapidly cooled splats were utilized. This necessitated a redesigning of the existing levitation melting and splat cooling unit. Small thin plate chill castings, although extremely finely structured, have much coarser structures and have over an order of magnitude slower cooling rate than the splats. Chill casting capability was therefore incorporated into the levitation melting and splat cooling apparatus. Still coarser structures and slower cooling rates result from liquid quenching of the molten levitated charge. The ability to replace the splat cooler with a liquid quench tank in the redesigned apparatus yields a quenching technique with a cooling rate intermediate between that of chill casting and conventional slow solidification. With these four quenching techniques available-- conventional casting, liquid quenching, chill casting, and splat cooling-- continual refinement of solidification structures may be studied over six orders of magnitude of cooling rate, $1^{\circ}C/sec.$ to 10^{6} $^{\circ}C/sec.$

Apparatus-General

Extensive work was done to modify and extend the capabilities of an existing levitation melting unit. This work was primarily to (1) improve the vacuum system and purity of cooling gases employed, (2) incorporate ability to make chill plate castings and to liquid quench the molten droplets, and (3) permit making up to five separate runs without breaking vacuum. The capabilities of the apparatus include the following:

1. Ferrous metals or alloys can be levitation melted in amounts up to about 3 grams in vacuum or controlled atmosphere. A wide variety of other metals can also be so melted.

2. Samples can be held molten or partially molten for long periods (e.g., in excess of 1/2 hour). Large superheats can be obtained (in excess of $600^{\circ}C$). Large undercoolings can be achieved (as much as $300^{\circ}C$ under the melting point).

3. Alloying can be accomplished by simultaneously melting two or more charge materials (while levitated) or by reaction of the charge with a controlled atmosphere. Alternately, the charge can be pre-alloyed in the vacuum induction furnace.

4. Up to five separate melting and casting runs can be made without opening the apparatus to the atmosphere.

5. The metal charge can be solidified by (a) slow controlled cooling in the levitation coil, (b) liquid quenching, (c) casting in thin section ingot molds, and (d) "splat cooling".

6. Interrupted solidification experiments can be conducted by, for example, partially solidifying the sample (slowly) in the coil and then rapidly solidifying the remainder by liquid quenching or splat cooling.

The basic levitation melter employed has been previously described[20]; it is based on the work of Comenetz and others[21]. The "hammer and anvil" splat cooling device has also been previously described[9]. The propulsion of the hammer is electromagnetic. A large current is released for a short time through a "pancake" coil adjacent to a driving disc. The driving disc is then repulsed from the coil with a force that may be calculated from magnetodynamic principles. In the splatter the force achievable is 2200 to 6600 pounds; resulting platen velocity is 1000 to 3000 cm/sec. (33 to 100 ft/sec.). Remaining portions of the apparatus have been constructed in the course of this research and are described in the following sections.

Figure 1 is an overall sketch of the levitation melting and quenching apparatus, and Figure 2 (top) a photograph of the apparatus, including power supply. Descriptions are given below of the melting, temperature measuring, atmosphere controlling, gas quenching, liquid quenching, chill casting, and splat quenching systems. Figures 3-7 show details of some of these systems.

Levitation System

The levitation melter constructed for this work was designed to be operated with a 10 KW, 400 K.C. Lepel High Frequency Generator. This power source is capable of an output of approximately 300 amperes into a suitable impedance load, but is limited to less than this into the relatively

low inductance levitation coil. Figure 3 shows a levitation coil of the type presently in use; it is made from 1/8 inch diameter, thin wall copper tubing.

The most practical technique for temperature control during levitation involves flowing a stream of cooling gas over the levitated charge. This is readily done by winding a levitation coil, such as the one in Figure 3, around a Vycor tube of large enough diameter to contain the specimen, and then flowing cooling gas vertically up the tube.

To obtain good "matching" to the generator and to increase the circulating current in the coil, a capacitor bank (Lepel CT-25-4) was inserted into the output circuit in parallel with the levitation coil. The coil and the capacitor bank form a resonant circuit, having a large circulating current, measured to be over 650 amperes at full power. Physically, the capacitor is located close to the levitation coil and they are connected using co-axial power leads to minimize power losses. A schematic diagram of the external electrical circuit is given in Figure

The enclosure containing charges and ingot molds is shown schematically in Figure 1. This enclosure is a duplicate of that designed by Yarwood[27] except modified for splatting, as described below. Up to five charges are placed in each charge container prior to evacuating the system. The charge container is of boron nitride to prevent its being heated when raised into the levitation coil. Charging is accomplished by first rotating the turntable into position so one of the five charges is directly beneath the vertical glass tube. Next, the charge and charge container are raised up into the levitation coil by pushing on a vertical pushrod which extends out the bottom of the box. This pushrod also serves as a "charge exit port" for splatting and is so named in the sketch. An "O" ring seal between the pushrod and enclosure allows the lateral motion

while maintaining vacuum or slight positive pressure in the enclosure.

The turntable also contains up to five ingot molds. To cast one of these, it is simply rotated under the coil while the droplet is levitated. The power is turned off and metal dropped into the plate. To "splat" a sample, one of the locations for an ingot mold is left vacant, and this location placed under the levitated drop. When the levitation power is turned off, the droplet passes through the hole, down the hollow "pushrod-charge exit port", and through a plastic sheet sealed at the base of the exit port. This sheet plastic seal covers a 5/8" hole; vacuum or positive pressure is again maintained by an "O" ring seal. The seal is "Saran Wrap" (polyvinylidene chloride copolymerized with polyvinyl chloride); it is sufficiently strong to resist atmospheric pressure while the enclosure is fully evacuated, but rapidly melts as the falling hot drop approaches it.

The temperature of the levitated droplet is monitored using a Milletron Two-Color Pyrometer, Model TSA. Its accuracy varies with the material whose temperature is being measured, but has been found in this work (and with this system) to be accurate on absolute measurements on liquid iron and steel to within $\pm$ 20°C and to within $\pm$ 10°C relative to the measured melting point. Output is read on a meter in the control unit, and may be recorded on an external chart recorder. A schematic diagram of the temperature measuring system is shown in Figure 5. Sighting of the optical pyrometer is done from the top of the levitation coil through a right angle prism and a flat glass disc glued to the top of the glass tube surrounding the specimen. The disc is well above the levitation coil (8 inches) to prevent deposition on it of vapors from the levitated charge.

Controlled Atmosphere and Gas Cooling System

A schematic diagram of the controlled atmosphere and gas cooling system is shown in Figure 6. Evacuation of the system is accomplished by means of mechanical and diffusion pumps, acting through a 1-3/8 inch hole in the bottom of the enclosure containing the charges and ingot molds. A thermocouple vacuum gauge is permanently mounted on the enclosure, and a vacuum ion gauge may be attached to one of the two standard vacuum fittings.

The desired gas atmosphere (or combination of gases) is admitted through copper tubing to flow rate control and solenoid-operated check valves. Ability to admit a large and variable flow rate (up to 250 cubic feet per hour) to the system permits temperature control of the levitated charge. The cooling gas passes up the 5/8 inch I.D. Vycor tube surrounding the levitated specimen and exits through a vacuum released valve. This valve acts as a vacuum seal when the system is evacuated. All connections in the gas flow system are 3/8 inch copper tubing to prevent gas contamination.

Quenching Mechanisms

The various ways summarized below of solidifying the samples permit obtaining cooling rates of the orders of: $1 - 10^{o}C$/sec. for gas quenching; $30 - 200^{o}C$/sec. for liquid quenching, $10^{3} - 10^{4} {}^{o}C$/sec. for chill casting, $10^{5} - 10^{6} {}^{o}C$/sec. for splat cooling.

With sufficiently high flow rates of hydrogen or helium it is possible to solidify a molten levitated charge. At the relatively slow rates of cooling normally involved, the cooling rate may be measured from the chart recorder of the optical pyrometer. This cooling rate simulates

those observed in relatively large castings. As noted previously, quenching into liquid is achieved by placing a liquid quench tank under the charge exit port in place of the splat cooler, and dropping the charge through the plastic seal.

To achieve still higher cooling rates, copper molds with plate-shaped mold cavities of varying thickness are inserted in the turntable in the enclosure in Figure 1 . These copper molds are one inch diameter split cylinders with a wedge or conical shaped riser section above the plate cavity and 1/64 inch vent holes below the plate cavity to aid in mold filling. Plate thicknesses are .03 inches, .05 inches, and .08 inches. For best mold filling, molds are polished each time and minimum superheat of 100°C employed.

An important feature of the arrangement for "splatting" shown in Figure 1 is that the rather delicate levitation melting device and its attachments are physically separate from the necessarily violent clapper (clapping velocities are up to 200 miles per hour).

The drive mechanism for the "hammer and anvil" type splat cooler shown in Figure 7 consists of a driving coil and capacitor energy storage bank, a power supply to charge the capacitor bank, droplet sensing equipment, and spark gap switch with associated trigger circuitry. The capacitor bank and associated power supply are manufactured by EG & G International, Inc. The capacitor bank consists of two separate but equivalent units, Models 524 and 233, each containing capacitors totalling 320 microfarads and having a storage capacity of 2500 joules at 4.0 KV. These two units are connected in parallel, and to the power supply, Model 522, which has a 0 - 4.0 KV adjustable voltage output. The power

supply unit also contains circuitry to provide a voltage pulse output to trigger the spark gap, upon an external contact closure.

The droplet sensor is a Knight photoelectronic relay (kit). A CdSe photocell is located close to the clapper platens, in the line of sight of fall of the molten droplet. When activated by a falling droplet, a relay contact is closed, and through connection with the power supply trigger circuit, provides a voltage pulse to trigger the spark gap. The spark gap unit consists of an EG & G experimental "rail-type" spark gap and an EG & G trigger transformer. The pulse from the power supply is transformed to a much higher voltage, which ionizes the spark gap and causes electrical breakdown, rendering the spark gap conducting, and discharging the capacitor bank into the driving coil.

Upon sensing a falling droplet, the spark gap is triggered and the energy stored in the capacitor bank is released into the driving coil. The large current pulse through the driving coil, associated with the capacitor discharge, creates an intense magnetic field around the coil which in turn induces eddy currents in the aluminum driving disc. The eddy currents cause another magnetic field out of phase with the first. Thus, the driving plate is repelled from the coil at high speed. The capacitor discharge primary pulse lasts approximately 0.1 - 0.2 milliseconds; the moving elements are accelerated to maximum speed during this time.

Operation of the splat cooler and associated equipment is briefly as follows. The clapper platens are cleaned and the moving platen assembly is set in the open position with driving plate against the driving coil. The droplet sensing photocell is inserted into position in the side of the protective cover and the cover is placed over the clapper. After

the induction power is turned on and the specimen levitated, the clapper

power supply is energized to charge the capacitor bank to the desired

voltage. Specimen temperature is manipulated by changing gases or gas

flow rate. When proper conditions have been attained, the induction power

is switched off. The specimen falls and is sensed by the photocell which

triggers the capacitor discharge. The moving platen smashes the falling

specimen against the back platen to form a splat. Total elapsed time

between sensing the specimen by the photocell and splatting is about five

milliseconds.

Cooling Rates During Solidification

As mentioned in the literature survey, Strachan has measured the cooling rate obtained in the splat cooler used in this investigation by use of a photovoltaic cell. A typical cooling curve is shown in Figure 8, yielding a cooling rate from $1500^{\circ}C$ - $1300^{\circ}C$ of 10^6 $^{\circ}C/sec$.

To measure cooling rates during solidification of the plate castings, a small Pt-Pt10%RH thermocouple (Number 38 thermocouple wire) embedded in the side of the plate-shaped cavity of the copper chill molds was used. The output of the thermocouple was recorded on an oscilloscope, giving a cooling curve similar to those obtained in splat cooling, Figure 9. The measured rate from $1500^{\circ}C$ - $1300^{\circ}C$ of $1300^{\circ}C/sec$. of a 0.080 inch thick chill plate casting is necessarily an average value, since as seen by variation of the microstructure of the resulting Fe-25%Ni casting, shown in Figure 10, the cooling rate (as characterized by the secondary dendrite arm spacing) varies over the thickness of the chill casting.

The value of the cooling rate for the type of quenching oil used in this investigation is calculated in Appendix B to be $140^{\circ}C/sec$. As heat transfer from the molten metal drop to the liquid (through a vapor boundary layer) is "h-controlled", Appendix B, the cooling rate is uniform throughout the drop.

During gas quenching in the levitation furnace the output of the optical pyrometer may be displayed on a strip chart recorder. Cooling rates of $1 - 10^{\circ}C/sec$. may be obtained with a sufficiently high (250 SCFH) flow rate of hydrogen or helium.

During solidification in a crucible in the vacuum induction furnace, the output of a Pt-Pt10%Rh thermocouple immersed in the melt is displayed on a strip chart recorder. Cooling rates of 0.1 - 1.5°C/sec. are possible.

Metals and Alloys Studied

The following materials were either studied as received or used as alloying material:

1. Ferrovac "E" Iron, whose chemical analysis as provided by its producer, the Crucible Steel Company, is given in Appendix A, was used as the principal alloying element and was mechanically tested in tension in the as received and completely annealed conditions.

2. Electrolytic nickel, whose chemical analysis is given in Appendix A, was used in the high purity Fe-25%Ni alloy.

3. The following elements and compounds were used in reagent grade purity: Silicon, ferric oxide, carbon, copper, sulfur, and manganese.

4. The chemical analysis of commercial 440C alloy is given in Appendix A.

5. The chemical analysis of commercial 4330 alloy is given in Appendix A.

The following alloys were prepared from the above prime materials in the vacuum induction furnace for use in the levitation furnace: Fe-4.3wt.%C, Fe-0.05wt.%Si, Fe-0.07wt.%O, Fe-Mn-S, Fe-25%Ni-0.05wt.%Si, Fe-25%Ni. The chemical analyses are given in Appendix A.

In addition, high purity Fe-25%Ni alloy was prepared from previously zone-refined Ferrovac "E" iron and electrolytic nickel rods by a "zone alloying" technique in the electron beam furnace. The chemical analysis is given in Appendix A.

RESULTS

Matrix Microstructure, Inclusion Size and Morphology

Several alloys were chosen to demonstrate the relationship of dendrite arm spacing to cooling rate for iron base alloys over a range of cooling rates from that of normal casting of about 1°C/sec. up to that of splat cooling, 10^6 $^{\circ}$C/sec. ("hammer & anvil" technique).

Single phase Fe-25%Ni and multiphase commercial 440C and 4330 alloys were solidified by the four quenching techniques described above. Photomicrographs of the resulting microstructures are shown in Figures 11, 12, and 13. The dendritic solidification morphology of 4330 alloy is shown qualitatively to be refined by higher cooling rates. Plots of the secondary dendrite arm spacing vs. cooling rate are shown in Figures 14 and 15 for Fe-25%Ni[22] and 440C alloy. From the linearity of the log-log-plots, one can see that the secondary dendrite arm spacing is a function only of cooling rate for the alloys studied over six orders of magnitude of cooling rate. Equations of the experimentally determined relationships are as follows:

$$\text{For Fe-25\%Ni, } d = 60\dot{T}^{-0.32} \tag{1}$$

$$\text{For 440C, } d = 82\dot{T}^{-0.41} \tag{2}$$

where d is the secondary dendrite arm spacing in microns and $\dot{T}$ is the cooling rate in $^{\circ}$C/sec.

The variation with cooling rate of the structure of a normally lamellar Fe-4.3%C eutectic alloy (Ledeburite) was also investigated, Figure 16.

A relation of the lamellar spacing to the cooling rate similar to the
dendritic cases was found. The equation of this relationship, shown in
Figure 17 is as follows:

$$\bar{l} = 2.3\dot{T}^{-0.12} \qquad (3)$$

where $\bar{l}$ is the mean lamellar spacing in microns.

Two types of inclusions in iron were investigated over the range
of cooling rates available. An Fe-0.05%Si alloy (Ferrovac "E" plus reagent
grade silicon) and an Fe-0.07%O alloy (Ferrovac "E" plus reagent grade
Fe_2O_3) were prepared in a silica crucible in the vacuum induction furnace.
Both alloys were allowed to come to equilibrium with the silica crucible
at 1550°C for 20 minutes, then solidified at 1.5°C/sec. by turning off the
furnace power. Nucleation occurred after less than 20°C undercooling. The
resulting microstructure of the Fe-0.05%Si alloy, shown in Figure 18
contained, as evidenced by their shape and appearance in white light and
the appearance of the crossed Nicols effect in polarized light, SiO_2 spherical
glassy inclusions. The resulting microstructure of the Fe-O alloy, shown
in Figure 19, contained opaque, grey spherical FeO inclusions. The
equilibrium diagram of the Fe-Si-O system, and the experimental observations
of Forward[26] indicate that the structures obtained are those to be expected
for the two alloys. Pieces of these alloys were then remelted in the
levitation furnace and subsequently liquid quenched, chill cast, and splat
cooled. The resulting microstructures are shown in Figures 19 and 20.

In the Fe-0.07%O master alloy and the oil quenched specimen
spherical FeO inclusions were optically resolvable, Figure 19a and b.
The Fe-0.07%O chill casting, Figure 19c, shows a distribution of spherical
inclusions not completely resolvable at 1000X magnification. The

Fe-0.07%0 splat, Figure 19d, showed no optically resolvable inclusions.
The Fe-0.05%Si master alloy and oil quenched specimen showed spherical
glassy SiO_2 inclusions easily identifiable (Nicols effect) in the optical
microscope, Figure 20a and b. Since the inclusion sizes in the Fe-0.05%Si
chill cast specimens and splats were below optical resolution, electron
microscopy of parlodion replicas of electropolished sections of the
chill casting and splat were used to obtain the microstructures shown
in Figure 20b and c. Although some distribution of inclusion like
particles did appear at 100,000X magnification in the splat, their small
size, about 25 angstroms, and their dissimiliarity to those observed in
the chill casting at 11,000X magnification makes their identification as
SiO_2 inclusions difficult. Therefore, no structural measurements were
attempted on the Fe-0.05%Si splat.

The structural parameters measured by quantitative metallographic
analysis were: the mean inclusion diameter on a polished section, $\bar{d}$;
the number of inclusions per unit area, N_A; and the volume fraction of
inclusions, V_v. For spherical inclusion morphology all other parameters
of interest may be calculated from these three. Table 1 summarizes the
quantative metallographic results for the as cast specimens discussed
here and the coarsened specimens, discussed in a later section.

To measure $\bar{d}$, a size distribution of about 300 measurements of
particle diameters on optical and electron photomicrographs of a polished
section were made and plotted as shown in Figure 21 for the chill cast,
oil quenched, and vacuum induction furnace melted Fe-0.05%Si master alloy.
The magnification was adjusted so that the mean measured diameter would
be about 1mm. The difference between the size distribution of spherical

TABLE 1

QUANTITATIVE METALLOGRAPHY RESULTS

SPECIMEN	NUMBER OF INCLUSIONS MEASURED	MAGNIFICATION	HEAD DIAMETER (MICRONS)	NUMBER PER UNIT AREA	VOLUME FRACTION (%)
SiO_2 Master, As Cast	264	530	2.78	1.3×10^4	0.17
Oil Quench, As Cast	331	1,300	0.528	4×10^6	0.214
Chill Casting, As Cast	393	10,000	0.099	2.8×10^6	0.069
Master, 12 Hours	255	330	3.71	1.2×10^4	0.201
Chill, 12 Hours	226	1,230	0.646	1.67×10^5	
Splat, 12 Hours	413	1,090	0.75	1.84×10^5	
Master, 24 Hours	282	325	4.25	1.21×10^4	0.210
Chill, 24 Hours	367	890	1.04	1.58×10^5	
Splat, 24 Hours	238	1,230	0.755	1.97×10^5	
Master, 48 Hours	282	330	4.05	$1\ 45 \times 10^4$	0.216
Chill, 48 Hours	245	1,150	0.885	1.48×10^5	
Splat, 48 Hours	388	880	0.98	1.48×10^5	
FeO Master, As Cast	315	250	4.37	1.47×10^4	0.174

particles presented on a mechanically polished section and an electro-
polished section will be neglected here.

Bergh & Lindberg[23] have presented a method for conversion of
size distribution of spherical particles determined on a plane polish
to a true three-dimensional size distribution. Appendix C is a demonstra-
tion of the technique on the size distribution of the Fe-0.07%O master
alloy. The mean diameter, $\bar{d}$, on a polished section is raised from 4.4μ
to 5.2μ for the true size distribution. Every measured planar size
distribution will be shifted to higher values of d_i, Figure C-1, in the
true size distribution, and a factor of 1.2 increase in mean diameter
will be assumed to be constant for all specimens. Since the relationship
between $\bar{d}$ and cooling rate, $\dot{T}$, is presented as log $\bar{d}$ vs. log $\dot{T}$ over six
orders of magnitude, errors of even 20% in $\bar{d}$ are not significant.

A plot of log $\bar{d}$ vs. log $\dot{T}$ for the Fe-0.05%Si alloy is shown
in Figure 22. The resulting equation is:

$$\bar{d} = 4.0\dot{T}^{-0.50} \tag{4}$$

Increased cooling rate also affected the volume fraction and
number per unit volume, N_v, of inclusions in the Fe-0.05%Si alloy. The
number of inclusions per unit area, N_A (directly proportional to the
number per unit volume, N_v), was measured directly from the micrographs.
Measurement of volume percent of inclusions was done by a two-dimensional
systematic point count as proposed by Hilliard and Cahn[24]. The volume
fraction of SiO_2 inclusions in the Fe-0.05%Si master alloy and oil quenched
specimen are similar, Table 1, while in the chill casting it is significantly
decreased. Although the volume fraction of SiO_2 in the splat was not
measured, it is presumed to be still further decreased from the equilibrium

value observed in the master alloy and liquid quenched specimen. With
sufficiently high cooling rate, then the equilibrium as cast volume
fraction of inclusions can be surpressed. The N_A of SiO_2 inclusions in
the oil quenched specimen of the Fe-0.05%Si alloy is increased from
the value observed in the master alloy, Table 1. The decreased V_v of
SiO_2 in the chill casting prevents a further increase in N_A over the
oil quenched specimen. Thus the interparticle spacing (inversely
proportional to N_v) is at first decreased, then increased with increasing
cooling rate, due to the combined effects of decreasing inclusion size
and volume fraction.

To demonstrate qualitatively the effect of cooling rate on
other types of inclusions, an Fe-2.0%Mn-1.2%S alloy and a 4330 low alloy
commercial steel were solidified by the four quenching techniques available.
The concentrations of Mn and S in the Fe-Mn-S alloy were chosen so that
only stoichiometric MnS inclusions would precipitate upon solidification.
The microstructures of the Fe-Mn-S master alloy, oil quenched specimen,
chill casting, and splat are shown in Figure 23. Similarly, the unetched
microstructure of 4330 alloy is shown in Figure 24. As can be seen, the
inclusions in both alloys are refined by increased cooling rate. In both
alloys a tendency toward more spherical inclusion morphology is observed
with increased cooling rate. In the Fe-Mn-S alloy the inclusion morphology
changes from wholly dendritic in the master alloy to wholly spherical in
the chill casting, Figure 23.

Using the same procedure as was used for the Fe-0.05%Si alloy,
an Fe-25%Ni-0.05%Si alloy was cast in a silica crucible in the vacuum
induction furnace. Reagent grade purity silicon was added to the high

purity "zone alloyed" Fe-25%Ni alloy yielding a matrix with clearly defined

solute dendrites and only pure SiO_2 inclusions. Microstructures of the

master alloy, oil quenched specimen, chill casting, and splat are shown

in Figure 25. In the structure of the Fe-0.05%Si alloy no clustering of

SiO_2 inclusions is ever observed, Figure 20. In the structure of the

Fe-25%Ni-0.05%Si alloy, where the dendrites solidify over a wider temperature

range, the result of solute dendrites is pronounced clustering of SiO_2

inclusions, Figure 25. Roughly the same amount of undercooling occurred

in each master alloy, $20^{\circ}C$, as measured by the thermocouple immersed in

the melt. As can be seen, both the matrix and the inclusions are refined

by the higher cooling rates.

Discussion

The microstructures investigated herein are necessarily end products of the various solidification processes. Matrix and inclusion structures occurring at the early stages of solidification are not necessarily observed here; only the effect of the final victor(s) in the competition of the structure determining factors has been observed. The slow cooled master alloys of the Fe-25%Ni, 440C, and 4330 alloys are all so coarse that the original dendritic microstructure is hardly recognizable at high magnification, Figures 11, 12, and 13. In the oil quenched specimens and chill castings the dendritic structures become more refined and well defined. The splat structures appear as rod-like dendrites for the Fe-25%Ni and 440C alloys, and equiaxed for the 4330 alloy. The lamellar eutectic structure of the Fe-4.3%C alloy, Figure 16, is simply refined to finer lamellar spacing with higher cooling rates.

The FeO and SiO_2 inclusions in Figures 19 and 20 are refined from 3-5 microns diameter in the master alloy to submicron sizes in the faster quenched specimens. Qualitatively similar trends are observed for the inclusions in the Fe-Mn-S and 4330 alloys, Figures 23 and 24. Refinement of both dendrites and inclusions is observed in Figure 25 for the Fe-25%Ni-0.05%Si alloy.

The linearity of the plots of log structure parameter (for solute dendrites, inclusions, and lamellar eutectic) vs. log cooling rate indicates that the same factor is determining the final solidification structure over the range of cooling rates observed. As demonstrated by the isothermal holding in the liquid-solid region experiments of Coughlin, Kattamis, and Flemings[25], this structure determining factor is coarsening kinetics. The driving force for coarsening kinetics is the reduction

of surface energy[25]. Thus, the original finely branched dendrite or small inclusion that grows into the undercooled liquid eventually reduces its free energy by reducing its surface area. The result is a larger dendrite arm spacing or a larger mean inclusion size.

REFERENCES

1. P. Duwez, "Structure and Properties of Alloys Rapidly Quenched From the Liquid State", Trans. of the ASM, v. 60, 1967, pp. 605-633.

2. H. Lou, and P. Duwez, "Face Centered Cubic Cobalt-Rich Solid Solutions in Binary Alloys with Aluminum, Gallium, Silicon, Germanium, and Tin" Canadian Journal of Physics, v. 41, 1963, pp. 758-761.

3. P. Duwez, R. H. Willens, and W. Klement, Jr., "Continuous Series of Metastable Solid Solutions in Silver-Copper Alloys", J. Appl. Phys., v. 31, 1960, p. 1136.

4. C. C. Chou, H. L. Lou, and P. Duwez, "CsCl-Type Compounds in Binary Alloys of Rare-Earth Metals with Gold and Silver", Journal of Applied Physics, v. 34, No. 7, 1963, pp. 1971-1973.

5. H. L. Lou and P. Duwez, "Metastable Amorphous Phases in Tellurium Base Alloys", Applied Physics Letters, v. 2, No. 1, 1963, p. 21.

6. P. Predecki, A. W. Mullendore, and N. J. Grant, "A Study of the Splat Cooling Technique", Trans. Met. Soc. AIME, v. 233, 1965, pp. 1581-1586.

7. R. C. Ruhl, "Cooling Rates in Splat Cooling", Materials Science and Engineering, 1 (1967), pp. 313-320.

8. R. C. Ruhl and M. Cohen, "Splat Quenching of Iron-Carbon Alloys", Trans. Met. Soc. AIME, v. 245, 1969, pp. 241-253.

9. R. W. Strachan, "A Technique for Levitation Melting, Undercooling, and Splat Cooling of Metals and Alloys", Ph.D. Thesis, Dept. of Metallurgy, M.I.T., 1967.

10. P. Duwez and S. C. H. Lin, "Amorphous Ferromagnetic Phase in Iron-Carbon-Phosphorous Alloys", U. S. Atomic Energy Commission Report, 1967.

11. ibid. (9)

12. R. K. Linde, "Kinetics of Transformation of Metastable Silver-Copper Solid Solutions Quenched from the Liquid State", Transactions AIME, v. 236, Jan. 1966, pp. 58-64.

13. H. Matyja, B. C. Giessen, and N. J. Grant, "Effect of Cooling Rate on Dendrite Spacing in Aluminum Alloys", to be published.

14. M. C. Flemings, Solidification Processing class notes.

15. M. C. Flemings: Proceedings Twelfth Sagamore Army Materials Research Conference, August 24 to 27, 1965.

16. T. Z. Kattamis and M. C. Flemings: Trans. TMS-AIME, 1965, vol. 233, pp. 992-99.

17. F. C. Quigley and P. J. Ahearn: Trans. Am. Foundrymen's Soc., 1964, vol. 72, pp. 813-17.

18. ibid (15)

19. C. F. Jatczak, D. J. Giradi, and E. S. Rowland: Trans. Am. Soc. Metals, 1956, vol. 48, p. 279.

20. E. Okress, D. Wroughton, G. Comenety, P. Brace, J. Kelly, "Electro-magnetic Levitation of Solid and Molten Metals", J. Appl. Phys., 23, 545-552 (1952).

21. S. Y. Shiriashi and R. G. Ward, "The Density of Nickel in the Super-heated and Supercooled Liquid States", Can. Met. Quarterly, 3, 117-122 (1964).

22. M. C. Flemings, R. V. Barone, and H. D. Brody, "Investigation of Solidification of High Strength Steel Castings", AMMRC Report, Oct., 1967.

23. S. Bergh and O. Lindberg, Jernkont. Ann., v. 146, 1962, pp. 862-868.

24. J. W. Cahn and J. E. Hilliard, "An Evaluation of Procedures in Quantitative Metallography for Volume Fraction Analysis", Trans. AIME, v. 221, April, 1961.

25. T. Z. Kattamis, J. C. Coughlin, and M. C. Flemings, "Influence of Coarsening on Dendrite Arm Spacing of Aluminum-Copper Alloys", Trans. Met. Soc. AIME, v. 239, 1967, pp. 1504-1511.

26. G. Forward, "Nucleation of Oxide Inclusions During the Solidification cf Iron", Sc.D. Thesis, M.I.T., 1966.

27. J. Yarwood, "Inclusion Formation in the System Fe-FeO-FeS", Ph.D. Thesis, M.I.T., 1968.
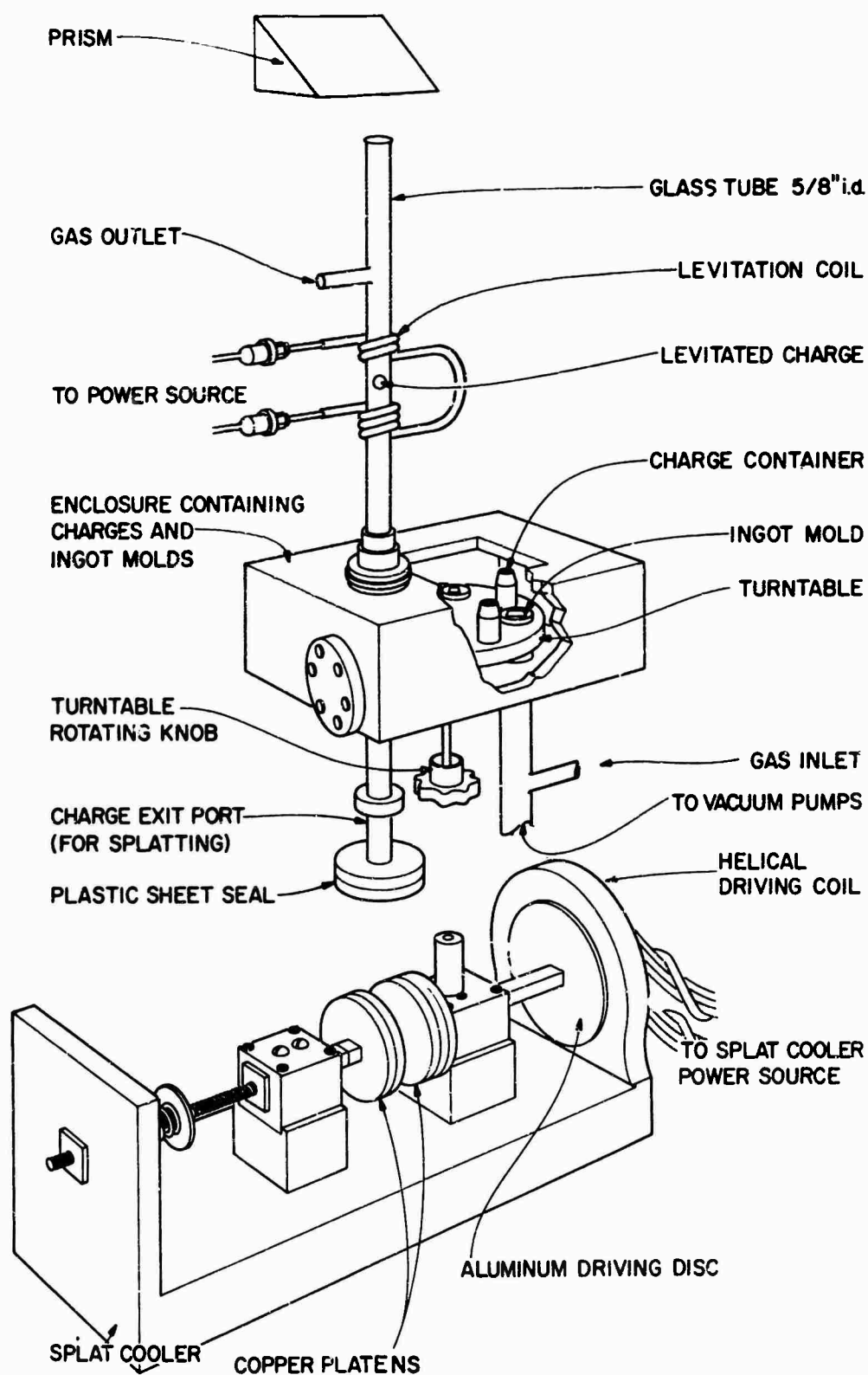
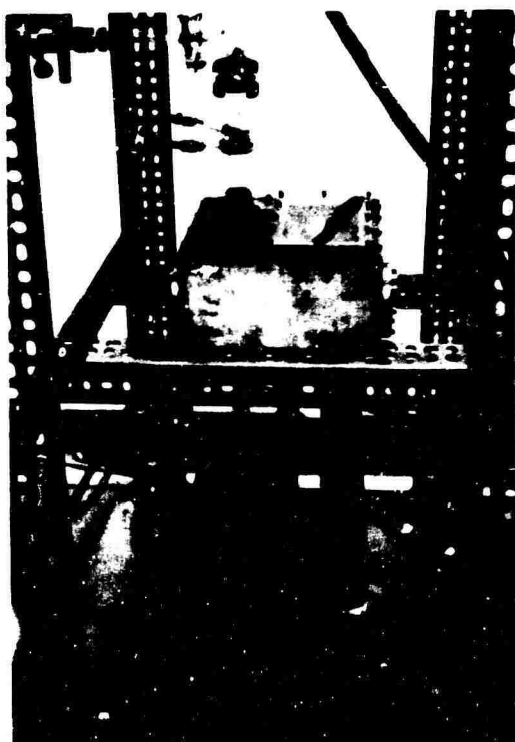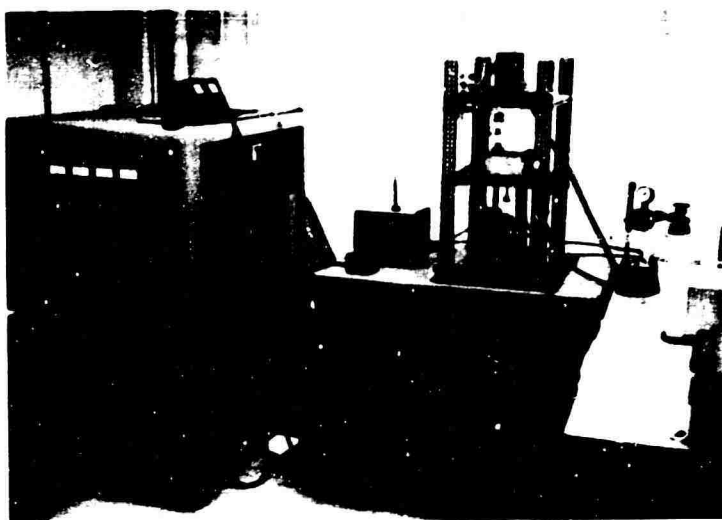Figure 1-1. Sketch of levitation melting and casting apparatus.

Figure 1-2. Photograph of levitation melting and casting apparatus.

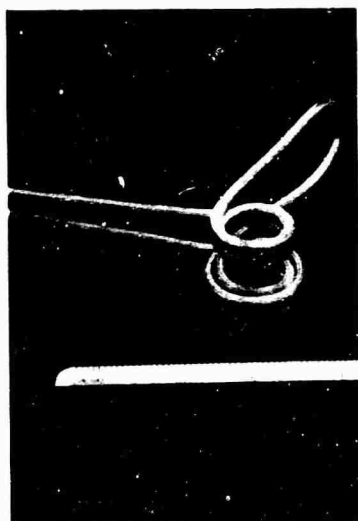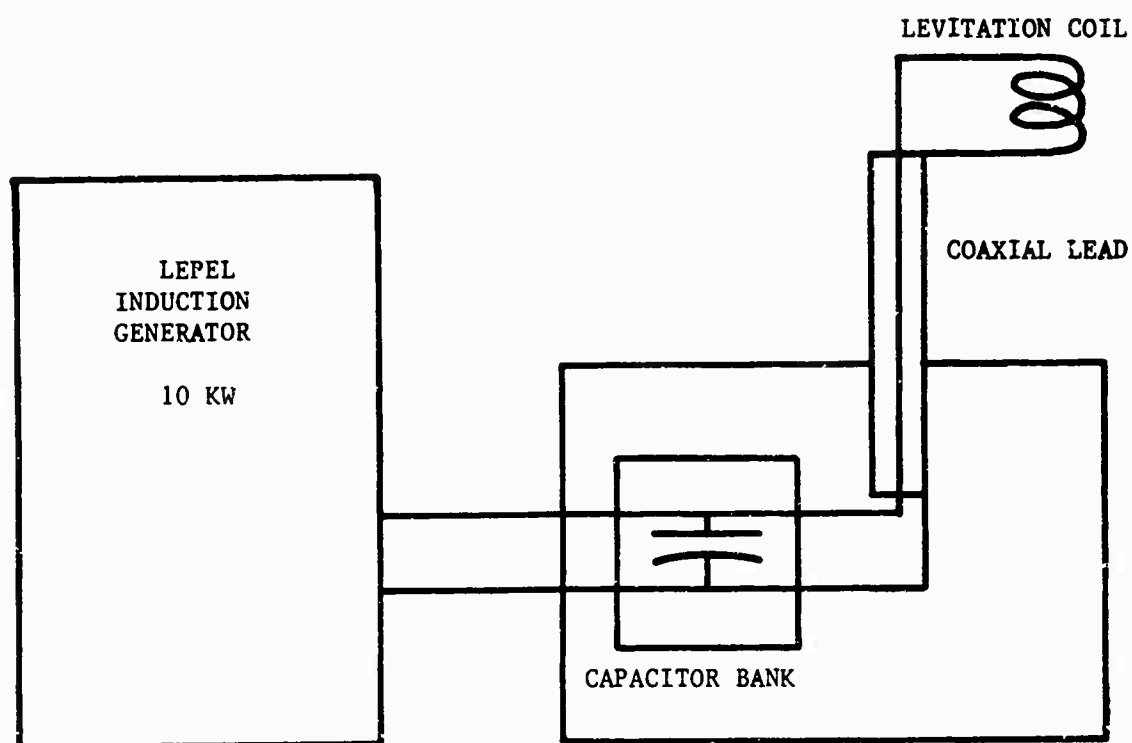Figure 1-3. Photograph of levitation coil.

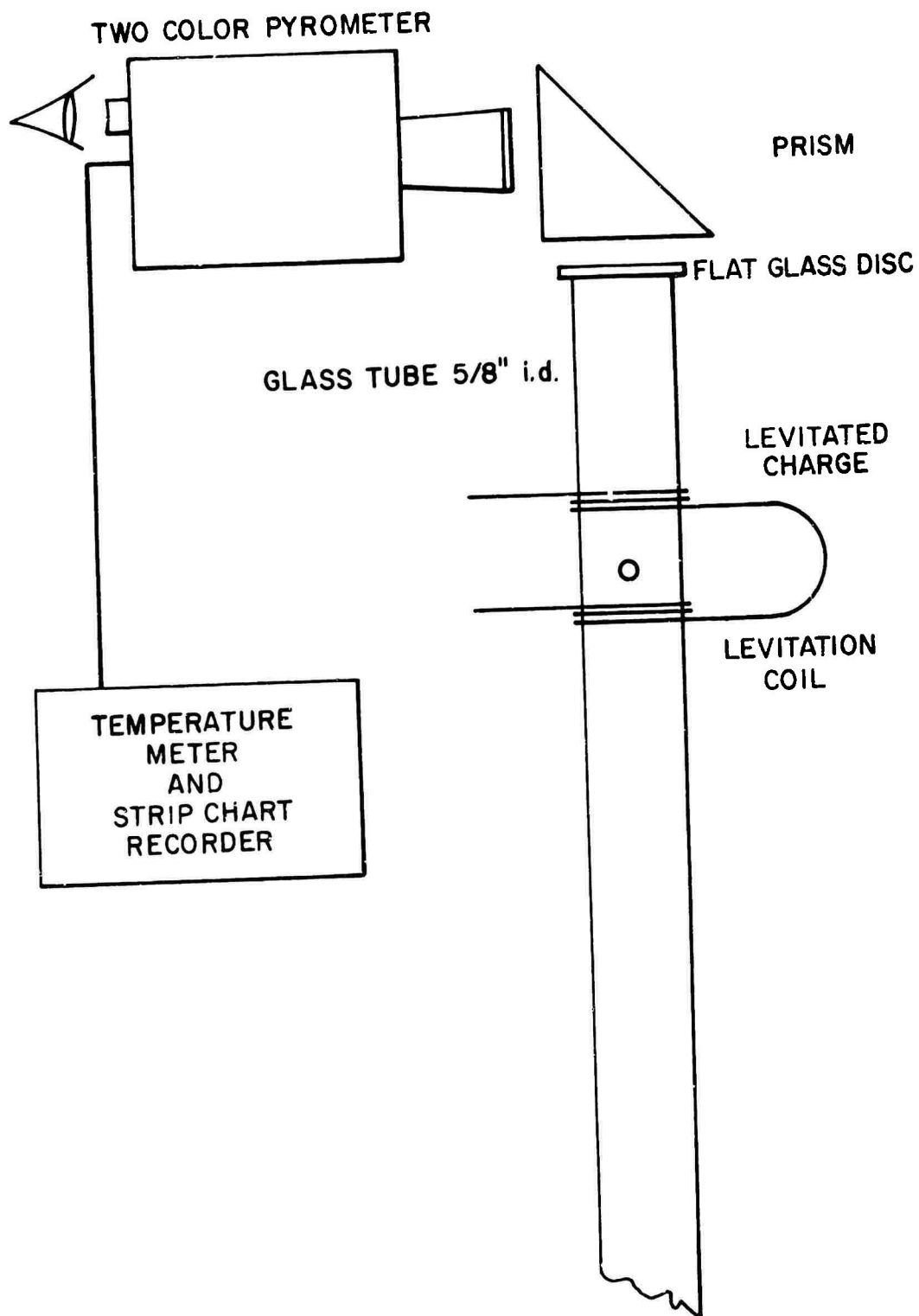Figure 1-4. Schematic diagram of levitation melter circuit.

TWO COLOR PYROMETER

PRISM

FLAT GLASS DISC

GLASS TUBE 5/8" i.d.

LEVITATED
CHARGE

LEVITATION
COIL

TEMPERATURE
METER
AND
STRIP CHART
RECORDER

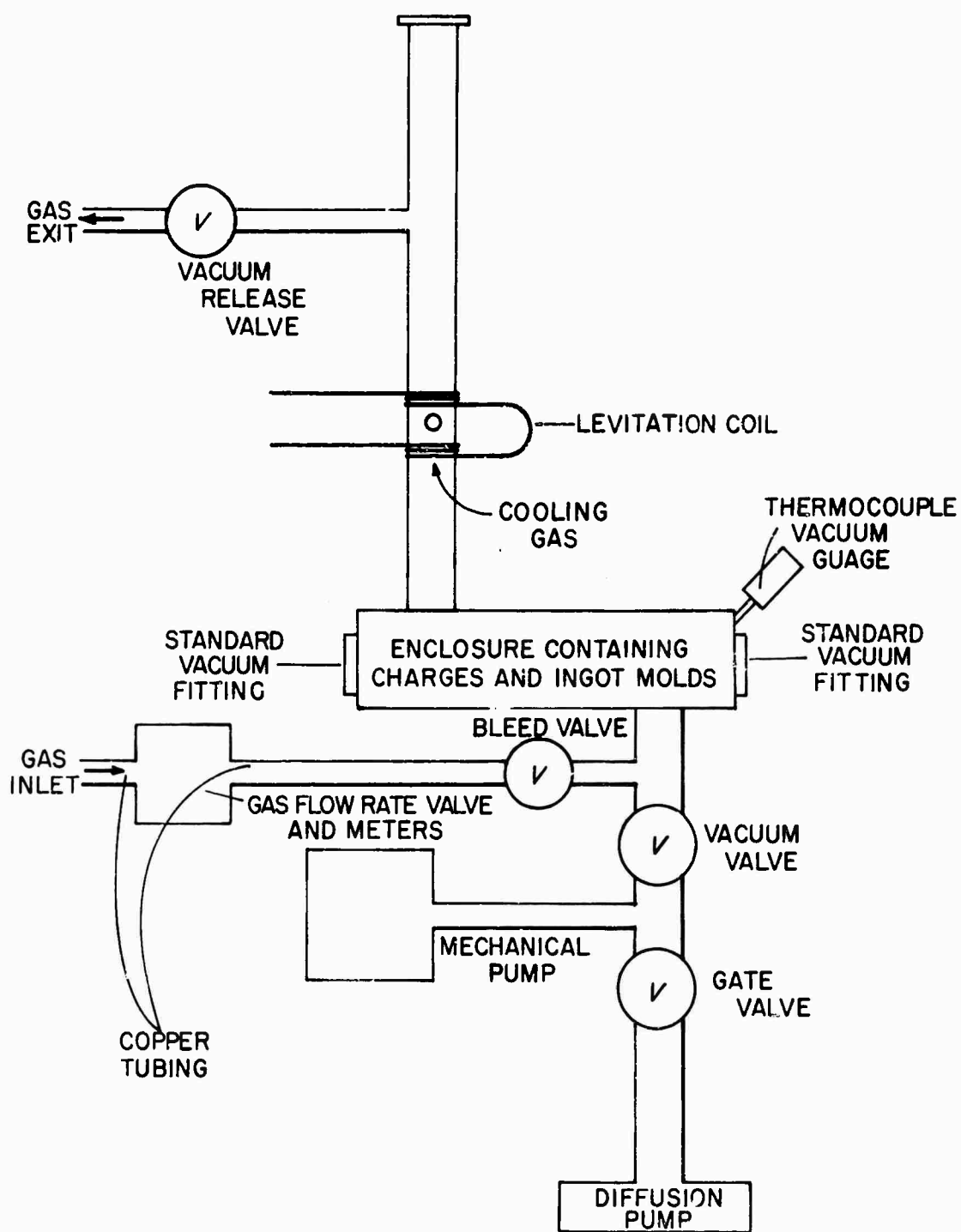Figure 1-5. Schematic diagram of temperature measuring system.

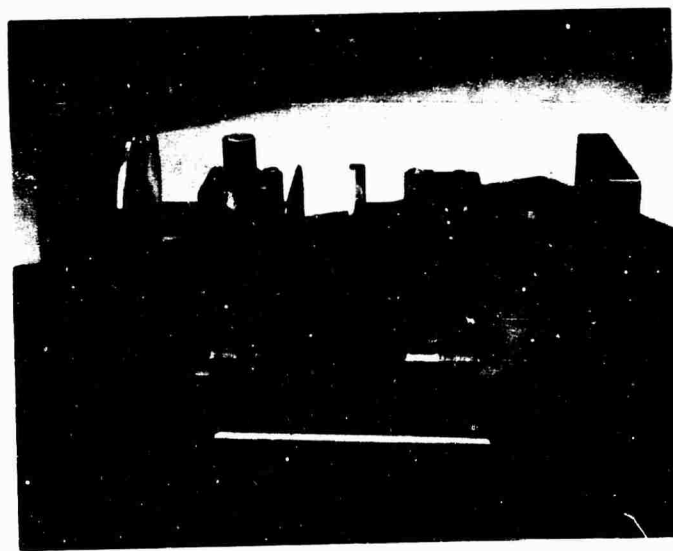Figure 1-6. Schematic diagram of gas flow system.
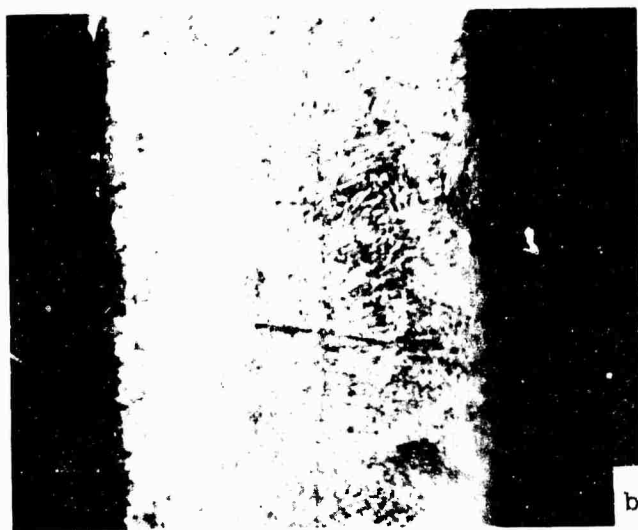
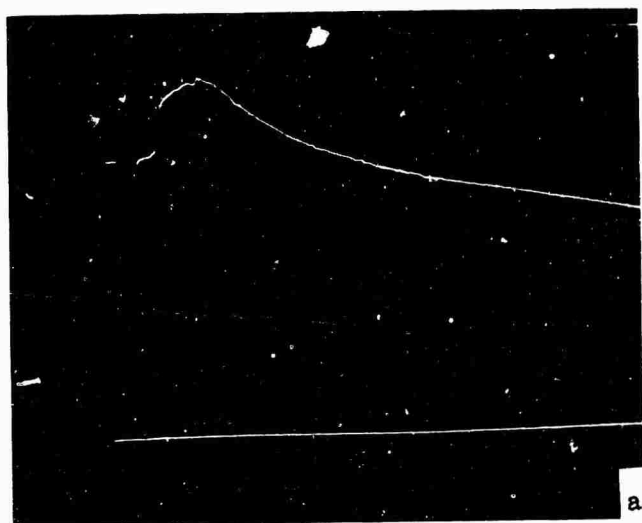Figure 1-7. Photograph of "hammer and anvil".

Figure 1-8. (a) Optical photocell eye cooling curve, eye in the moving
platen, Iron-25 per cent Nickel specimens, clapper
velocity 450 cm/second, vertical scale 0.1 volt/division,
1 millisecond/division time scale, 140-160°C superheat.
(b) Resulting microstructure of Fe-25%Ni alloy splat.
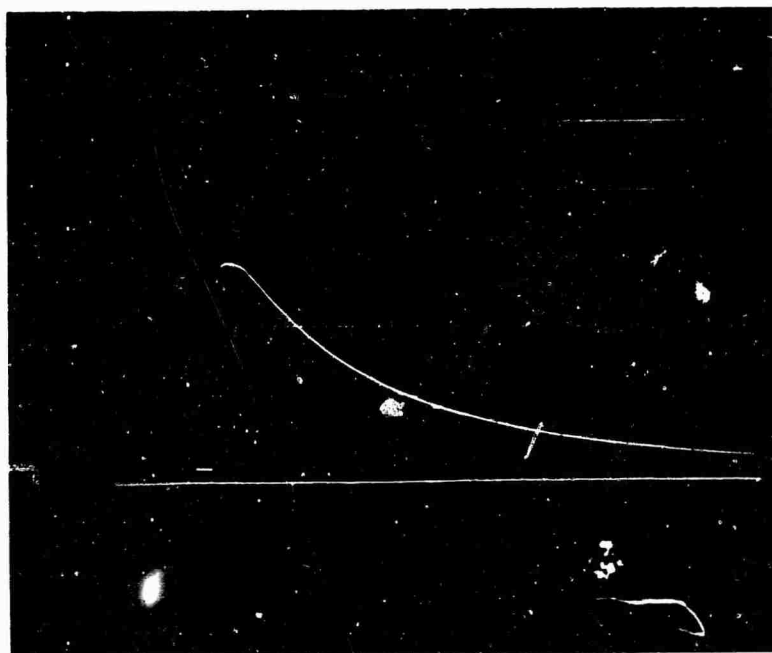Magnification 1000X.
(Marble's etch).

Figure 1-9. Thermocouple cooling curve for Fe-25%Ni alloy 0.08 inches thick chill casting. Dropped from levitation coil at 1600°C, 5 millivolt/division vertical scale, 0.5 second/division horizontal scale.
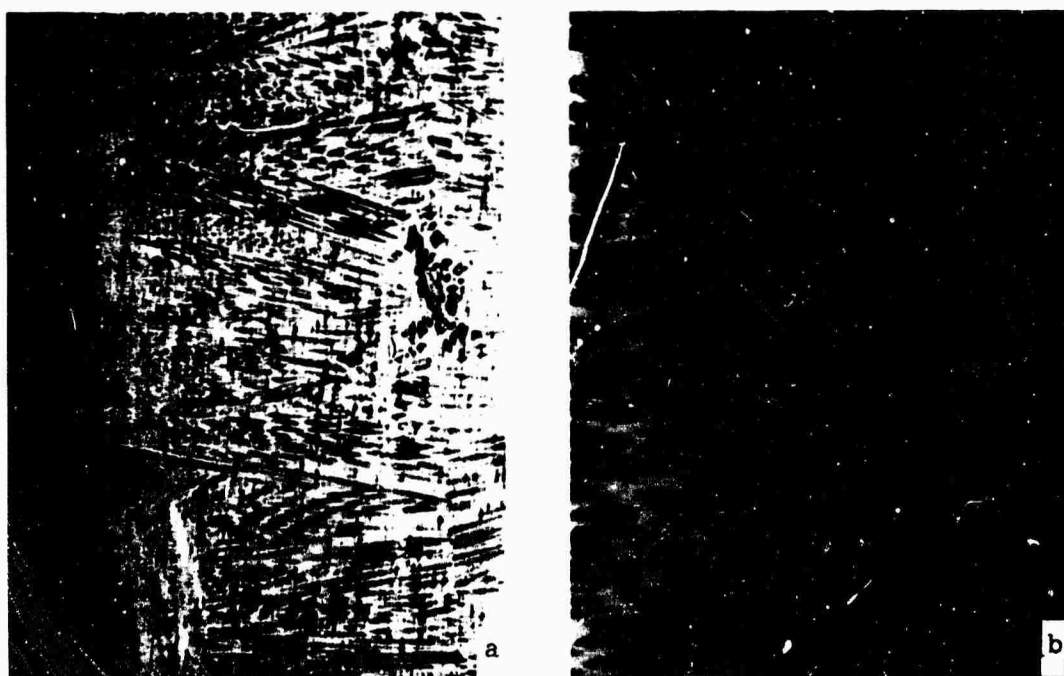
Figure 1-10. Fe-25%Ni chill plate casting 0.08 inches thick, dropped at 1600°C from the levitation coil.
Magnification (a) 55X, (b) 500X.
(Marble's etch).

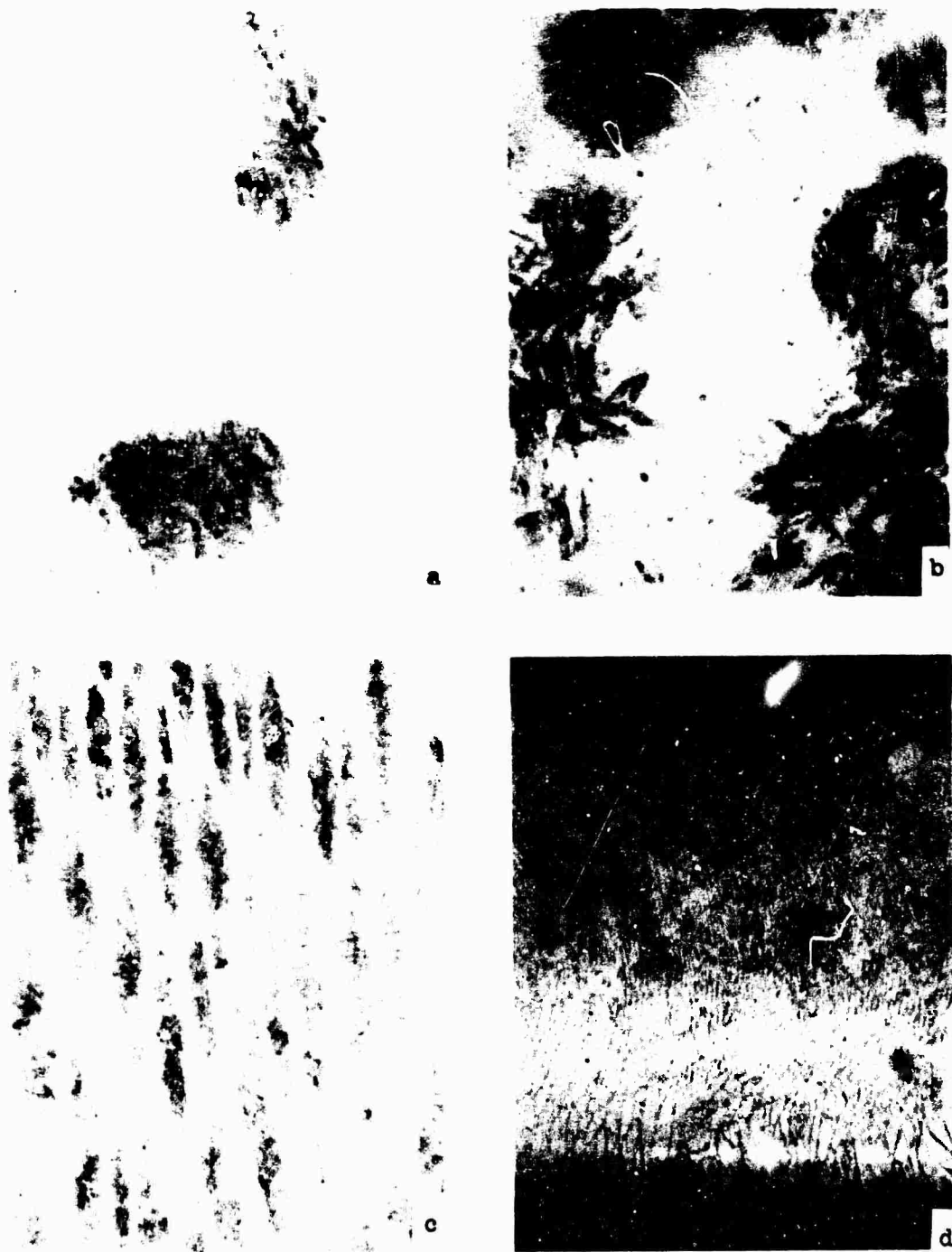Figure 1-11. The variation of microstructure with cooling rate for Fe-25%Ni alloy. (a) electron beam "zone alloyed", (b) liquid quenched, (c) chill cast, (d) splat cooled. (Magnification 500X, Marble's etch).

(a)

(b)

(c)

(d)

Figure 1-12. Variation of microstructure with cooling rate for 440C
alloy. (a) gas quench, (b) liquid quench, (c) chill cast,
(d) splat cooled.
(Magnification 500X, Murakami's etch).

(a)

(b)

(c)

(d)

Figure 1-13. Variation of microstructure with cooling rate for 4330
alloy. (a) gas quench, (b) liquid quench, (c) chill cast,
(d) splat cooled.
(Magnification 500X, Rosenhain's etch).

SECONDARY DENDRITE ARM SPACING (MICRONS)

1000

100

10

1

0.1

FURNACE COOLED
× UNIDIRECTIONALLY SOLIDIFIED
○ SPLAT COOLED
△ THIS WORK
+

$d = 60 \, \dot{T}^{-0.32}$

OIL
QUENCHED

CHILL
CAST

10^{-3} 10^{-1} 10^{+1} 10^{3} 10^{5} 10^{7}
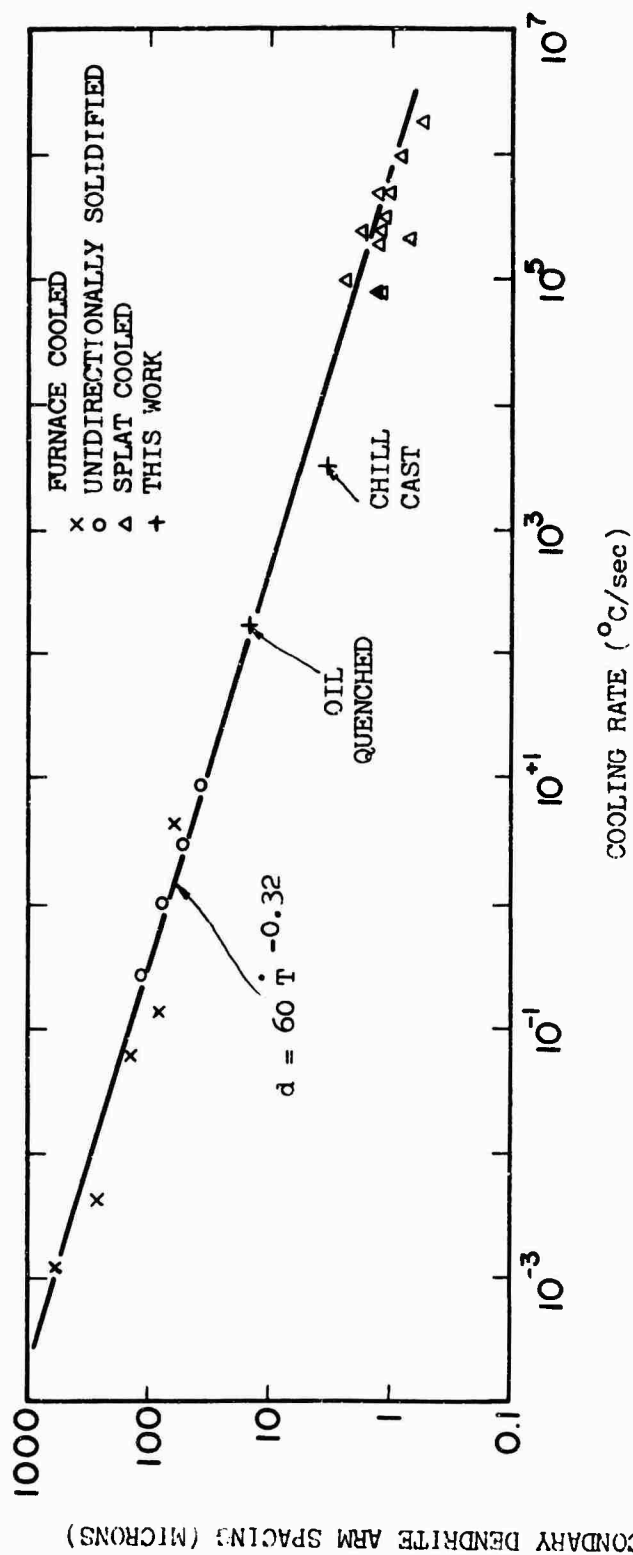
COOLING RATE (°C/sec)

Figure 1-14. Dendrite arm spacing versus cooling rate,
Fe-25 per cent Ni alloy.
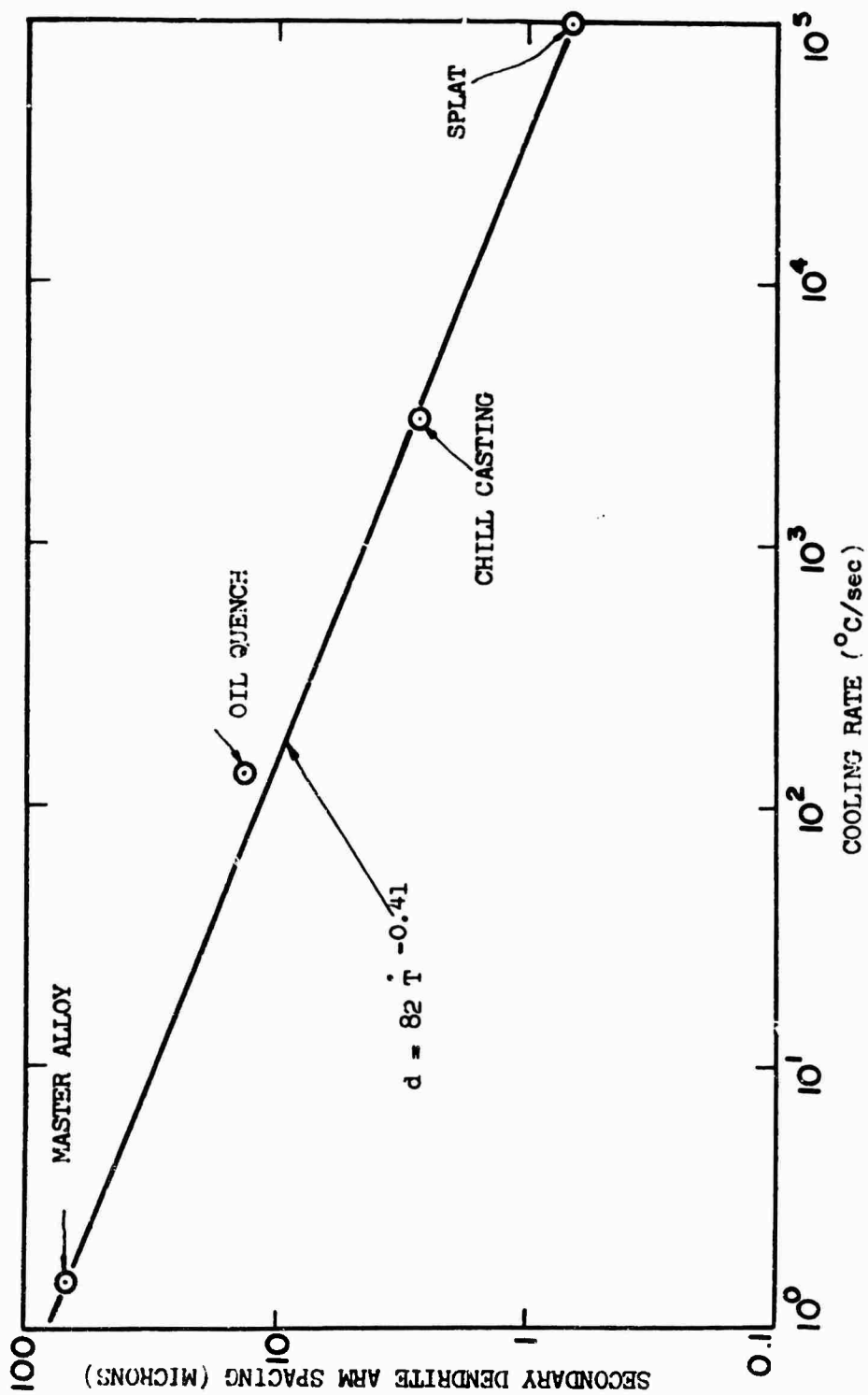
Figure 1-15.   Dendrite arm spacing versus cooling rate, 440C alloy.
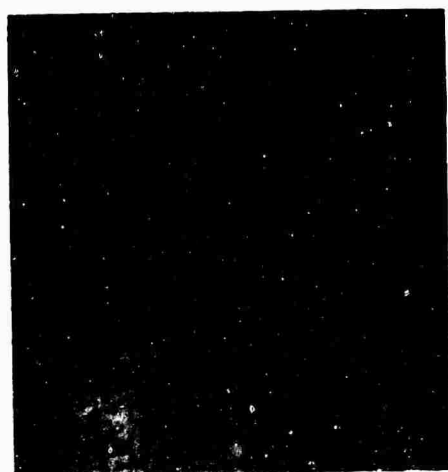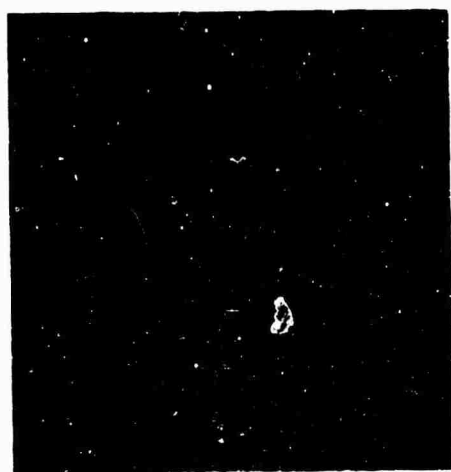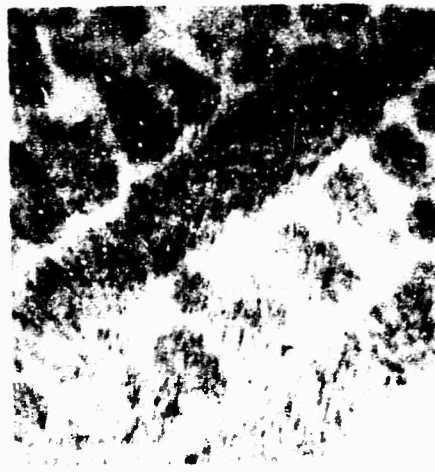
Figure 1-16. Variation of microstructure with cooling rate for
Fe-4.3%C alloy. (a) master alloy, (b) liquid quenched,
(c) chill casting, (d) splat.
Magnification 500X.
(Nital etch).
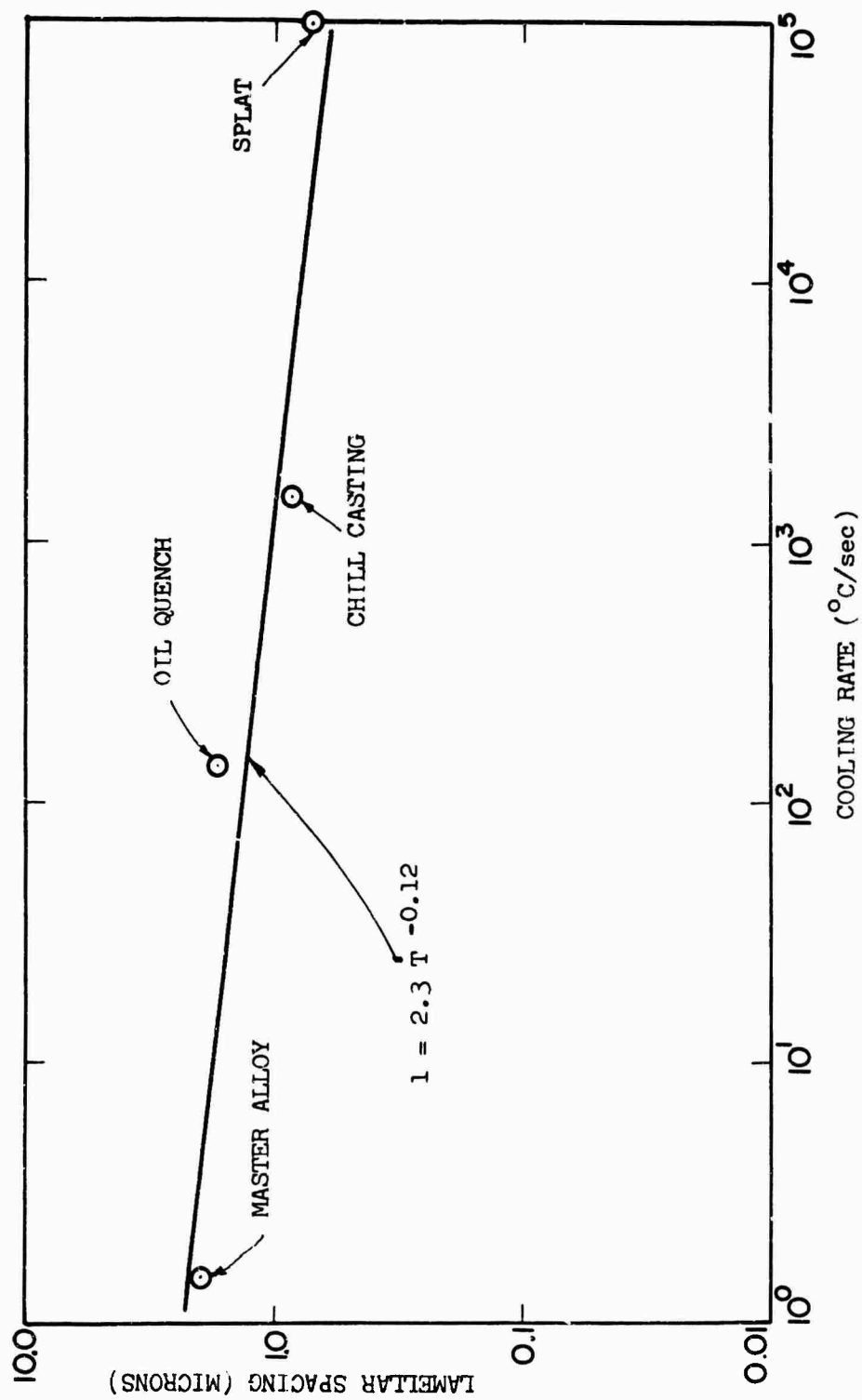
Figure 1-17. Lamellar spacing versus cooling rate, Fe-4.3%C alloy.
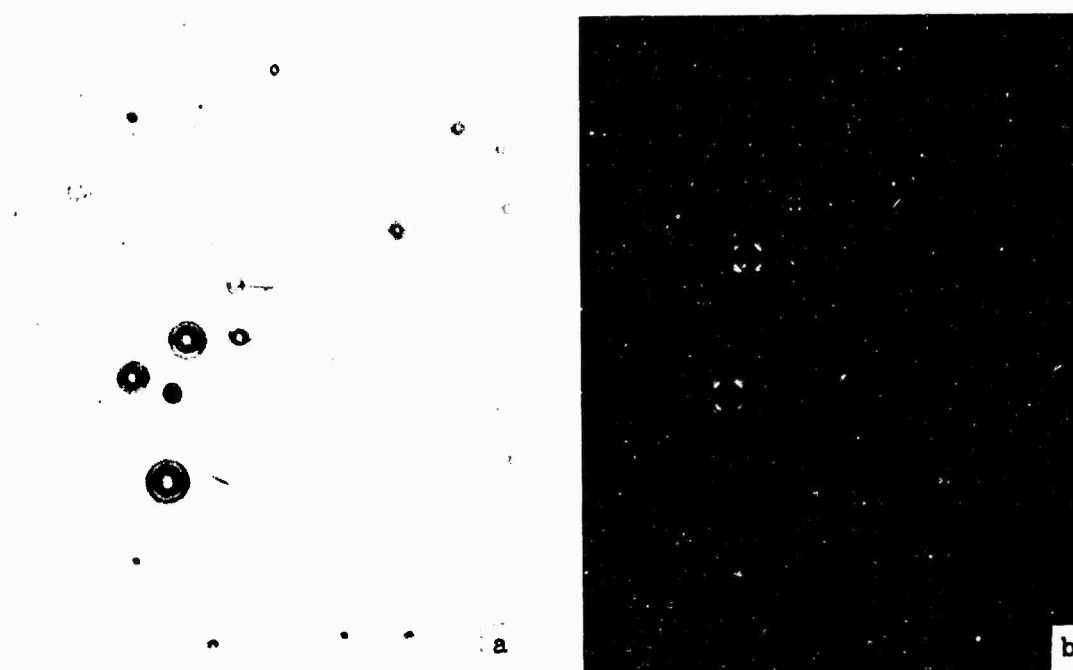
Figure 1-18. Microstructure of Fe-0.05%Si master alloy. (a) white light, (b) polarized light. (Magnification 880X).
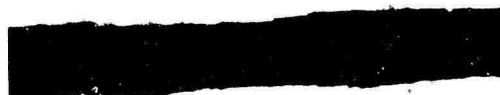
Figure 1-19. Microstructure of Fe-0.07%0 alloy. (a) master alloy,
(b) liquid quenched, (c) chill casting, (d) splat.
(Magnification 1000X).

Figure 1-20. Variation of microstructure with cooling rate for
Fe-0.05%Si alloy. Magnification (a) master alloy, 530X,
light microscope, (b) liquid quenched, 1000X, mechanically
polished, light microscope, (c) chill casting, 11,200X,
electropolished, parlodion replica, (d) splat, 100,000X,
electropolished, parlodion replica.
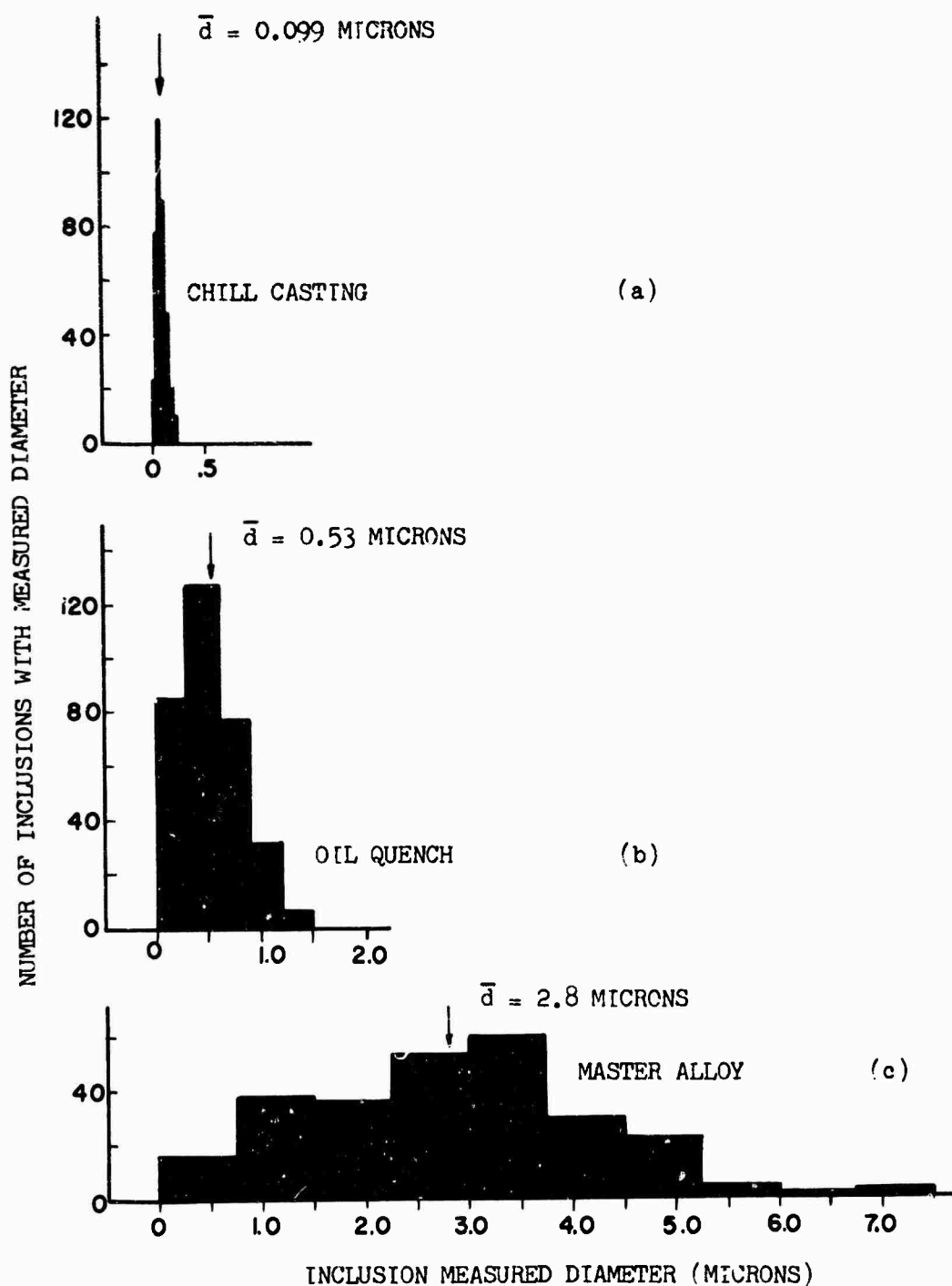
Figure 1-21. Size distributions of SiO_2 inclusions in the as cast
Fe-0.05%Si alloy for the various quenching techniques.
a. chill casting, b. liquid quench, c. master alloy.
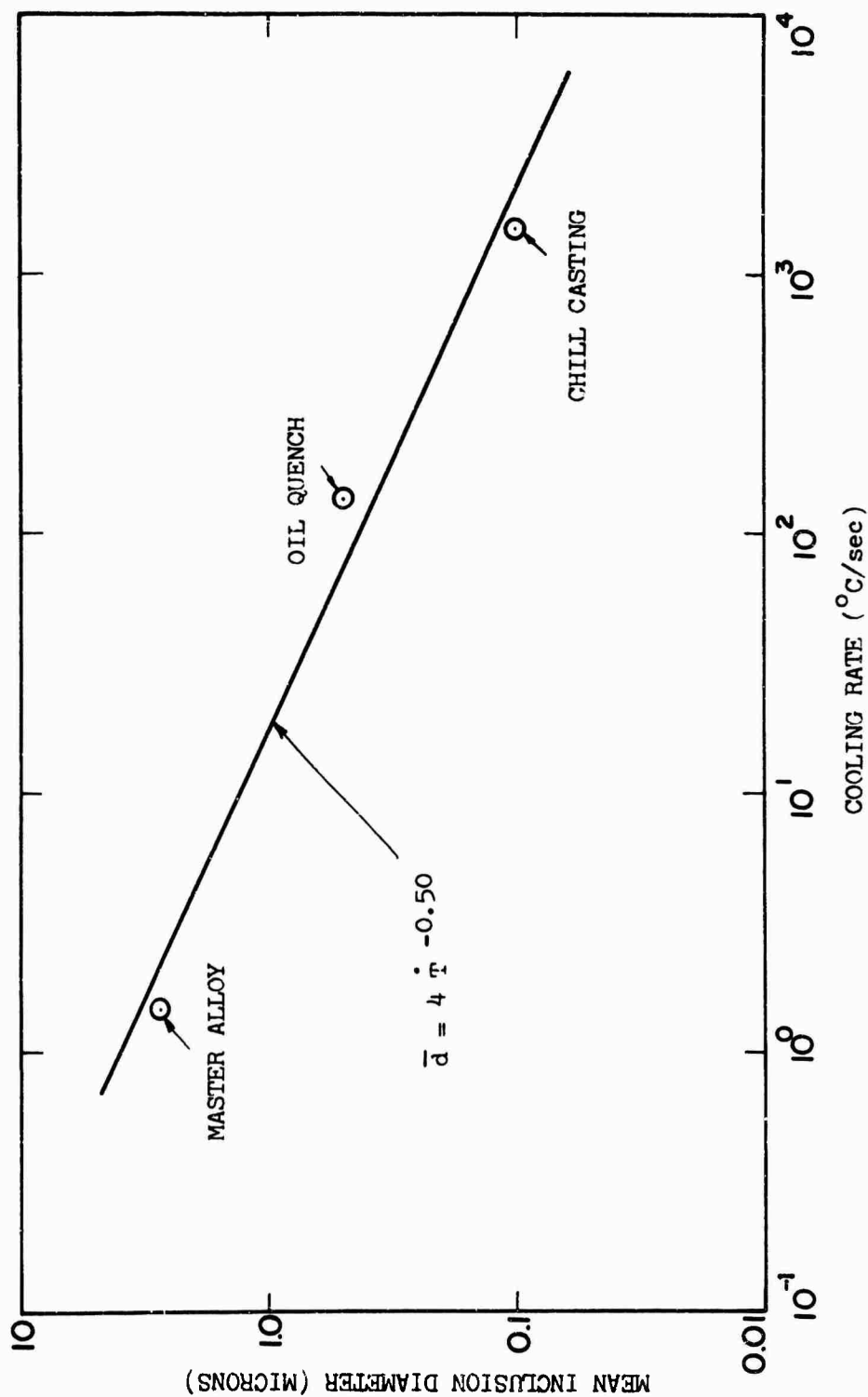
Figure 1-22. Mean measured SiO_2 inclusion diameter versus cooling rate for Fe-0.05%Si alloy.
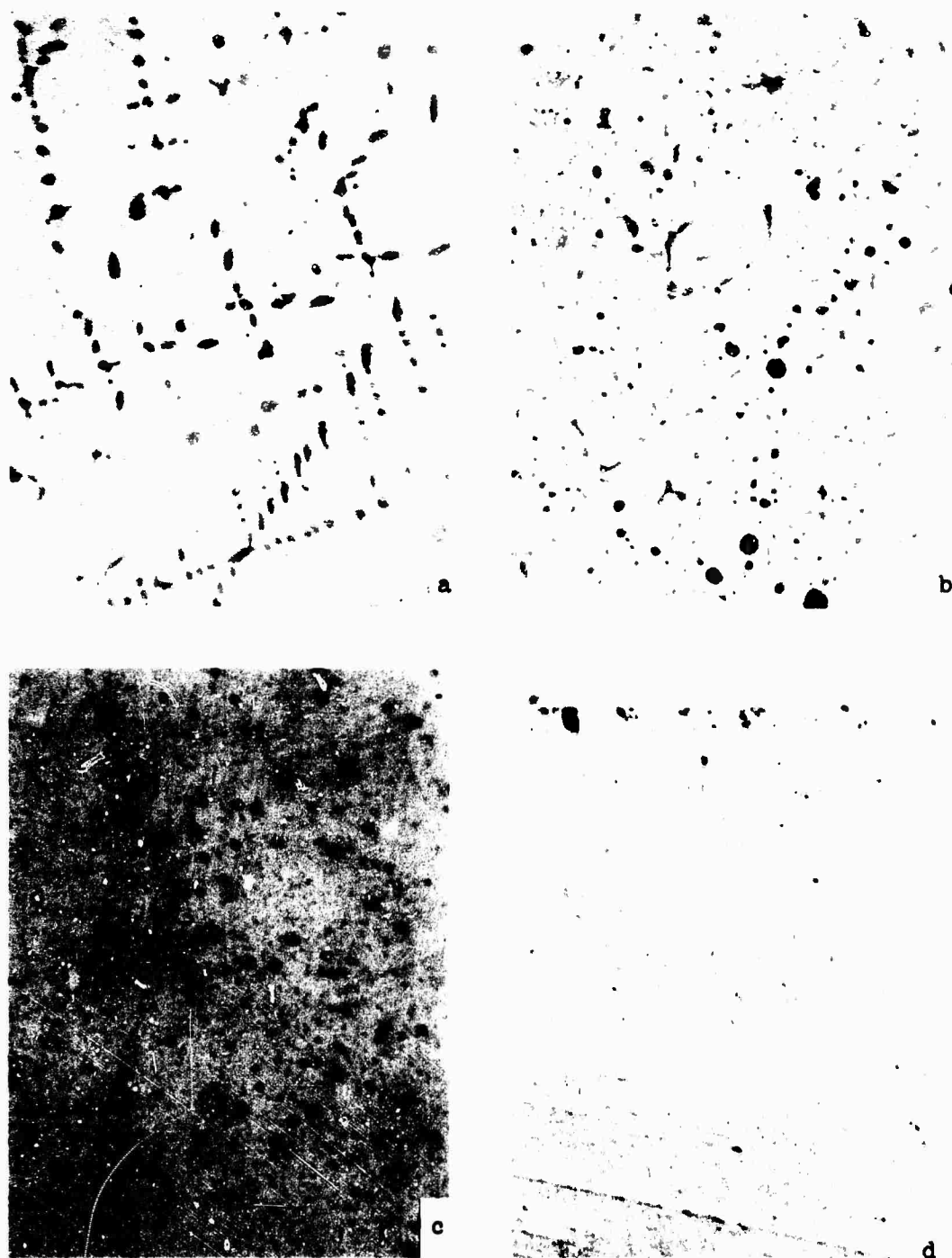
Figure 1-23. Variation of microstructure with cooling rate for
Fe-Mn-S alloy. (a) master alloy (b) liquid quench,
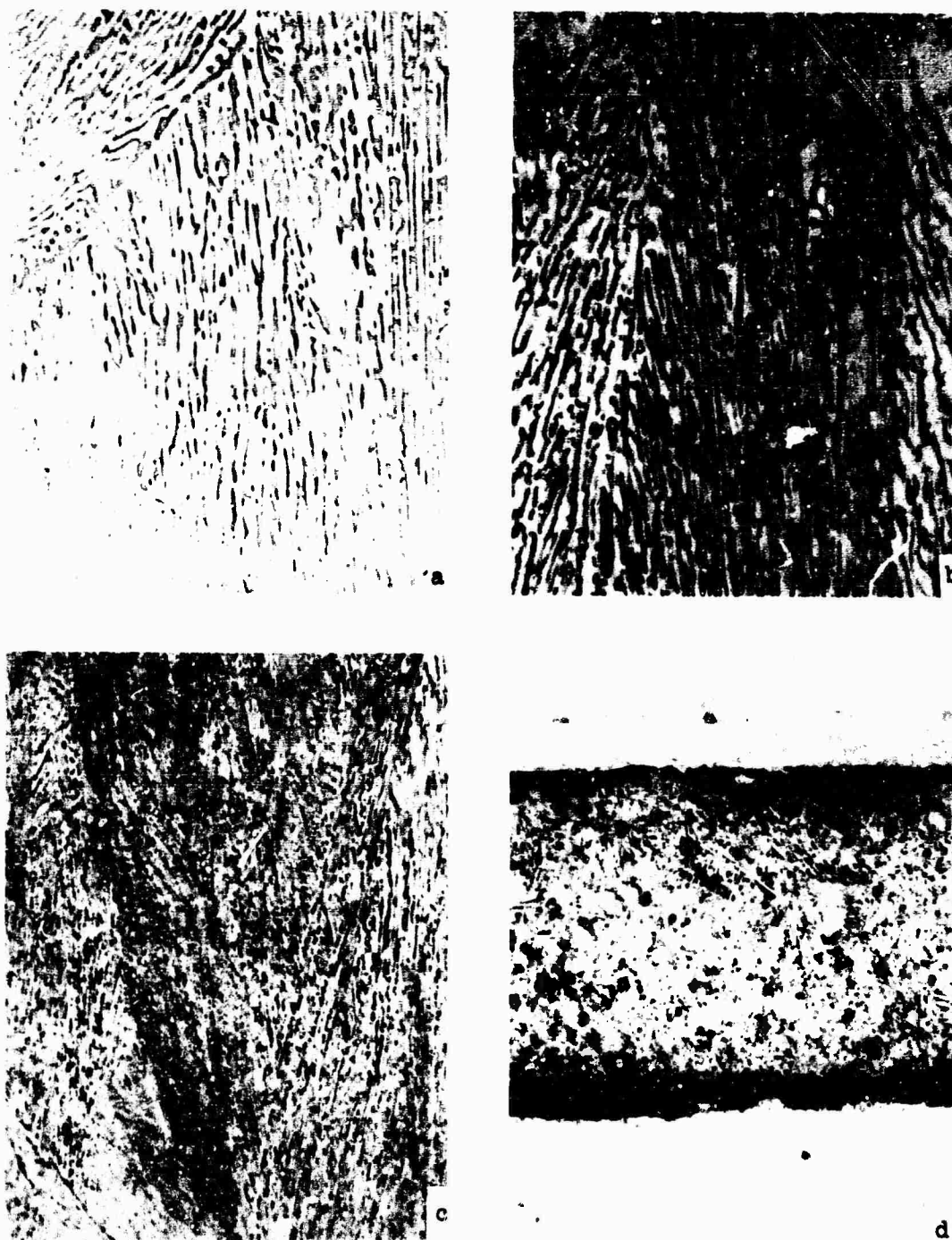(c) chill cast, (d) splat.
(Magnification 500X).

Figure 1-24. Variation of inclusion morphology with cooling rate for
4330 low alloy steel. (a) master alloy, (b) liquid quench,
(d) chill cast, (d) splat.
(Magnification 500X, unetched).
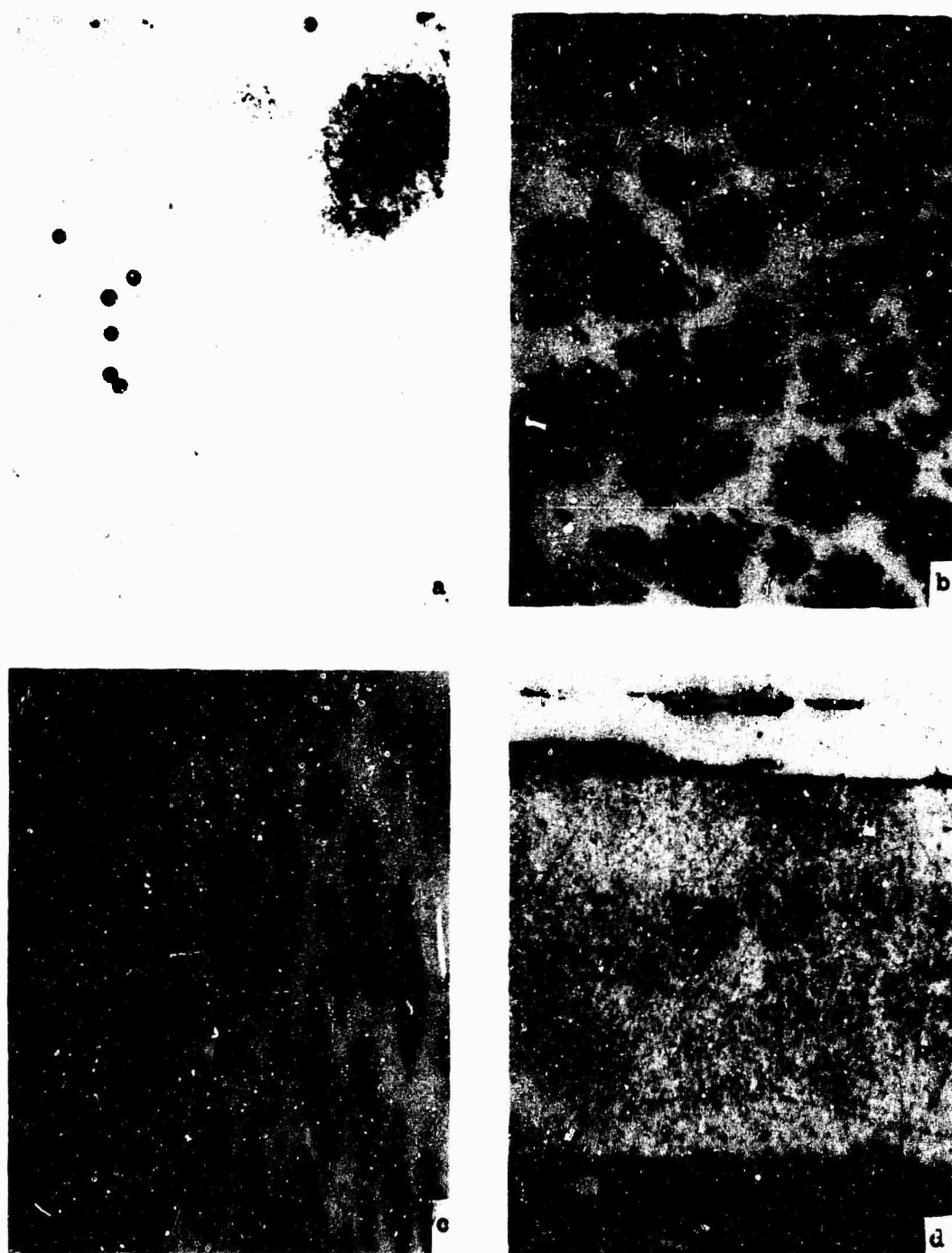
Figure 1-25. Variation of microstructure with cooling rate for
Fe-25%Ni-0.05%Si alloy. (a) master alloy, (b) liquid
quenched, (c) chill cast, (d) splat cooled.
(Magnification 500X, Marble's etch).

Chapter II

ISOTHERMAL SOLID STATE COARSENING OF SILICA INCLUSIONS

Introduction and Literature Survey

After precipitation of a second phase in a solution is complete, precipitate size continues to increase due to a phenomenon known as Ostwald ripening, i.e., reduction of surface free energy by growth of large particles at the expense of smaller ones. Wagner[1] has developed a theoretical expression describing Ostwald ripening; a cubic relationship between particle size and ripening time resulted. Greenwood[2] has studied the ripening of solid spherical precipitates in a saturated liquid solution; he found a cubic relationship between spherical precipitate radius and ripening time. Ardell and Nicholson[3] in studying the aging kinetics of gamma prime precipitates in Ni-6.7%Al alloy also found a cubic relationship between particle size and coarsening (ripening) time. Lifshitz and Slyozov[4] have applied coarsening kinetics to second phase grain growth in a solid solution. Oriani[5] studied this type of coarsening for spherical carbide precipitates in iron; again a cubic coarsening law was observed.

High temperature (1371°C) homogenization treatments were carried out on high strength 4330 alloy steel for 24, 64, and 186 hours by Quigley and Ahearn[6] to determine the effect of such treatments on mechanical properties. An increase of ductility with homogenization time was observed. Exactly what structural features were altered by this treatment (e.g., microsegregation, inclusions, grain size) was not determined, and this work was, therefore, undertaken to determine if inclusion ripening (FeO or SiO_2 inclusions) would be significant at the times and temperatures involved.

The high temperature solid state coarsening kinetics for SiO_2 inclusions were studied for the Fe-0.05%Si master alloy, chill casting, and splat at $1400^{\circ}C$. This knowledge will compliment that already obtained in Section I concerning the solidification behavior of these SiO_2 inclusions in the Fe-0.05%Si alloy.

Since the SiO_2 inclusions are spherical even at diameters less than 0.1 μ, a simple case of Ostwald ripening of spheres in a solid is presented as soon as the equilibrium volume fraction of SiO_2 is reached in the Fe-0.05%Si alloy at $1400^{\circ}C$.

Procedure

Isothermal heat treatment of specimens of the Fe-0.05%Si alloy at $1400^{\circ}C \pm 5^{\circ}C$ was carried out in a globar type tube furnace. The longitudinal temperature gradient in the furnace was first determined, and the specimens were placed such that the maximum positional temperature variation was less than $\pm 4^{\circ}C$. Specimens were vacuum encapsulated in fused quartz tubes after evacuation of the tubes to less than 5 torr and backfilling with He three times. The quartz tubes were placed in a firebrick rack which not only enabled removal of the specimens from the furnace without damage, but also acted as a thermal mass and decreased both the temporal and positional thermal fluctuations. $1400^{\circ}C$ is slightly below the softening point, but well below the fusing point of fused quartz, so that, although the evacuated quartz tubes collapsed around the specimens, the vacuum was maintained. Any leaks in the capsule would result in total destruction of the specimens at the times and temperatures used. Such a result was experienced a few times. To prevent a diffusion reaction between the SiO_2 tube and the Fe-0.05%Si specimens, each specimen was wrapped in Fe-0.05%Si alloy splat. Also, although some diffusion bor... ng of the splat wrappings and the specimens took place, no bonding between the quartz and the splat wrappings was ever observed.

Results and Discussion

Specimens of the Fe-0.05%Si master alloy, chill casting, and splat were held at 1400°C for 12, 24, and 48 hours. The resulting size distributions(including the "as cast" material for the master and chill casting) of SiO_2 inclusions as measured on a polished section are shown in Figures 1, 2, and 3. These planar distributions may be converted, if desired, to the true three dimensional distribution as shown in Appendix C and Figure C-1. For this work it is assumed that the true mean diameter of spherical inclusions is 1.2X, as discussed in Section I, greater than the measured planar mean diameter. The volume fraction of inclusions was again determined by a systematic point count.

Plots of mean inclusion diameter, number of inclusions per unit area, and volume fraction of inclusions versus time at 1400°C are given in Figure 4 for the master alloy, chill casting, and splat of the Fe-0.05%Si alloy. The results of the measurements of the size distributions, volume fractions, and number per unit area of inclusions (Figures 1, 2, and 3, and Table 1) indicate that the SiO_2 inclusions formed in the Fe-0.05%Si alloy coarsen in the solid matrix at 1400°C. The decrease in the number per unit area (proportional to number per unit volume) and the increase in mean SiO_2 inclusion diameter, while maintaining the volume fraction constant, indicate that the larger inclusions are growing at the expense of the smaller ones, i.e., Ostwald ripening is taking place. The increase of measured volume fraction of SiO_2 inclusions is the structure during the first 12 hours of heat treatment indicates either that silicon and oxygen are somewhat supersaturated during solidification and/or subsequent cooling, or that a small volume fraction of SiO_2 particles present lie below the optical

limit of resolution in the as cast structure. Also, the increase in volume fraction of SiO_2 inclusions after 12 hours may be due in part to an effect of the increased mean inclusion diameter (radius of curvature) on the equilibrium solubility of SiO_2.

The slightly higher coarsening rate of the master alloy as compared to that of the chill casting and splat is due to the larger standard deviation in the as cast size distribution of the inclusions in the master alloy, Figure 1a, as compared to that of the chill casting, Figure 2a. This deviation in particle size is the driving force for Ostwald ripening. A high standard deviation, therefore, gives a high rate of inclusion coarsening or Ostwald ripening.

The plots in Figure 4 indicate that appreciable ripening of SiO_2 inclusions does occur after 12, 24, and 48 hours in iron at $1400^{\circ}C$, approximately the temperature of Quigley and Ahearn's high temperature homogenization experiments ($1371^{\circ}C$). Since Quigley and Ahearn homogenized for up to 186 hours, SiO_2 and other types of inclusions in the 4330 steel would have sufficient time to coarsen appreciably.

REFERENCES

1. Wagner, Z. Elchem., v. 65, 1961, p. 581.

2. G. N. Greenwood, "The Growth of Dispersed Particles in Solutions", Acta. Met., Vol. 4, 1956, pp. 243-248.

3. A. J. Ardell and R. B. Nicholson, "On the Modulated Structure of Aged Ni-Al Alloys", Acta Met., v. 14, 1966, p. 1295.

4. I. M. Lifshitz and V. V. Slyozov, "Kinetics of Diffuse Decomposition of Supersaturated Solid Solution", J. Experimental Theoretical Physics (USSR), Vol. 35, 1958, pp. 479-492.

5. R. Oriani, Acta Met., v. 12, 1964, p. 1399.

6. F. C. Quigley and P. J. Ahearn, "Homogenization of High Strength Steel at 2500°F.", Transactions of the American Foundrymen's Society.

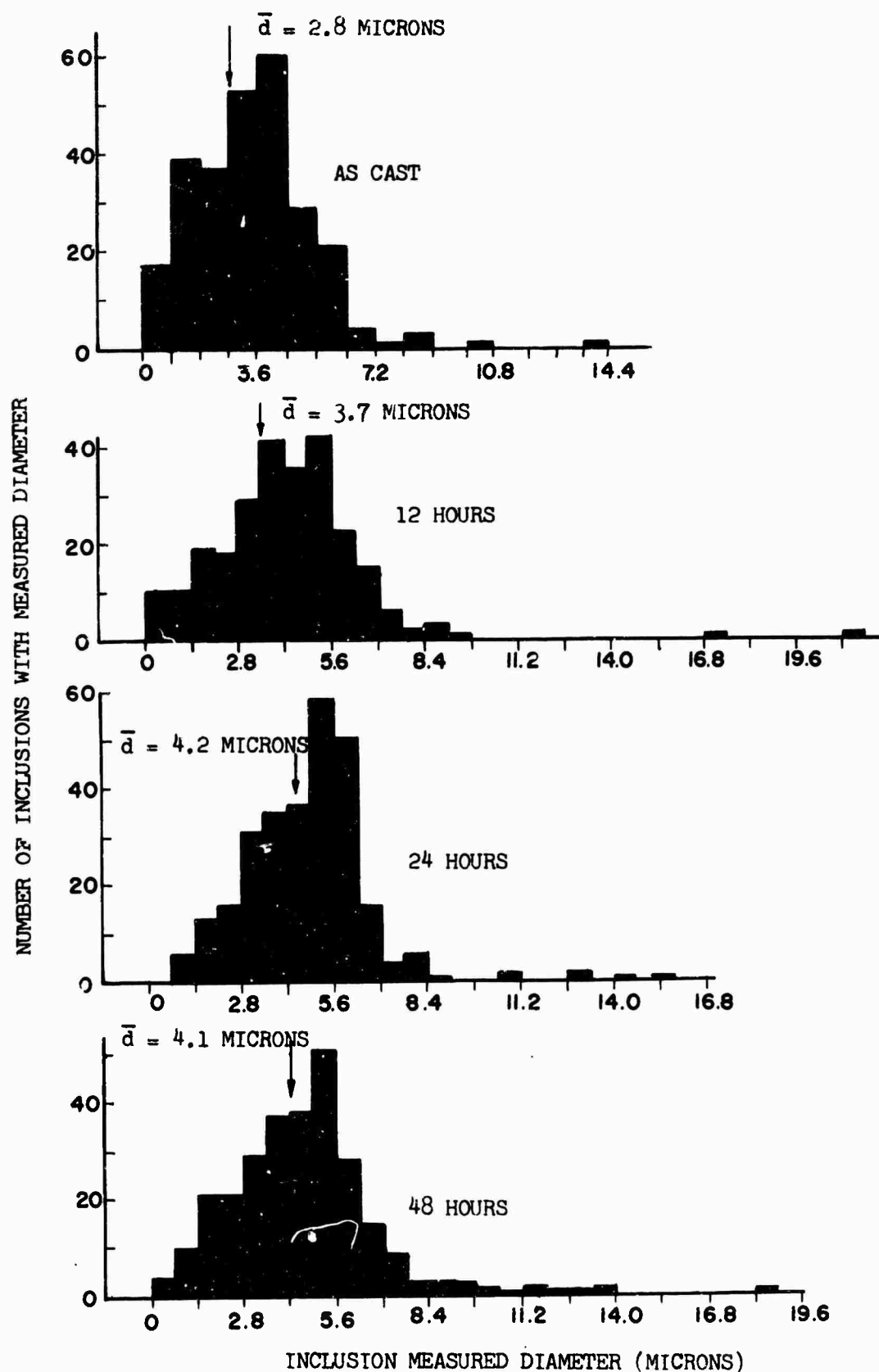Figure 2-1.   Size distributions of SiO_2 inclusions in the Fe-0.05%Si master alloy for various homogenization times at 1400°C.
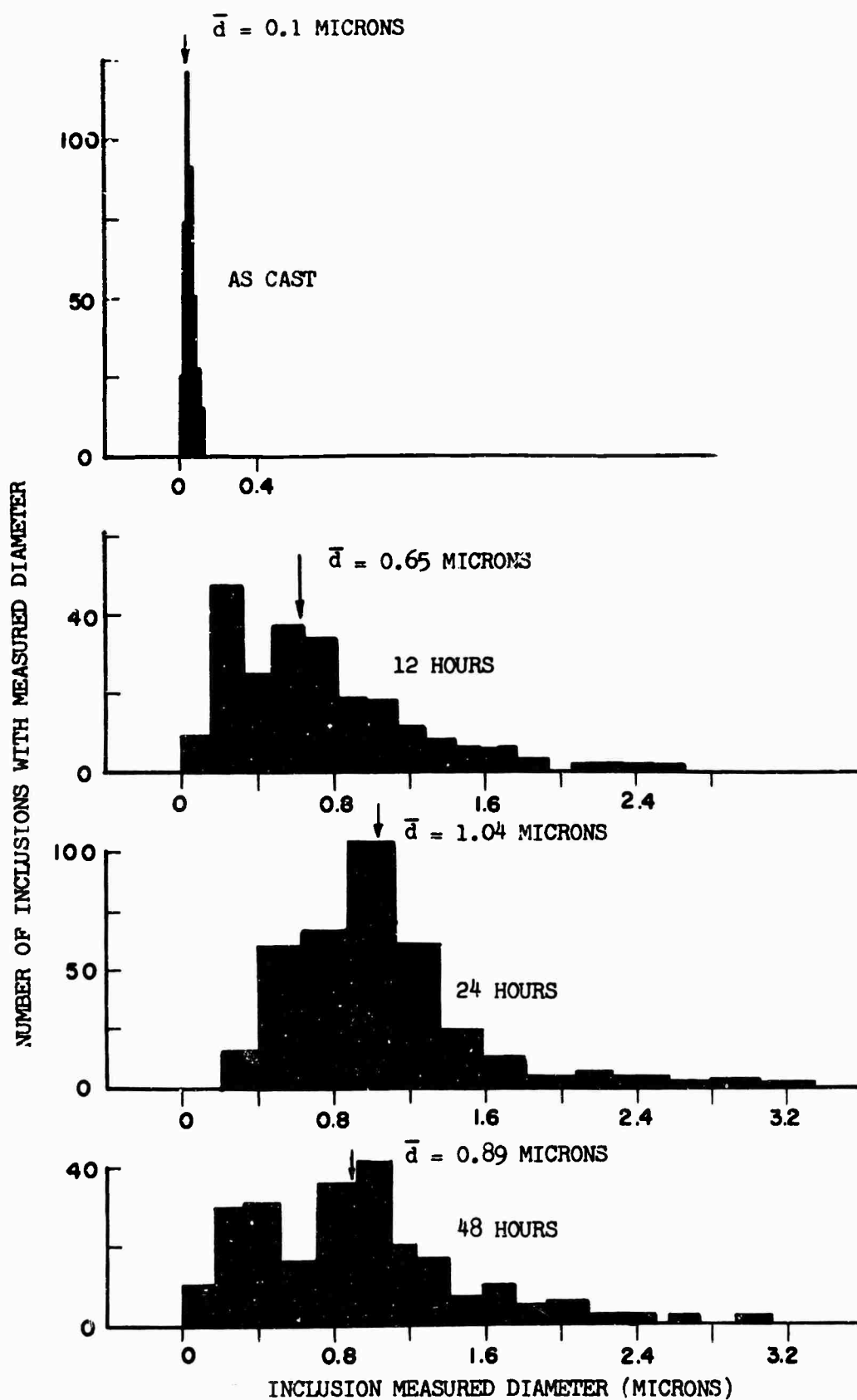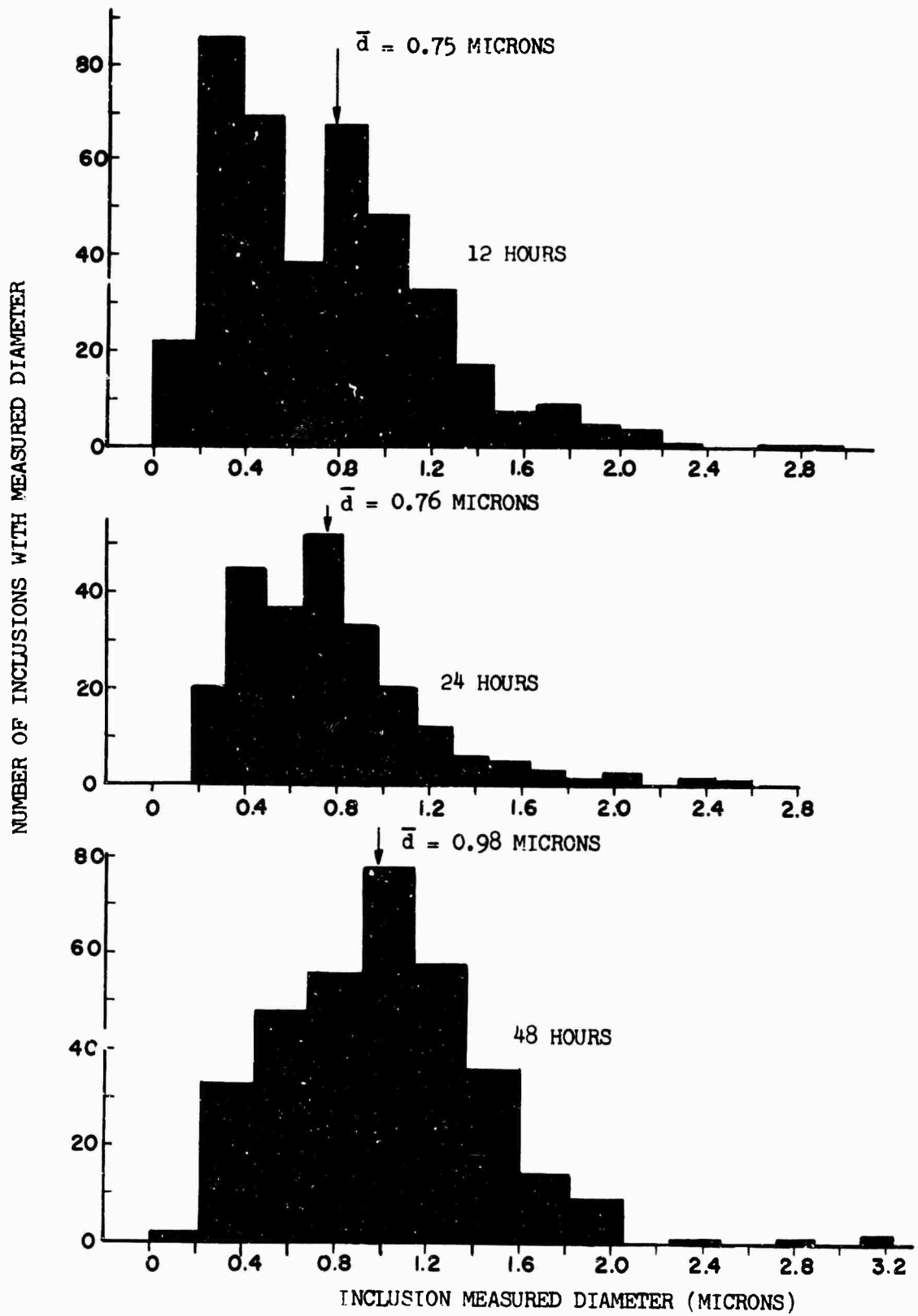
Figure 2-2. Size distributions of SiO_2 inclusions in the Fe-0.05%Si chill castings for various homogenization times at $1400^{\circ}C$.
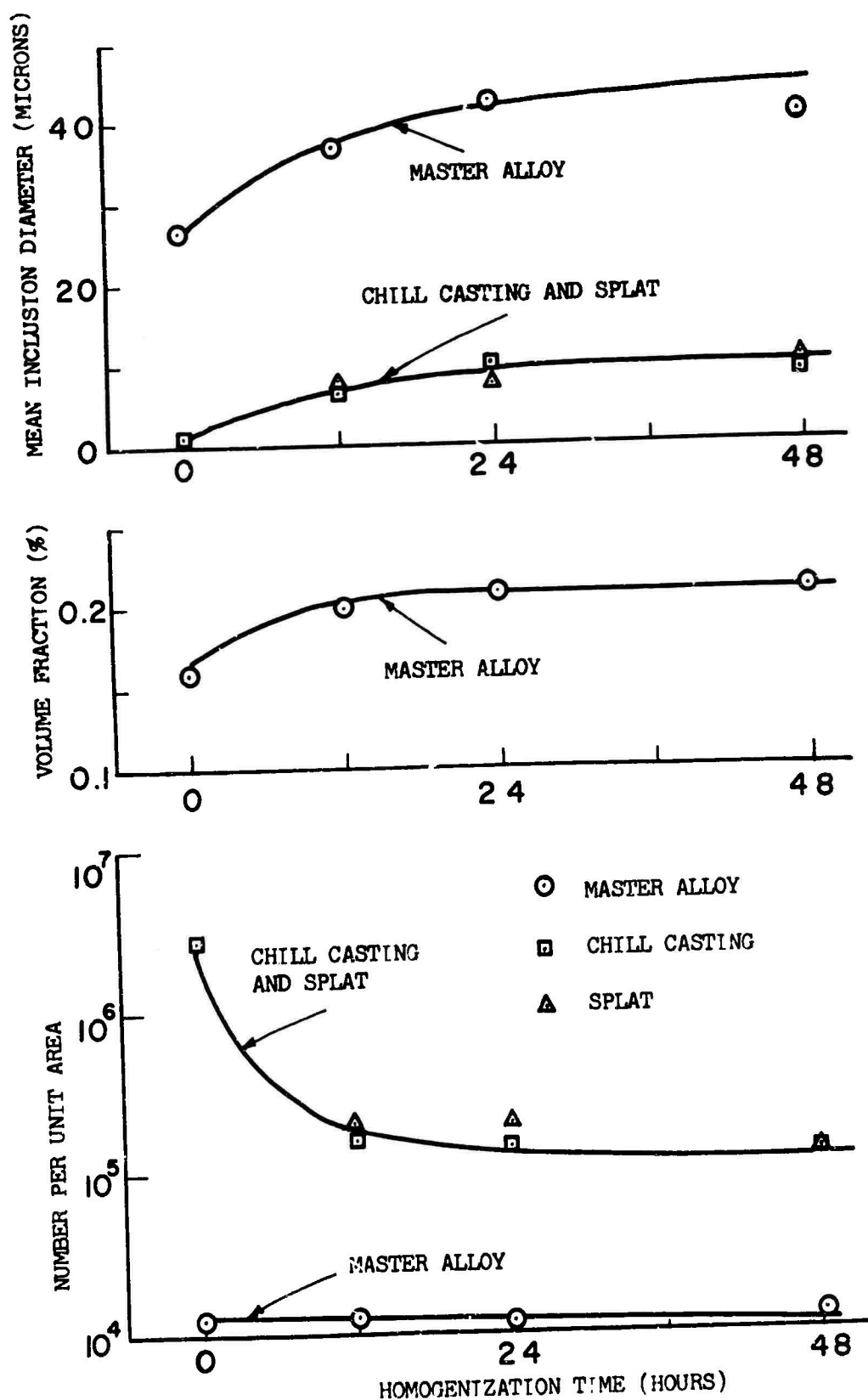
Figure 2-4. Variation of inclusion size (Top), volume fraction (Middle), and number per unit area (Bottom) versus homogenization time at 1400°C.

Chapter III

MECHANICAL BEHAVIOR OF INCLUSION BEARING IRON

Introduction and Literature Survey

Many studies of the effect of non-metallic inclusions formed
during solidification on the mechanical properties and fracture behavior of
iron have been completed. It has been observed that these microcracks
associated with inclusions are the cause of premature fracture and decreased
ductility in inclusion bearing alloys. Singh[1] has published a thorough
review of the mechanisms of initiation, growth, and coalescence of microcracks
resulting from either inclusion-matrix interface separation or inclusion
fracture during mechanical working. Tipnis and Cook[2] have described deformation
during necking of a tensile bar by means of rigid body rotation, leading in
the case of inclusions to inclusion-matrix interface separation. Liu[3] has
studied initiation of microcracks by inclusions in spherodized carbon steels.
Of special interest to this work is the prediction by Backofen that cracks
associated with inclusions are formed during heating or cooling due to
differential thermal expansion[4].

Ebeling and Ashby[5] have investigated the effect of SiO_2 inclusions
on the mechanical behavior of single crystals of copper; they find SiO_2
inclusions undeformed after severe matrix deformation. Although the volume
fractions and sizes of inclusions in Ebeling and Ashby's copper alloys were
such that the copper was dispersion hardened, they did observe an improvement
of properties with decreasing SiO_2 inclusion size. Pickering[6] has made a
study of the effects of mechanical working on the deformation of non-metallic
inclusions in the Fe-Si-O alloy system. Extensively deformed iron oxide and

ferro-silicate inclusions were observed optically after rolling. The
forces induced during deformation at the inclusion-matrix interface were
concluded to be of prime importance for the deformation and fracture of
the Fe-Si-O alloy. Gell and Leverant[7] studied the effect of MC-type
carbides on the fatigue properties of Mar-M200 nickel-base superalloy.
They utilized scanning and transmission electron microscopy to examine
fracture surfaces.

Non-metallic inclusions in metal matrices have been observed
extensively by optical and electron microscopy. O. Johari[8] has observed
extremely small carbide precipitates in steel using thin film transmission
electron microscopy. Minkoff and Nixon[9] have utilized the great depth of
focus of the scanning electron microscope to observe the morphology of
graphite growth in iron and nickel alloys. Observations of inclusions
in the dimpled region of a ductile fracture surface have been made on the
scanning electron microscope by Baker and Smith[10] in the copper-cuprous
oxide system, and cited by Finniston in his 1968 Hatfield Memorial Lecture[11].

In this work, fracture behavior of high purity iron was studied,
as influenced by simple SiO_2 and FeO inclusions. The volume fractions of
inclusions in the FeO bearing iron was exactly that in the SiO_2 bearing
alloy, Table 1. Since both types of inclusions appeared spherical in the
scanning electron microscope at greater than 10,000X, Figures 2 and 5,
the inclusion shape factor was constant. Also, both types of inclusions
appeared to be randomly positioned in the iron matrix, so this factor was
also constant. The two parameters to be studied in this work were inclusion
size and inclusion type (chemistry and structure). Master alloys, chill

castings, and splats with successively finer distributions of inclusions were tested in tension. Glassy SiO_2 inclusions and crystalline FeO inclusions were compared for their effect on mechanical behavior of iron.

Procedure

The fracture surfaces of tensile test bars were examined directly in the scanning electron microscope. Electropolished and mechanically polished surfaces of the as cast alloys and the surfaces of the reduced sections of the test bars were also examined in the scanning electron microscope. Fractured and electropolished specimens were stored in a vacuum of 10^{-4} torr before examination on the scanning electron microscope to prevent any surface contamination. Other than cutting the specimen to the proper size, no specimen preparation is required for the scanning microscope.

Results

The first fracture surface to be examined was that of the base material, Ferrovac "E" iron, shown in Figure 1 . As can be seen, necking continues to a virtual line where the characteristic dimples of a ductile fracture are evident. Extensive slidir.g off is observed in the necked region adjacent to the fracture surface. Even at 6500x, Figure 1d, no inclusions could be observed in the fracture surface (especially in the dimples) of Ferrovac "E".

Next a fractured test bar made from the Fe-0.05%Si master alloy, mean true SiO_2 diameter = 3.4µ was examined, Figure 2 . In this case, although the macroscopic deformation structure resembles the Ferrovac "E" test bar, many of the dimples on the fracture surface contain spherical SiO_2 inclusions. The inclusions are severely displaced, indicating inclusion-matrix interface separation. No SiO_2 inclusions were observed to be fractured.

Similar behavior on a much smaller scale was observed in the Fe-0.05%Si alloy chill casting, Figure 3 . Here the SiO_2 inclusions, mean true diameter = 0.12µ , are also perfectly spherical and also are present in the dimples of the fracture surface. No inclusions could be observed in the fracture surface of the Fe-0.05%Si alloy splat, Figure 4.

The fracture surface of a test bar of the Fe-0.07%O master alloy containing spherical FeO inclusions, mean true diameter = 5.2 was observed in the scanning electron microscope. Again, Figure 5,

the fracture surface shows dimples containing spherical inclusions, in this case FeO. The slightly larger size of FeO inclusions in the Fe-0.07%O alloy as compared to the SiO_2 inclusions in the Fe-0.05%Si alloy results in the more pronounced void coalescence observed in Figure 5, as compared to Figure 2 . Similar behavior is evident in the Fe-0.07%O chill casting, shown in Figure 6 .. No inclusions could be observed in the fracture surface of the Fe-0.07%O splat, Figure 7.

Observations were also made on the necked regions of the fracture surfaces of the master alloys. According to Tipnis and Cook[2] rotation occurs in the noncentral fracture region, i.e. the shear zone adjacent to the dimples in the central fracture region. The results of such rotation are observed in Figures 8,9 for the Fe-0.05%Si and Fe-0.07%O alloys. That the observed inclusion matrix interface separation has resulted from rotational type deformation seems apparent. The first impression of "balls rolling down a trough" is not far from correct, except that the troughs (voids) are being created by the deformation process.

Electropolished and mechanically polished sections of both the Fe-0.05%Si and Fe-0.07%O master alloys were investigated in the scanning microscope to determine the as cast morphology of the SiO_2 and FeO inclusions, the iron matrix, and the inclusion-matrix interface. The Fe-0.05%Si master alloy exhibited intact spherical inclusions with no inclusion-matrix interface separation, Figure 10. The Fe-0.07%O master alloy, however, exhibited extensive inclusion breakage and inclusion-matrix separation, Figure 11. Some of the inclusions also appear to be ferrosilicates instead of FeO, especially those broken upon solidification. What are apparently solidification shrinkage holes are observed on the surface of the FeO inclusions.

The electro-polished sections of test bars of the master alloys and chill castings of the Fe-0.05%Si and Fe-0.07%O alloys were examined in the scanning electron microscope. Test bars strained to 5% elongation and to necking (then unloaded) as well as a fractured bar of Fe-0.05%Si master alloy exhibited increasing amounts of inclusion-matrix interface separation with increasing strain in their reduced sections, Figures 12, 13, and 14. No SiO_2 inclusions were observed to be broken. A fractured test bar of Fe-0.07%O master alloy exhibited in its electro-polished reduced section severe inclusion-matrix separation and some severely fractured FeO inclusions, Figure 15. This behavior continued well back of the fracture surface. Behaviors similar to those of the master alloys, but on a much smaller scale, were observed in the Fe-0.05%Si and Fe-0.07%O chill castings, Figures 16 and 17.

Discussion

The fracture surfaces of the two alloys studied herein appear very similar, with slightly more evidence of void coalescence associated with the FeO inclusions. Rotation during the deformation, as observed by Tipnis and Cook[2], results in the "ball in a trough" appearance of the inclusions and dimples on the fracture surface. The polished reduced sections of the two alloy test bars did show a marked difference in behavior of FeO and SiO_2. Although inclusion-matrix interface separation was observed in both cases, the FeO inclusions were occasionally fractured, while the SiO_2 inclusions were always intact, Figures 14 and 15. This result along with the resulting microcracks is shown schematically in Figure 18. The work of Singh in the fracture of aluminum[1] has demonstrated that the lenticular-shaped void resulting from an inclusion-matrix interface separation is easier to propagate than the blunted void resulting from a fractured inclusion. However, Gell and Leverant[7], working on MC-type carbides in the nickel-base superalloy, Mar-M200, found that in fatigue testing fractured carbide inclusions in the as cast Mar-M200 structure were more important in the initiation of cracks than micropores. While the SiO_2 inclusion bearing iron showed no voids associated with inclusions in the as cast structure in the scanning electron microscope, the FeO inclusion bearing iron showed both inclusion fracture and inclusion-matrix interface separation in the as cast structure, Figures 10 and 11. Thus the Fe-0.07%O alloy has "cast in" voids that could cause poor mechanical performance.

Differences in the solidification shrinkage and thermal expansion of Fe, FeO, and SiO_2 cause the differing as cast soundness of the Fe-0.05%Si and Fe-0.07%O alloys. Since the SiO_2 inclusions are observed to be glassy, no abrupt solidification shrinkage and little thermal contraction occurs. For pure iron the solidification shrinkage is several percent,

and for FeO the shrinkage is expected to be larger. The FeO, furthermore, solidifies well after it is surrounded by solid iron and the solidification shrinkage should, therefore, appear as a void in the final structure; the internal voids in Figures ?1, 15, and 17 presumably result from this shrinkage.

Differential thermal contraction between the crystalline or glassy inclusion particles and the matrix must result in either internal stresses, inclusion-matrix interface separation, or cracking of the inclusion or matrix. Data for the thermal expansion of Fe, FeO, and SiO_2 are presented in Figure 19. Since high temperature data is not available, consider thermal expansion due to heating ($L/L = 0$ at $T = 0^{\circ}C$) of FeO and SiO_2 in an iron matrix. Assume the inclusions are inserted into the matrix at $0^{\circ}C$ with no stresses or voids associated with them. Upon heating the SiO_2 inclusions would always be in tension. The FeO inclusions would expand the same amount as the matrix until the alpha to gamma transformation where it would go into compression. Just the reverse of the above hypothetical process should take place upon solidification. SiO_2 is always in compression upon cooling, while FeO goes into tension at the delta to gamma transformation and possibly into compression at the gamma to alpha transformation. This tension could cause the observed inclusion-matrix interface separation in FeO such as that in Figure 11, or inclusion fracture in FeO as in Figure 11. Inclusion fracture or inclusion-matrix interface separation has not been observed in this work for the case of SiO_2 inclusions in the as cast Fe-0.05%Si alloy, Figure 10.

Chill casting test bar fracture surfaces, Figures 3 and 6, resemble master alloy fracture surfaces, Figures 2 and 5, on a much smaller

scale for both alloys, i.e., smaller dimples and inclusions in the chill casting. Although still finer dimples appeared in the splat tensile bar fracture surfaces, Figures 4 and 7, these are not comparable to the dimples in the master alloy and chill casting, since no inclusions were resolvable in the splat fracture surfaces at 14,000X.

The results of the mechanical properties measurements on the Ferrovac "E", Fe-0.05%Si and Fe-0.07%O master alloys given in Appendix D suggest that the cast-in microcracks associated with the FeO inclusions in the Fe-0.07%O alloy as cast structure reduce its ductility as compared to the relatively high ductility observed in the Fe-0.05%Si alloy, where no microcracks are associated with the inclusions in the as cast structures. Additional testing would be necessary to verify this tentative observation.

REFERENCES

1. S. N. Singh, "Effects of Ingot Structure and Thermomechanical Processing on Properties of a Wrought High Strength Al-Alloy", Sc.D. Thesis, M.I.T., 1968.

2. V. A. Tipnis and N. H. Cook, "The Influence of Stress-State and Inclusion Content on Ductile Fracture With Rotation", Journal of Basic Engineering, Sept., 1967, pp. 533-540.

3. C. T. Liu and J. Gurland, "The Fracture Beha.'or of Spheroidized Carbon Steel", Trans. ASM, v. 61, 1968, pp. 156-167.

4. W. A. Backofen, "Fracture of Engineering Materials", ASM, Metals Park, Ohio, 1964, p. 107.

5. M. F. Ashby, "Work Hardening of Dispersion — Hardened Crystals", Phil. Mag. 14, 1966, pp. 1157-1178.

6. F. B. Pickering, "Some Effects of Mechanical Working on the Deformation of Non-metallic Inclusions", Journal of the Iron and Steel Institute, June, 1958, pp. 148-159.

7. M. Gell and G. R. Leverant, "The Fatigue of the Nickel-Base Superalloy, Mar-M200, in Single-Crystal and Columnar-Grained Forms at Room Temperature", Trans. Met. Soc. AIME, v. 242, 1968, pp. 1869-1879.

8. O. Johari and G. Thomas, "Structures and Strengths of Ausformed Steels", ASM Trans. Quart., v. 58, 1965, pp. 567-578.

9. I. Minkoff and W. C. Nixon, "Scanning Electron Microscopy of Graphite Growth in Iron and Nickel Alloys", J. of Appl. Physics, v. 37, 1966, pp. 4848-4855.

10. C. Baker and G. C. Smith, "Some Observations on the Ductile Fracture of Polycrystalline Copper Containing Inclusions", Trans. Met. Soc. AIME, v. 242, 1968, pp. 1989-1995.

11. H. M. Finniston, "Twenty-Five Years On", 19th Hatfield Memorial Lecture, Journal of the Iron and Steel Institute, Feb., 1969, pp. 145-153.
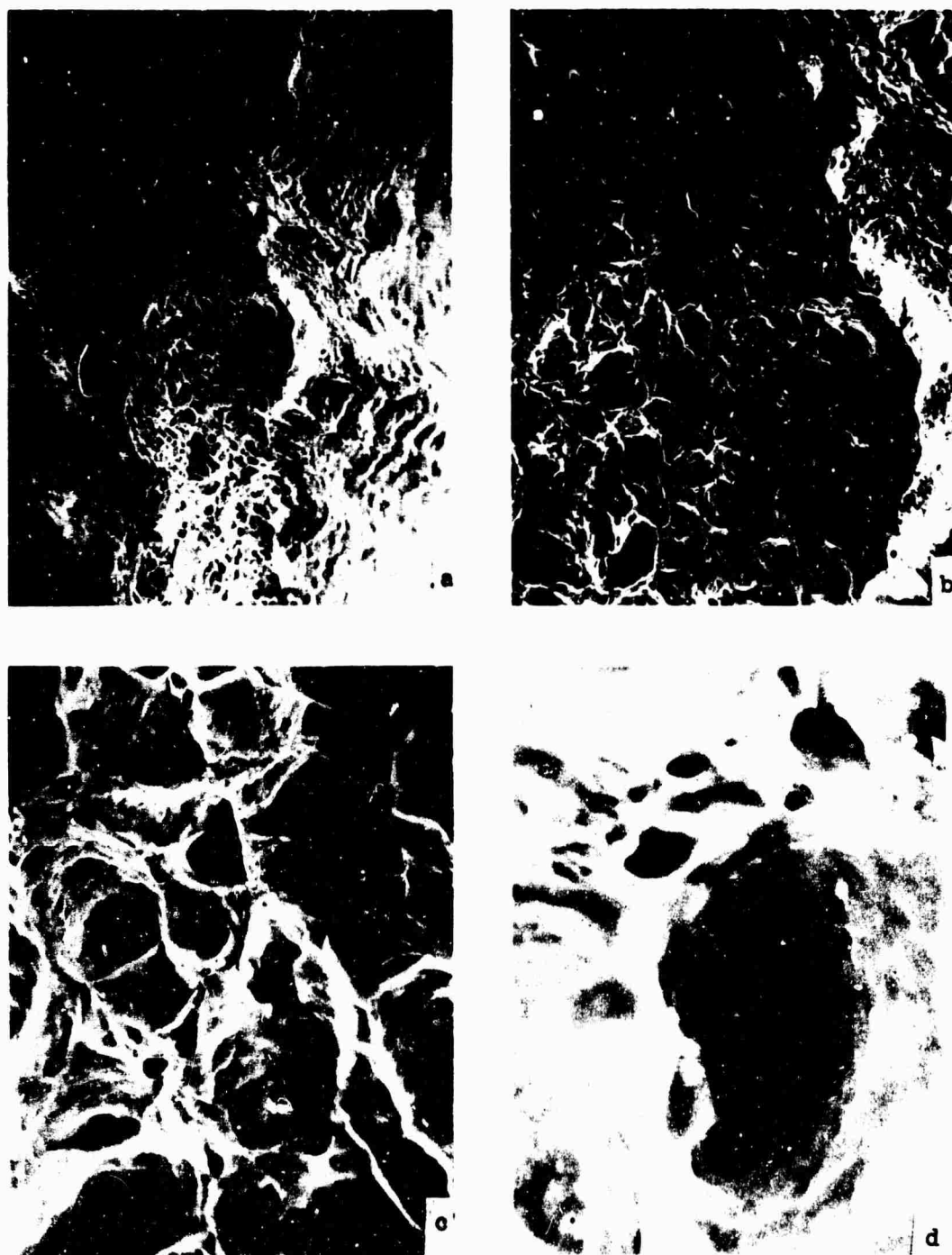
Figure 3-1. Fracture surface of Ferrovac "E" iron 1/2 inch
gage length test bar.
Magnification (a) 260X, (b) 650X, (c) 2600X, (d) 6500X.
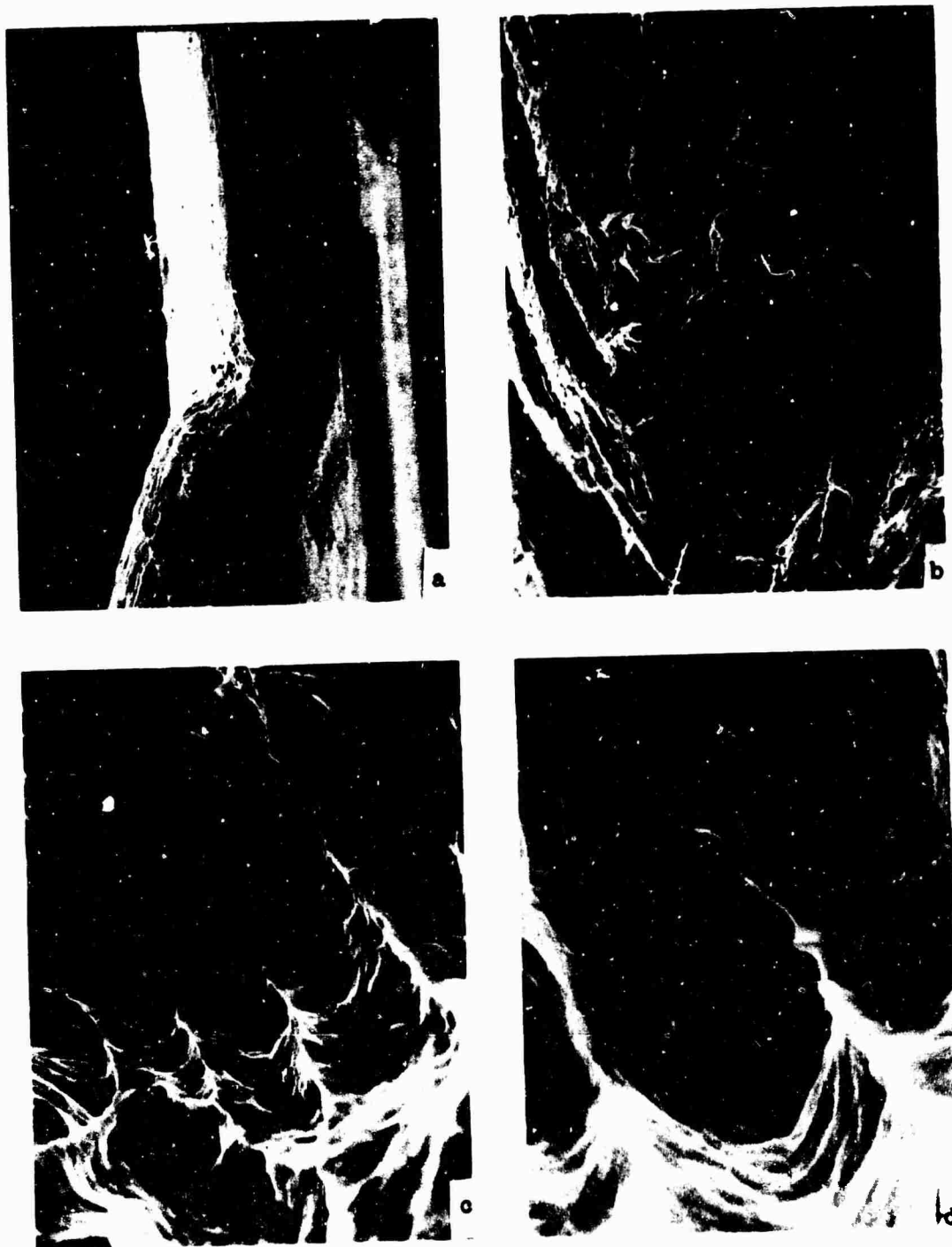
Figure 3-2.   Fracture surface of Fe-0.05%Si alloy 1/2 inch gage
length test bar.
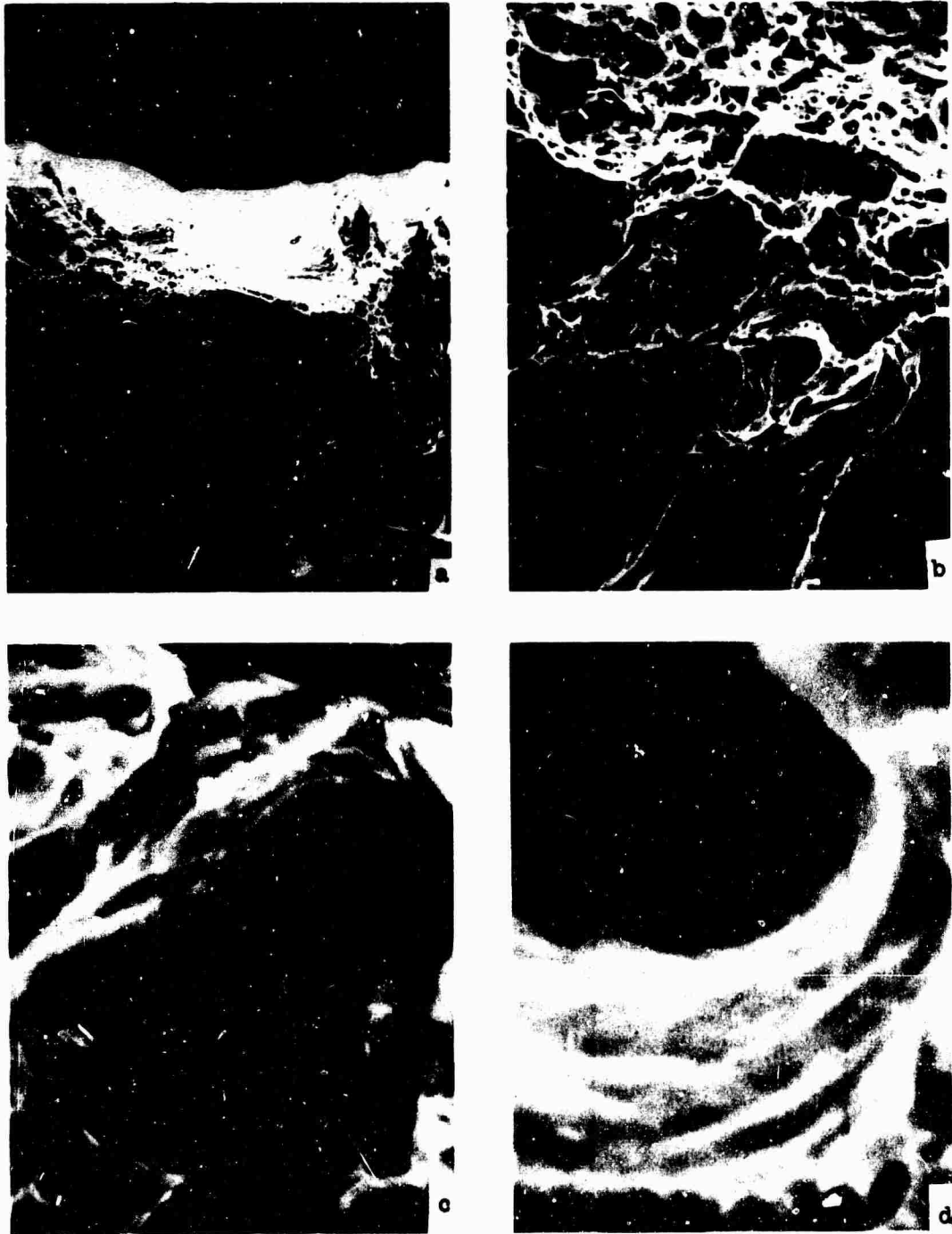Magnification (a) 650X, (b) 650X, (c) 2600X, (d) 6500X.

Figure 3-3. Fracture surface of Fe-0.05%Si chill casting 1/4 inch
gage length test bar.
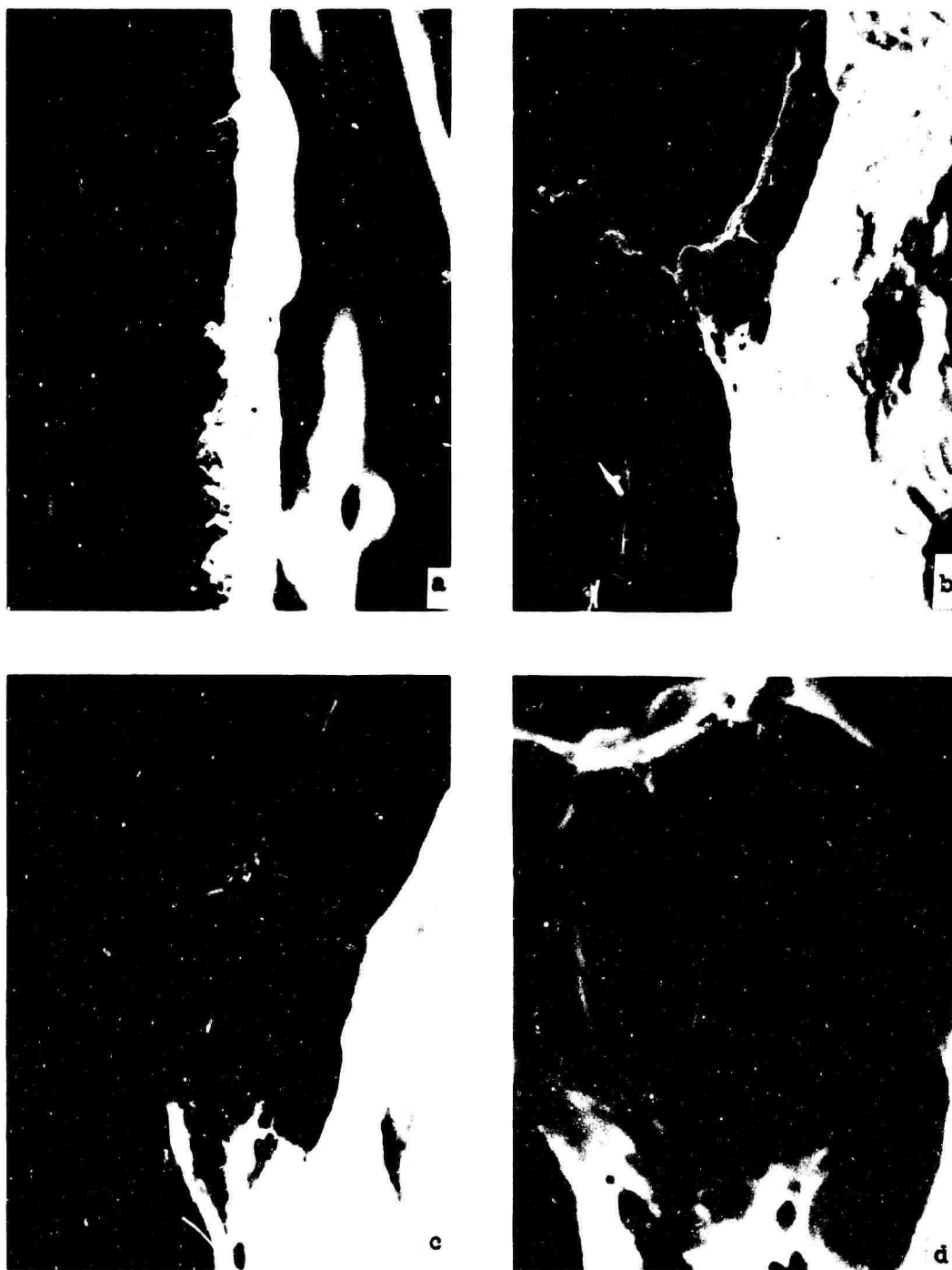Magnification (a) 140X, (b) 1,400X, (c) 7,000X, (d) 14,000X.

Figure 3-4. Fracture surface of Fe-0.05%Si splat 1/4 inch gage
length test bar.
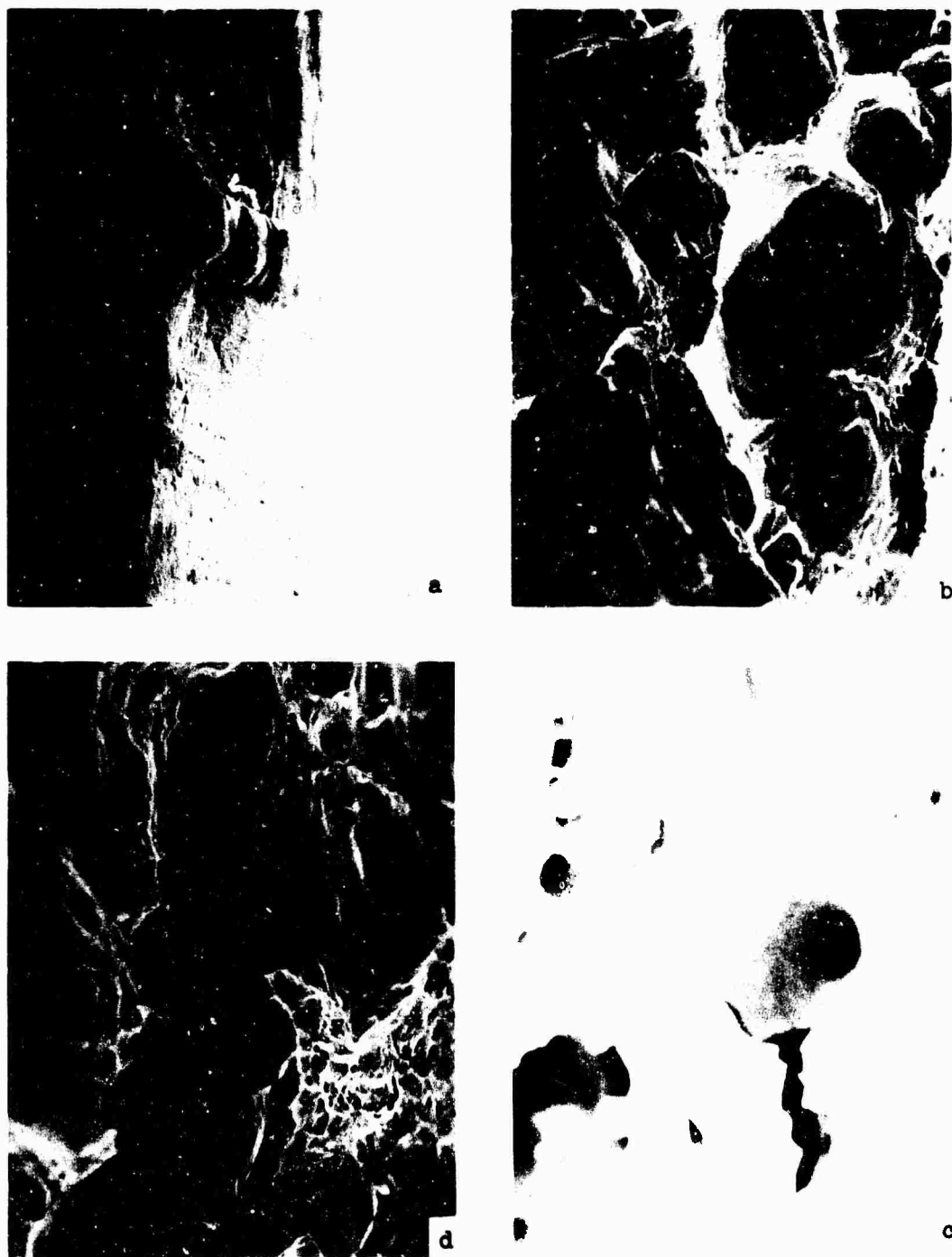Magnification (a) 140X, (b) 2,800X, (c) 7,000X, (d) 14,000X.

Figure 3-5. Fracture surface of Fe-0.07%O master alloy 1/2 inch
gage length test bar.
Magnification (a) 85X, (b) 850X, (c) 850X, (d) 1,800X.

Figure 3-6. Fracture surface of Fe-0.07%0 chill casting 1/4 inch
gage length test bar.
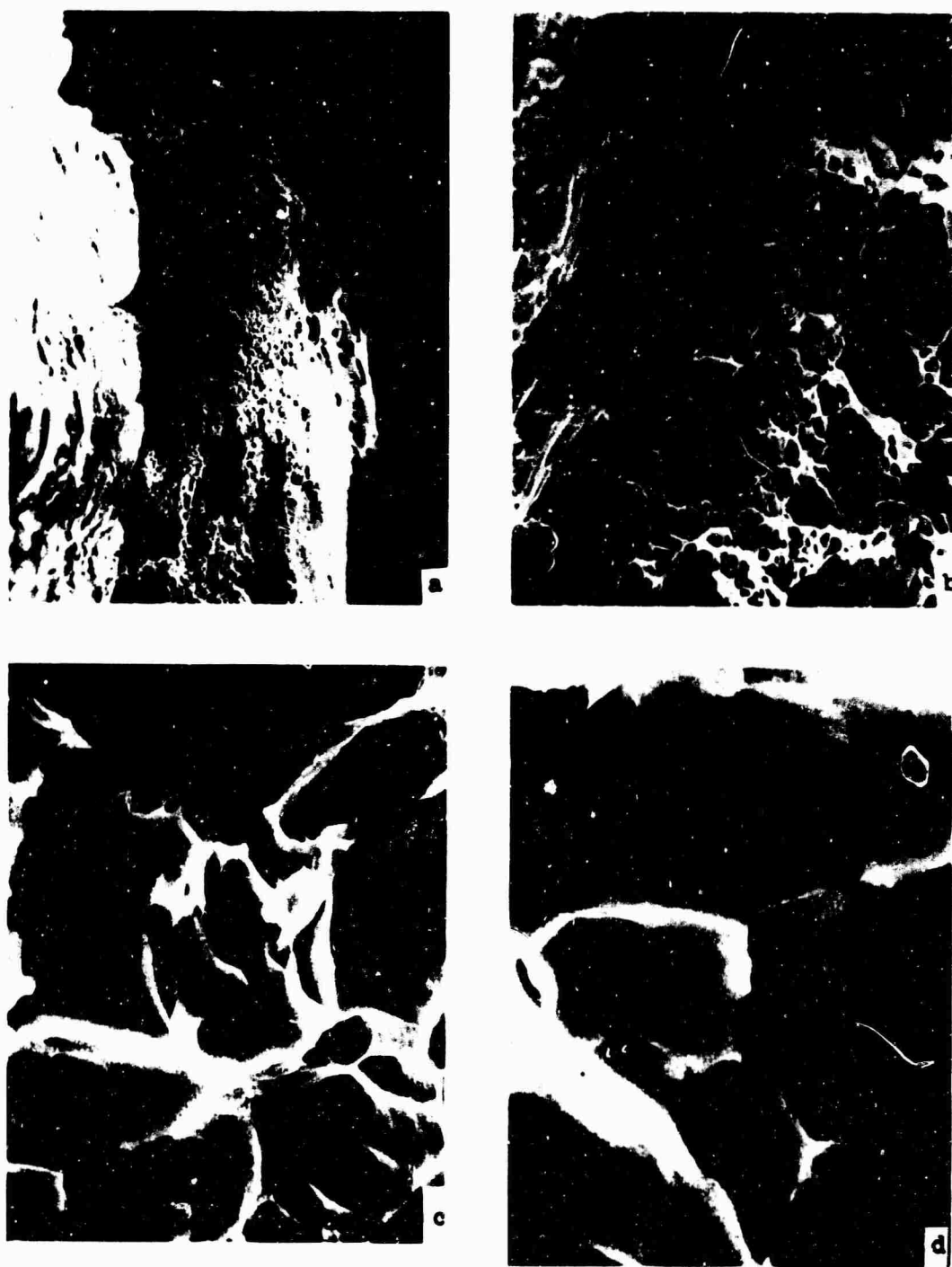Magnification (a) 360X, (b) 1,600X, (c) 8,000X, (d) 16,000X.
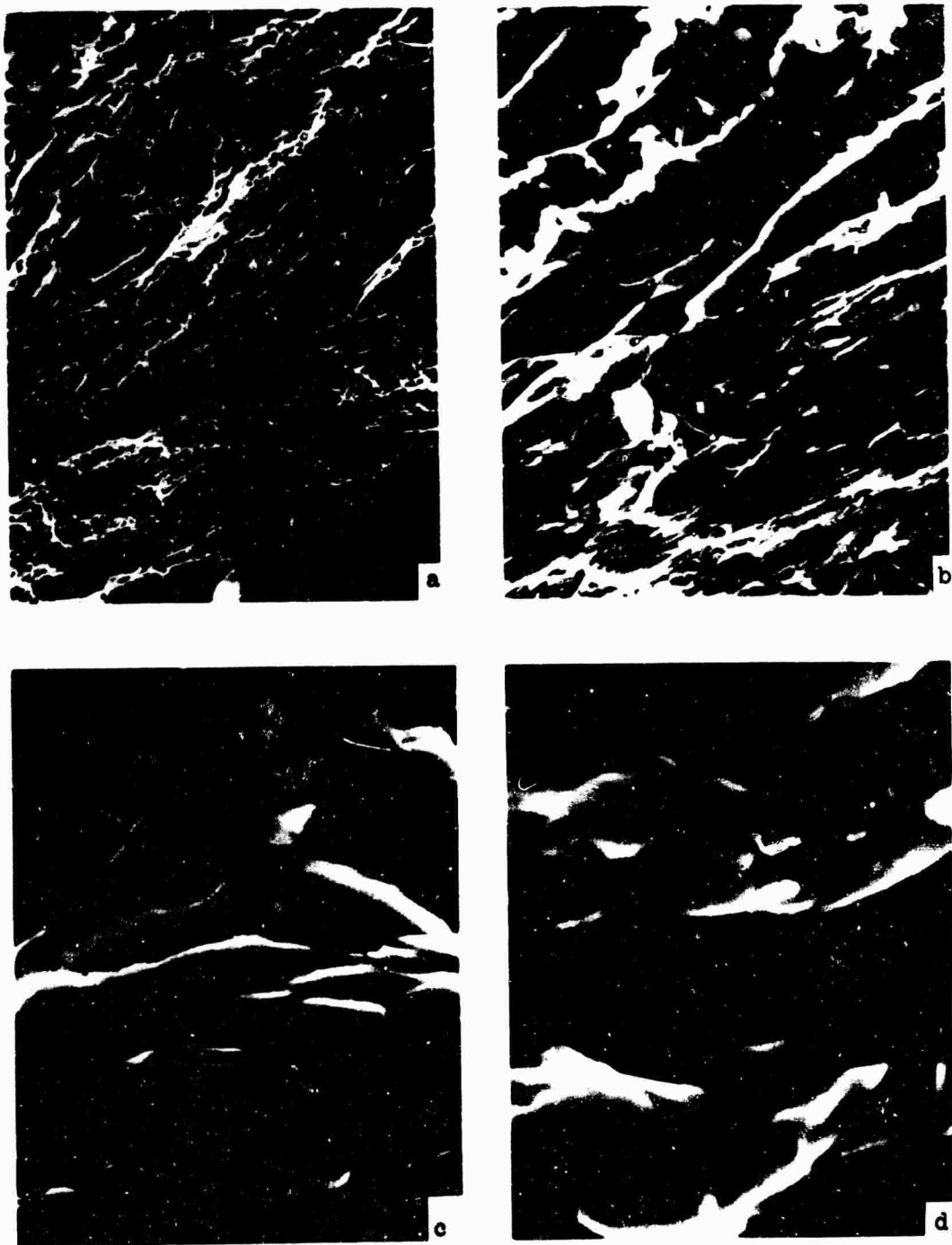
Figure 3-7. Fracture surface of Fe-0.07%O splat 1/4 inch gage
length test bar.
Magnification (a) 700X, (b) 2,800X, (c) 7,000X, (d) 14,000X.
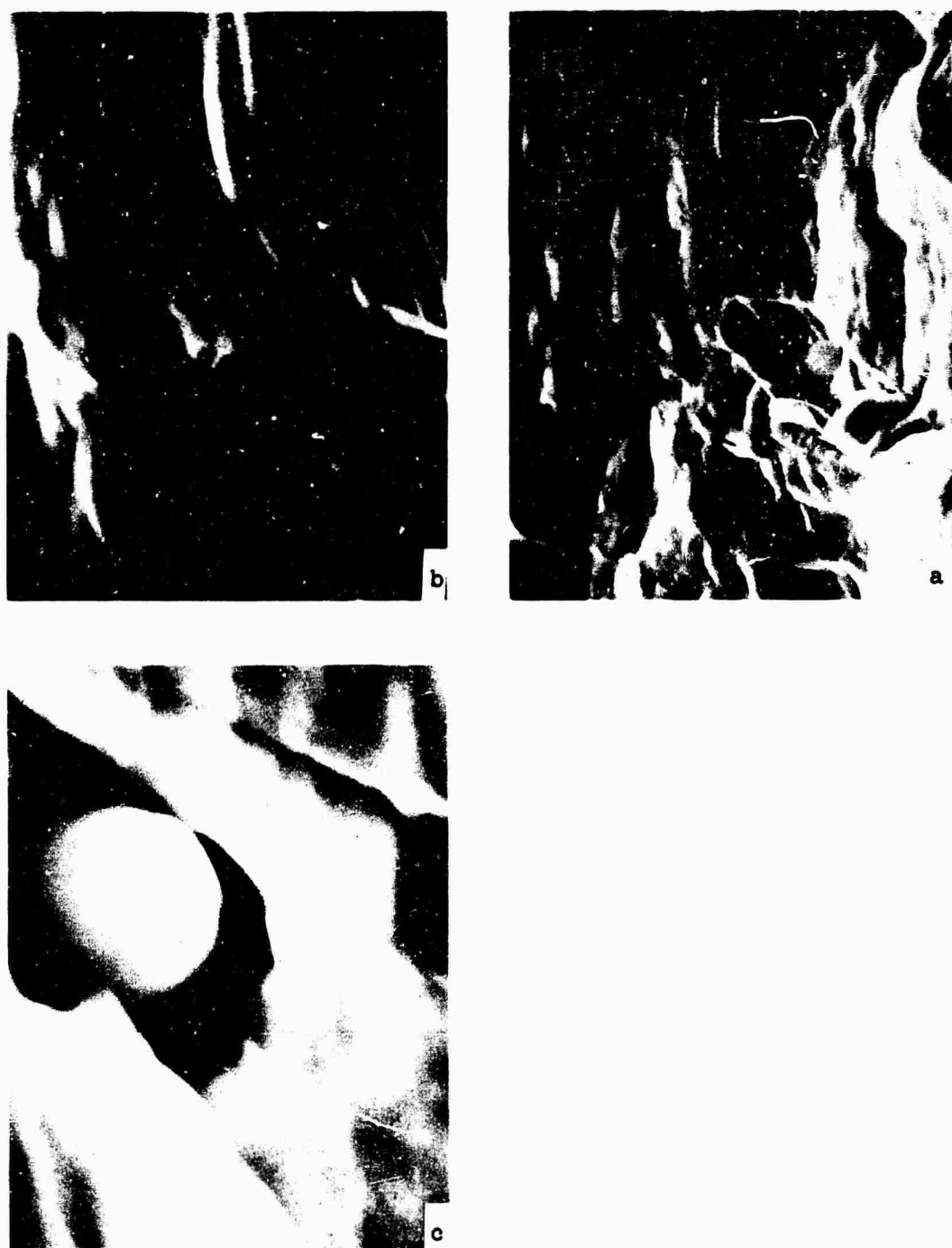
Figure 3-8. Necked region of the fracture surface of the Fe-0.05%Si
master alloy 1/2 inch gage length test bar.

Magnification: a. 2400X, b. 5500X, c. 12,000X.
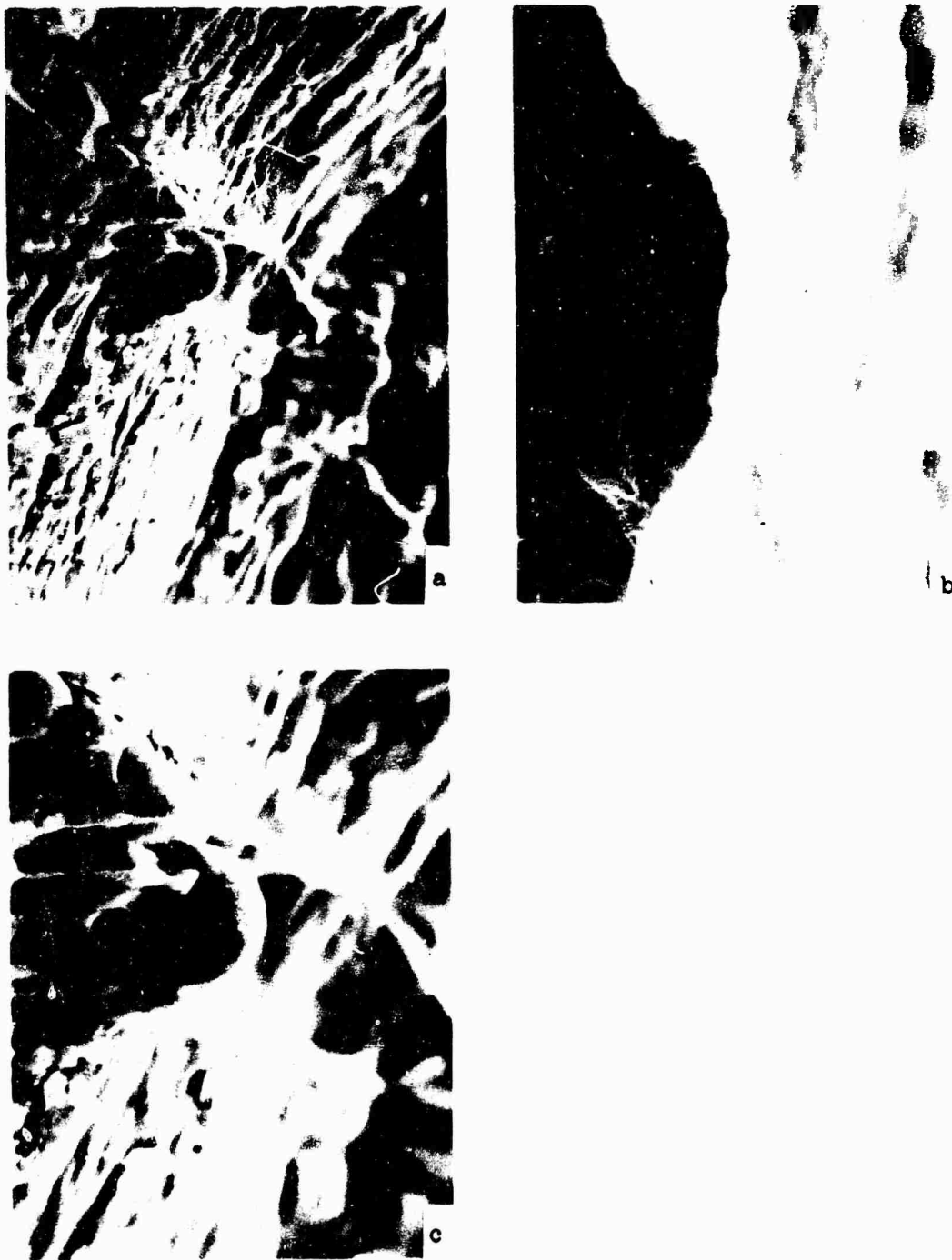
Figure 3-9. Necked region of the fracture surface of the Fe-0.07%O master alloy 1/2 inch gage length test bar. Magnification (a) 1,800X, (b) 3,600X, (c) 3,600X.
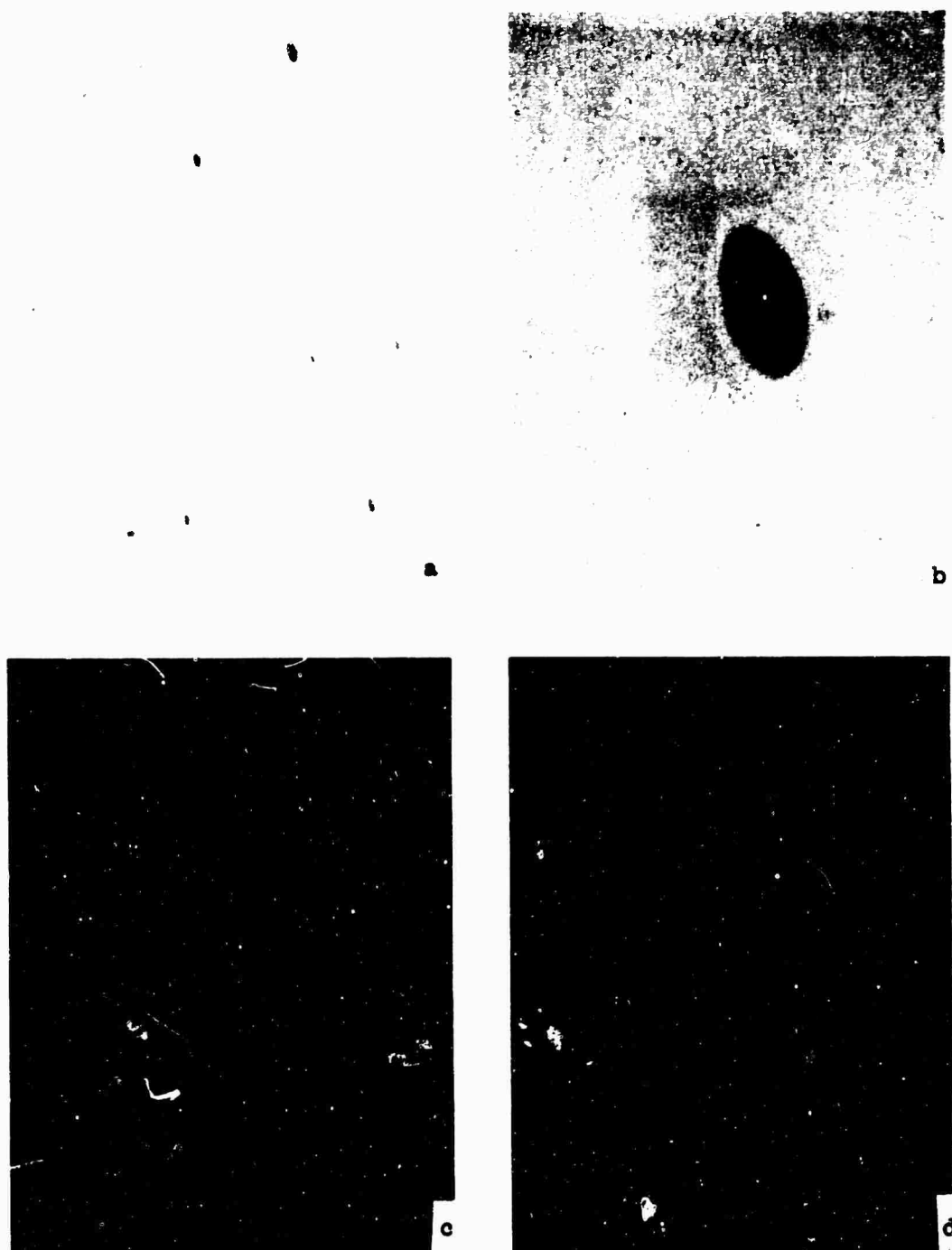
Figure 3-10.   Electropolished surface of the Fe-0.05%Si master alloy, as cast.
Magnification (a) 650X, 45 degree angle, (b) 6500X, 45 degree angle, (c) 650X, 90 degree angle, (d) 6500X, 90 degree angle.

82
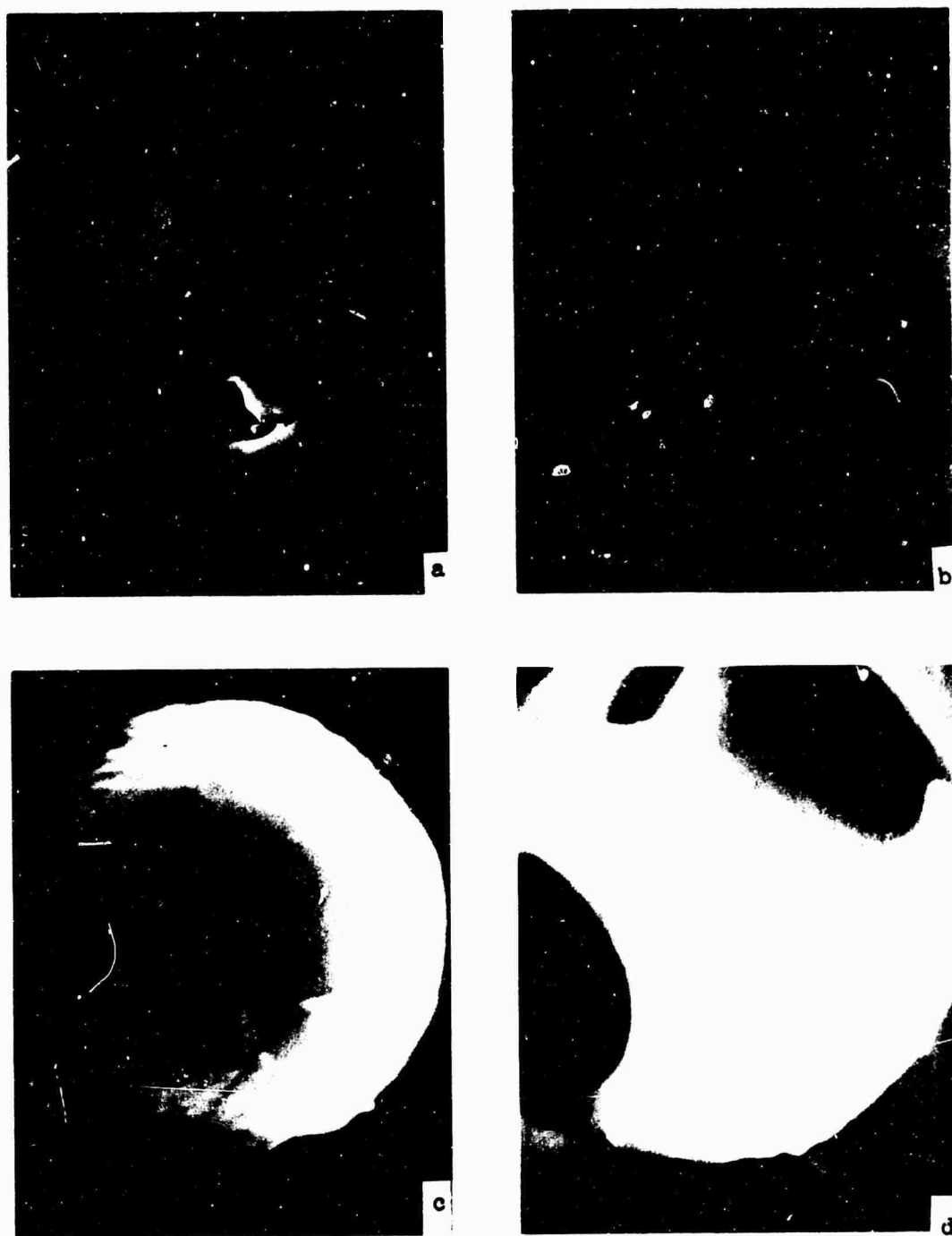
Figure 3-11. Electropolished and mechanically polished surfaces of
the Fe-0.07%O master alloy, as cast. (a) and (b) mechanically
polished, (c) and (d) electropolished.
Magnification (a) 2,600X, (b) 13,000X, (c) 12,000X, (d) 12,000X.
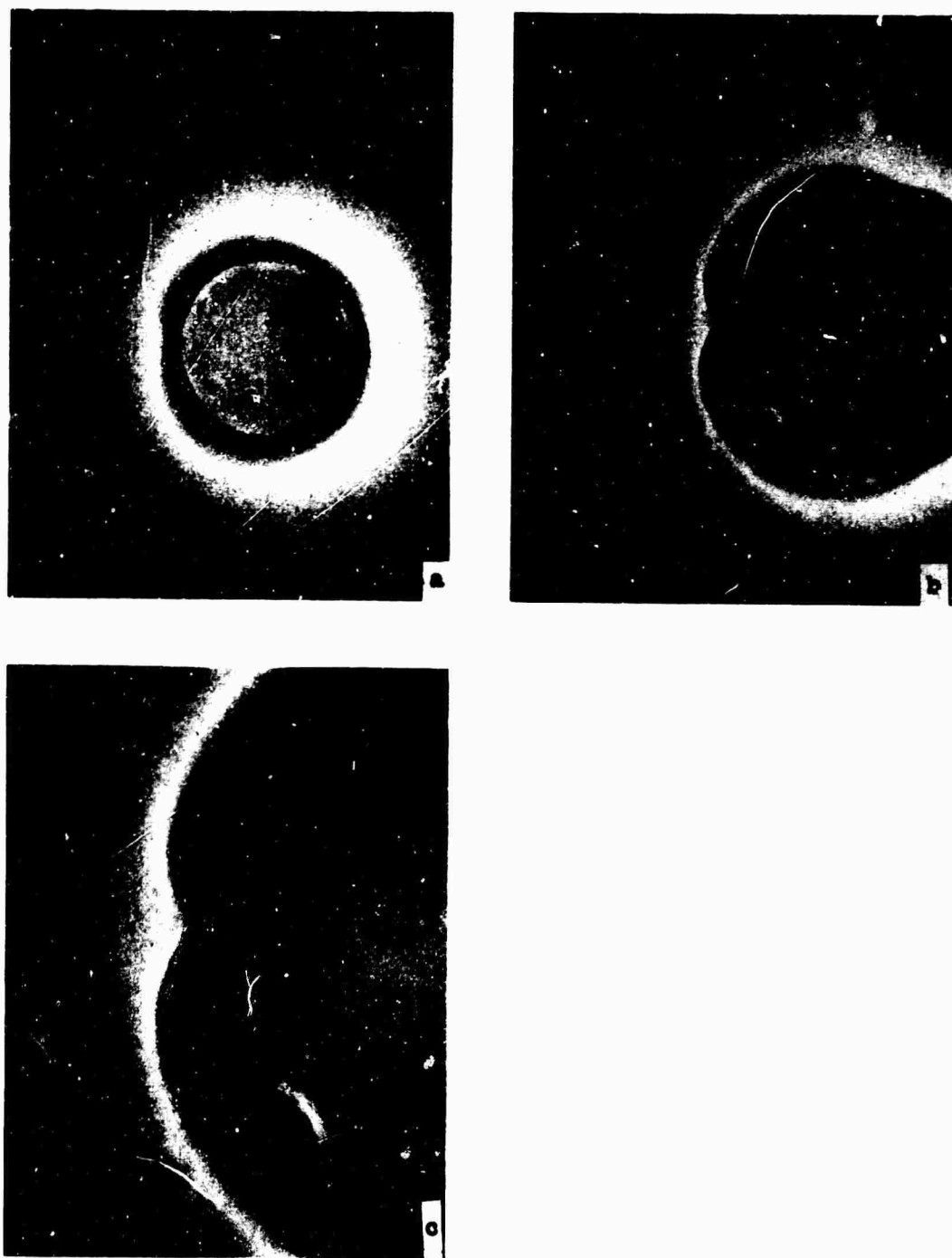
Figure 3-12. Electropolished surface of 0.05%Si-Fe master alloy 1/2 inch gage length test bar, strained to 5% elongation and unloaded. Horizontal tensile axis.
Magnification (a) 12,000X, (b) 12,000X, (c) 22,000X.
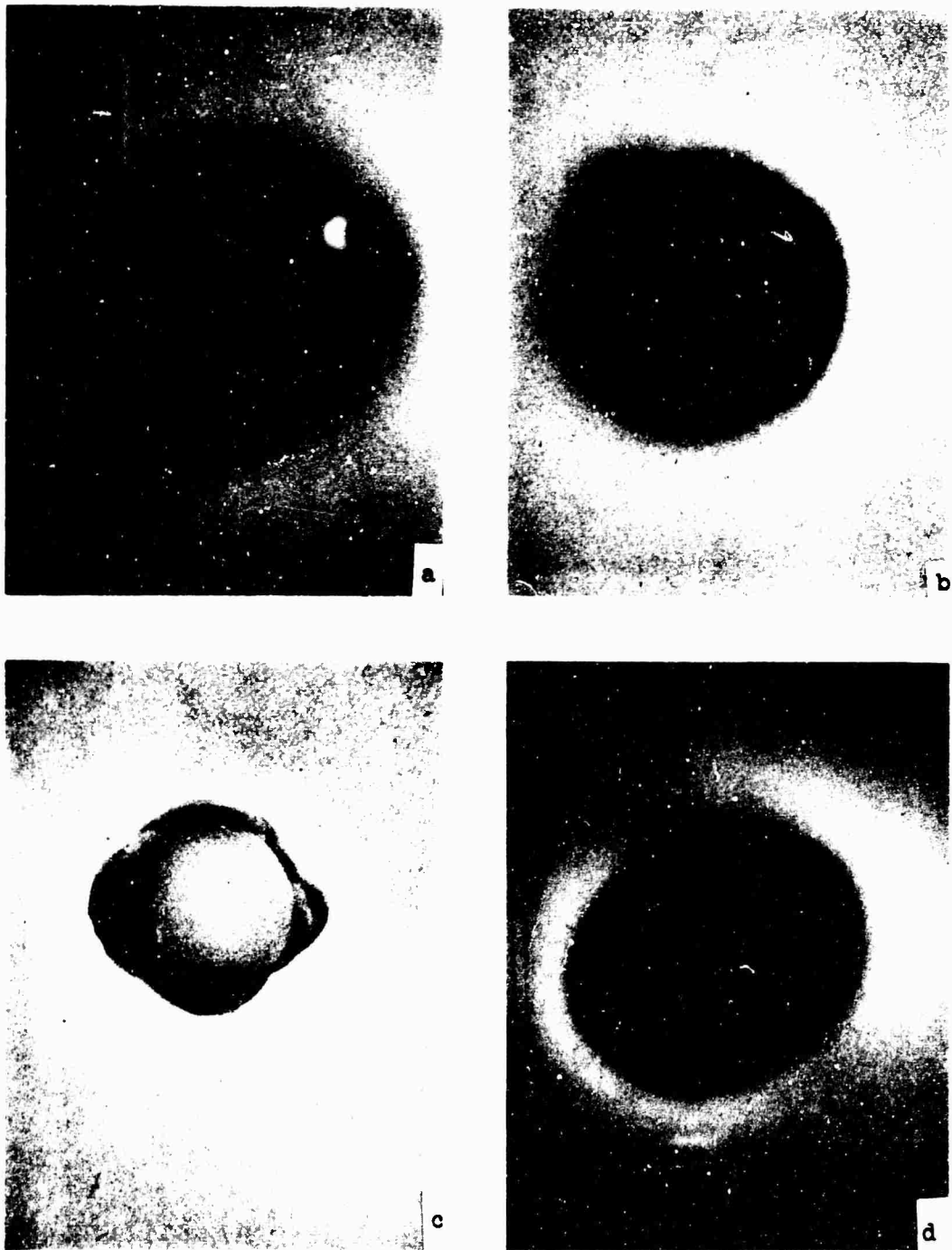
Figure 3-13.   Electropolished surface of the Fe-0.05%Si master alloy
1/2 inch gage length test bar, strained to necking and
unloaded. Horizontal tensile axis.
Magnification (a) 12,000X, (b) 12,000X, (c) 24,000X, (d) 24,000X.
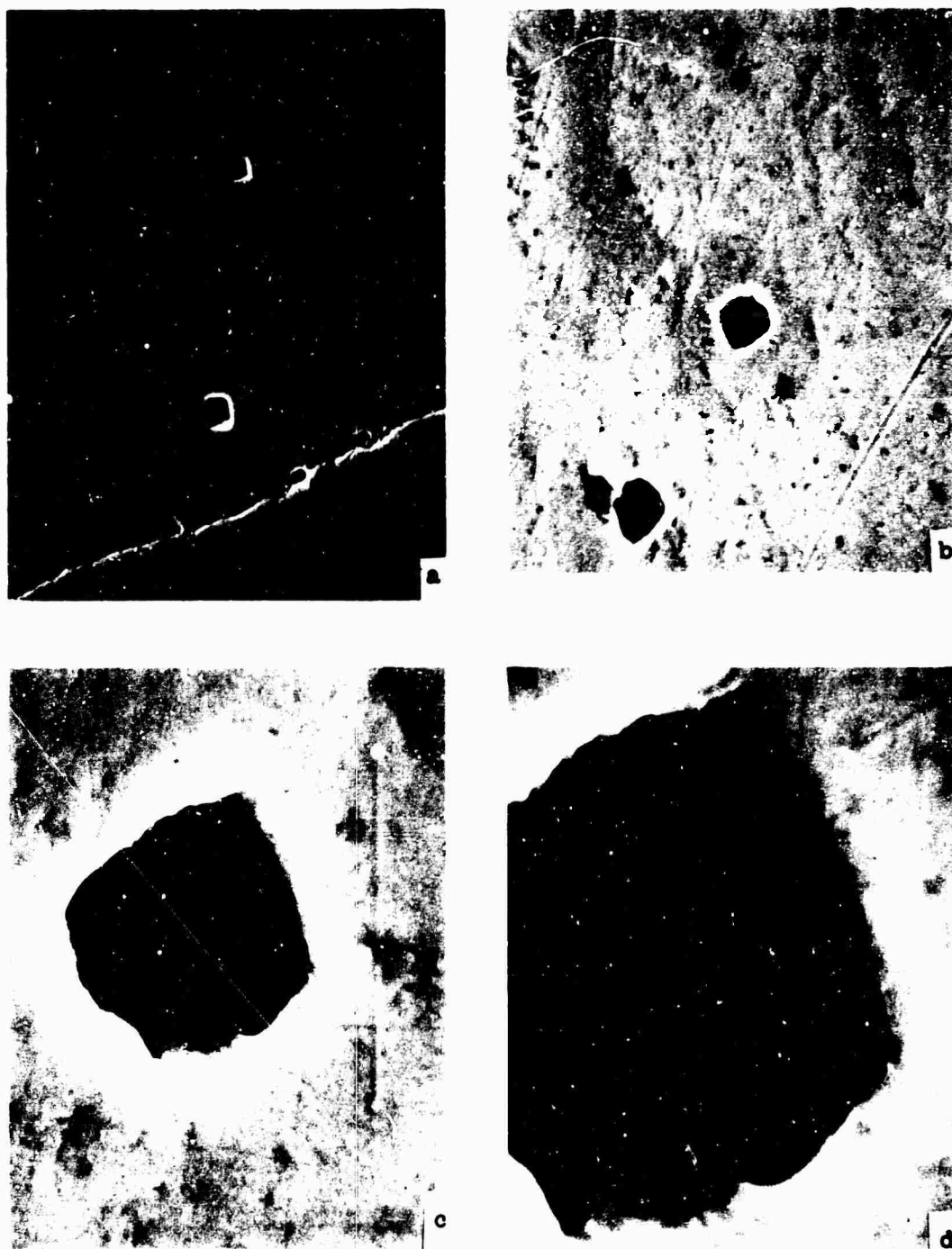
Figure 3-14. Mechanically polished surface of the Fe-0.05%Si master
alloy 1/2 inch gage length test bar, strained to fracture.
Horizontal tensile axis.
Magnification (a) 1,250X, (b) 2,600X, (c) 12,500X, (d) 26,000X.
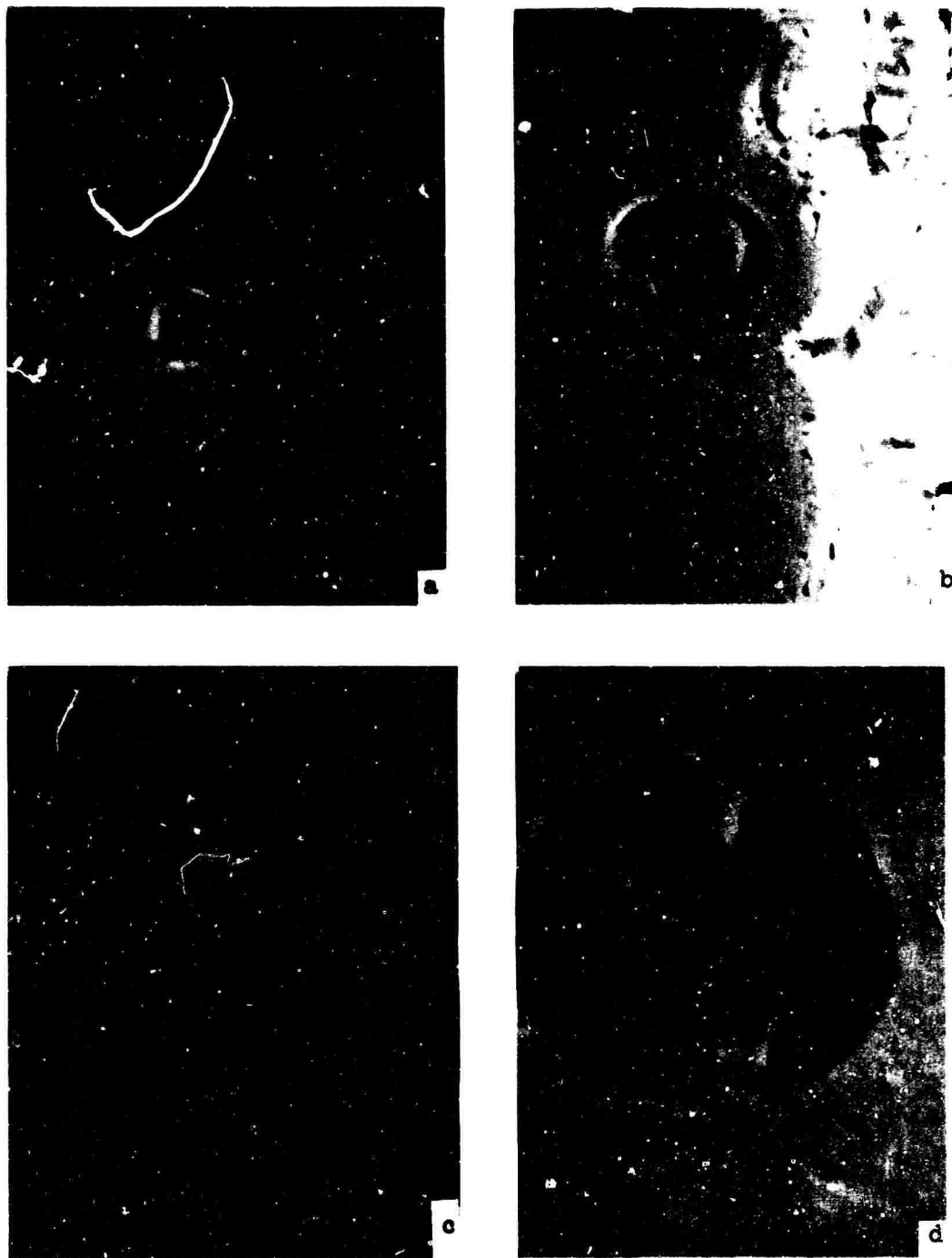
Figure 3-15. Electropolished surface of Fe-0.07%0 master alloy
1/2 inch gage length test bar, strained to fracture.
Horizontal tensile axis.
Magnification (a) 2,400X, (b) 5,500X, (c) 5,500X, (d) 5,500X.
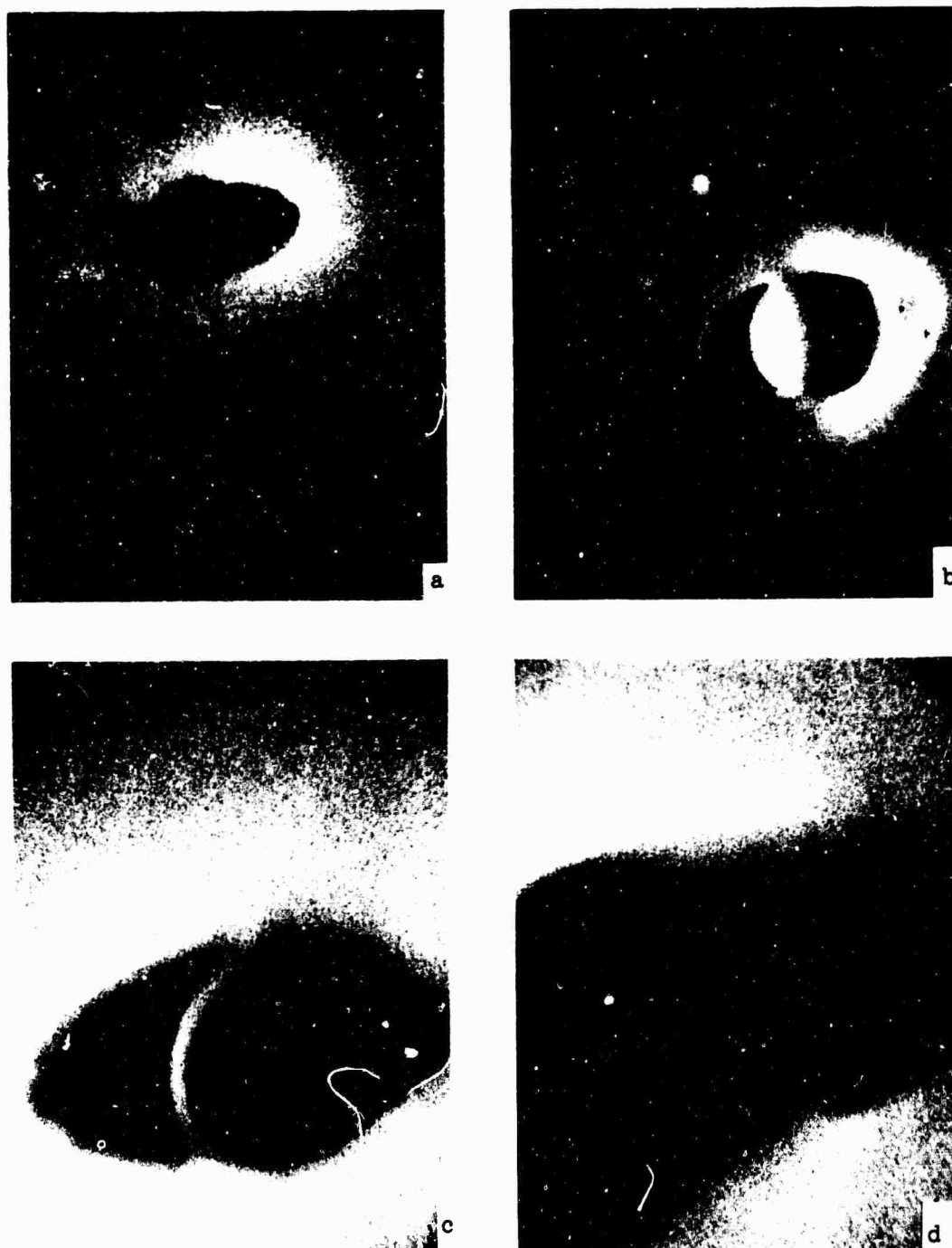
Figure 3-16. Electropolished surface of Fe-0.05%Si chill casting
1/4 inch gage length test bar, strained to fracture.
Horizontal tensile axis.
Magnification (a) 11,000X, (b) 22,000X, (c) 55,000X,
(d) 110,000X.
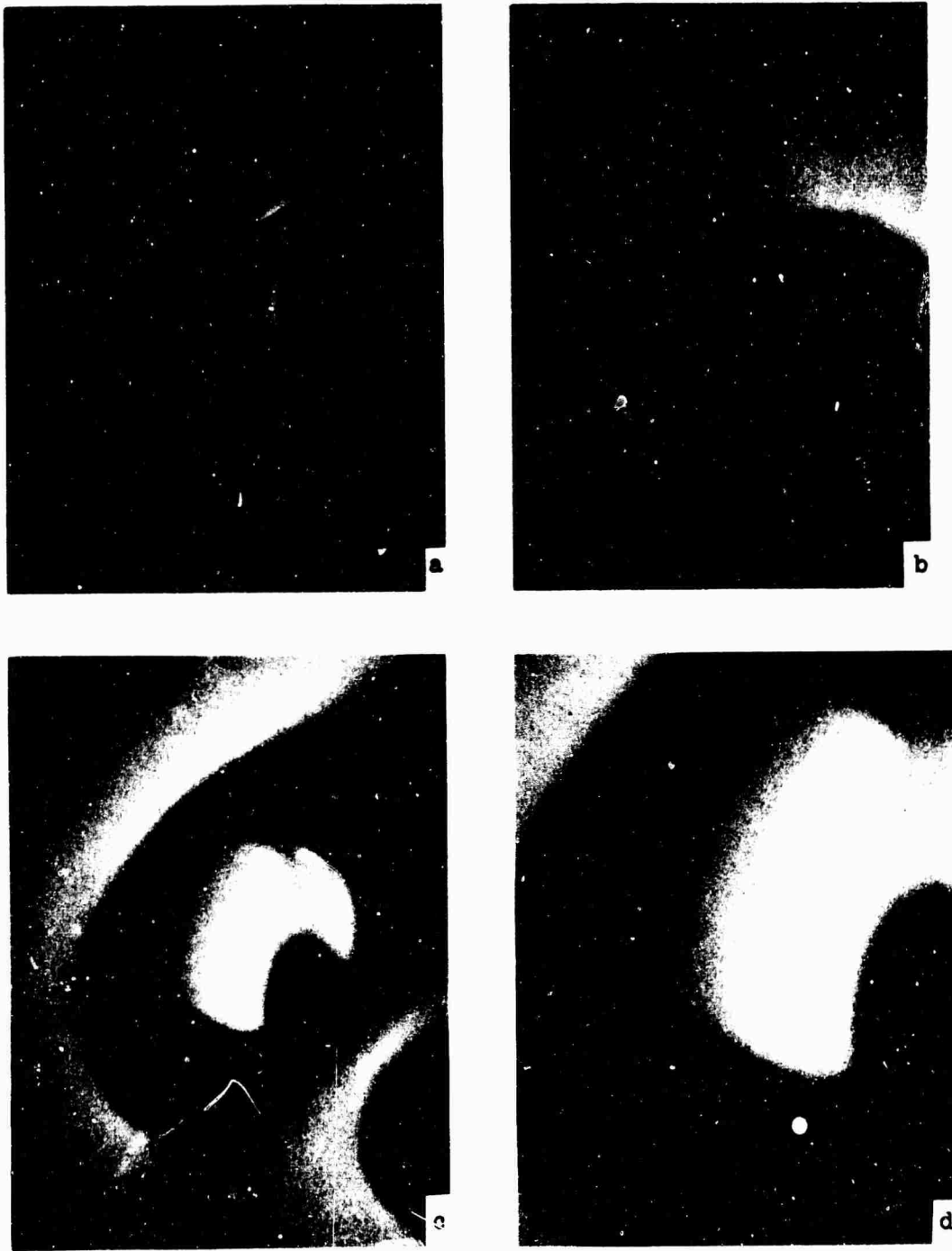
Figure 3-17. Electropolished surface of Fe-0.07%0 chill casting
1/4 inch gage length test bar, strained to fracture.
Horizontal tensile axis.
Magnification (a) 24,000X, (b) 60,000X, (c) 60,000X,
(d) 125,000X.
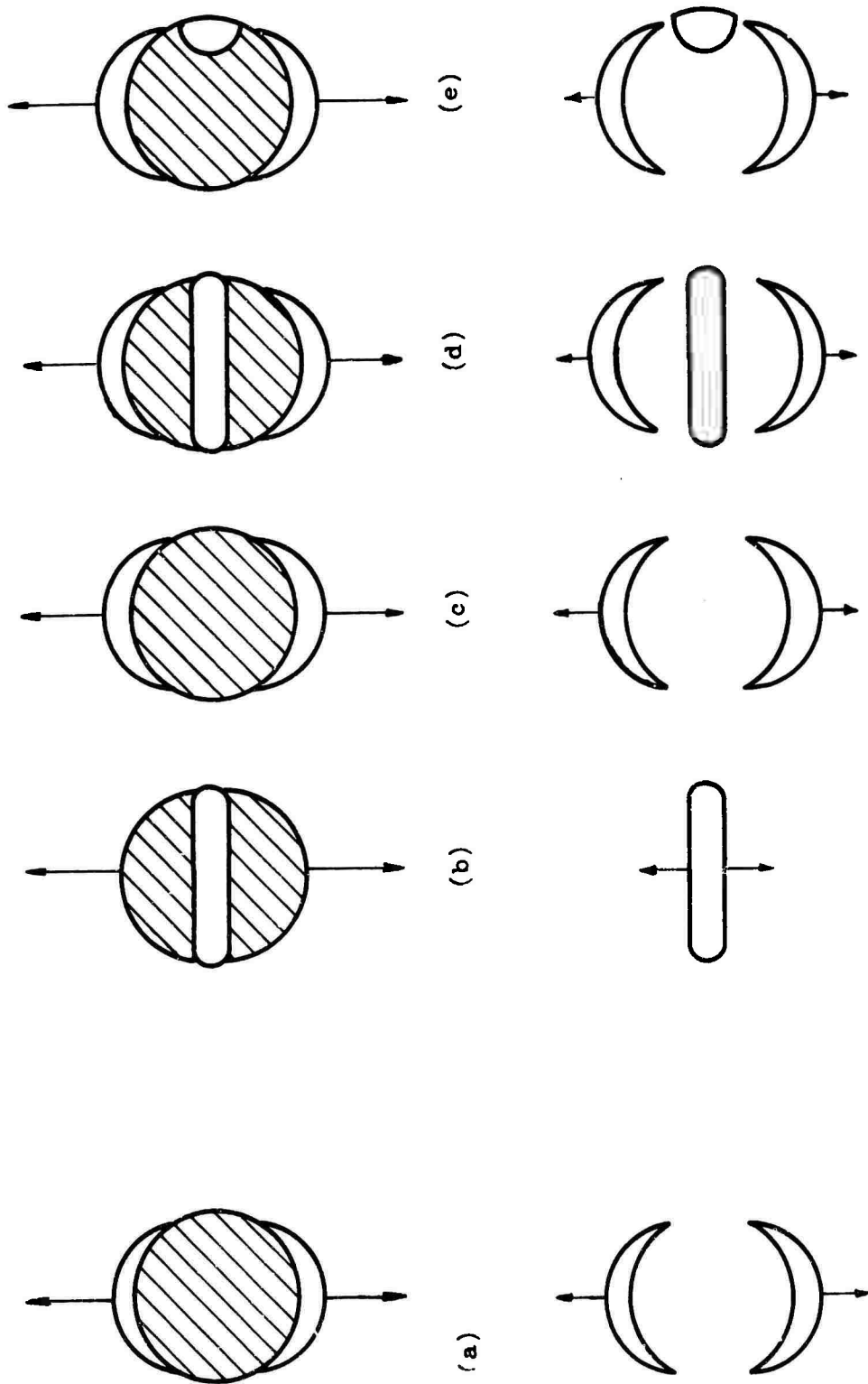
Figure 3-18. Schematic description of the deformation associated with FeO and SiO_2 inclusions during tensile testing. Top: Inclusions in the strained matrix. Bottom: Resulting microcracks. a. SiO_2 inclusions, b,c,d,e. FeO inclusions.
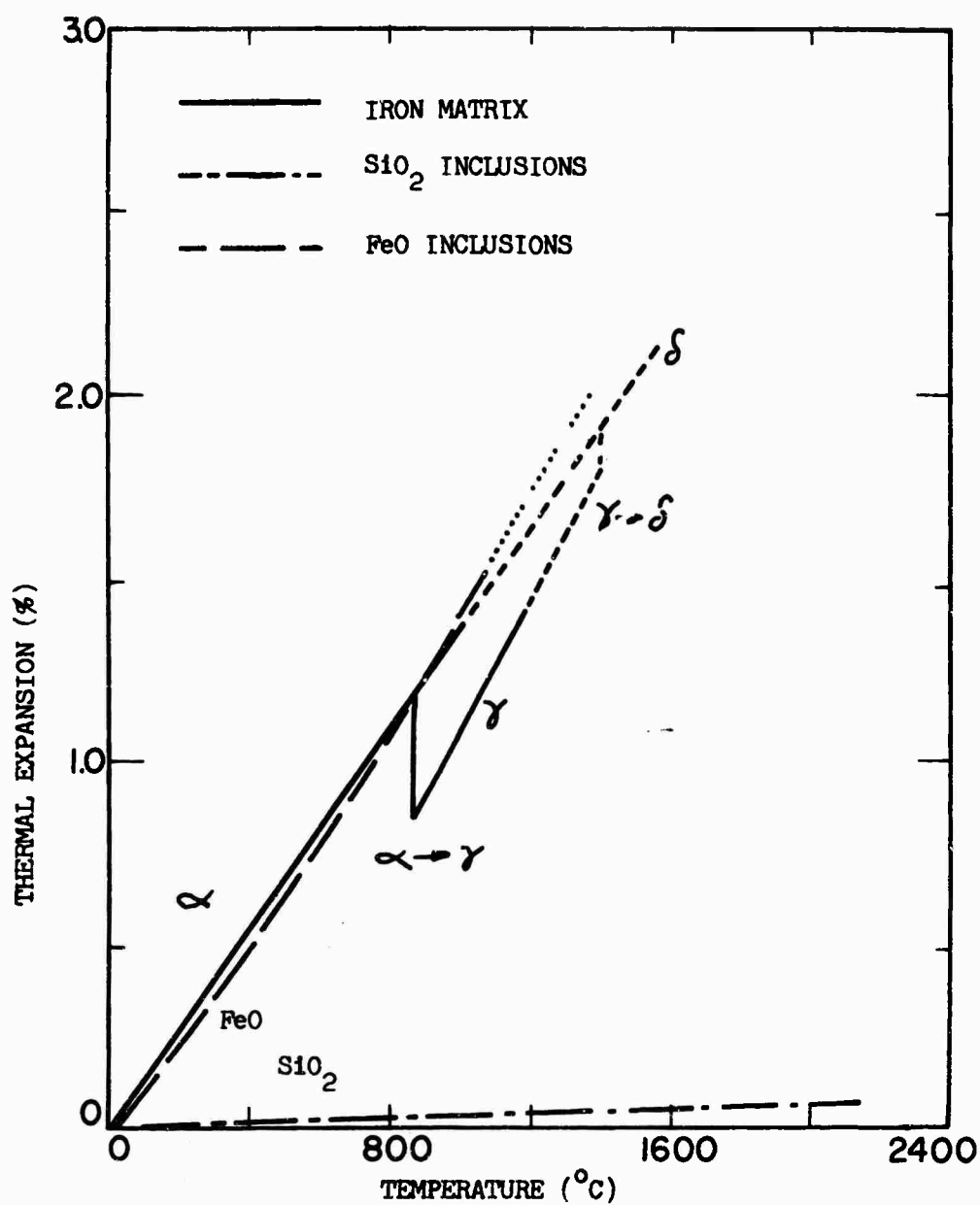
Figure 3-19. Thermal expansion of pure iron, FeO, and SiO_2.

CONCLUSIONS

1. A levitation melting, chill casting, and splat cooling device modified and developed in this investigation permits casting of small samples at cooling rates from $1^\circ C$/second to $10^6\ ^\circ C$/second.

2. Various microstructural features of iron base alloys were studied, including dendrites, lamellar eutectic, and non-metallic inclusions. These features are all refined by increasing cooling rate.

3. In the Fe-0.05%Si alloy splat, the SiO_2 inclusions are either surpressed or made unrecognizably small at 100,000X magnification. Optically recognizable SiO_2 inclusions are found in Fe-0.05%Si splats after heat treatment at $1400^\circ C$.

4. The degree of microstructural refinement of the alloys studied is a single valued function of cooling rate over the range of cooling rates studied. For example, SiO_2 inclusion diameters in the Fe-0.05%Si alloy varied from 3 microns at $1^\circ C$/second to 0.1 microns at $1500^\circ C$/second.

5. SiO_2 inclusions in Fe-0.05%Si alloy have no microcracks associated with them in the as cast structure. FeO inclusions in Fe-0.07%O alloy show, in the as cast structure, (a) inclusion-matrix interface separation, (b) fracture of FeO inclusions, and (c) cavities within the inclusions. The voids associated with the FeO inclusions result from the volume changes of the inclusion and matrix during and after solidification.

6. Nearly 100% reduction in area was obtained in test bars of high purity iron, Fe-0.05%Si alloy, and Fe-0.07%O alloy. A dimpled fracture surface is always observed.

7. In the inclusion bearing alloys, one or more inclusions are present in a large fraction of the dimples, and it is concluded that the dimples result from inclusion-matrix interface separation during deformation. Dimples immediately associated with inclusions are smaller the smaller the inclusion. The positions of the inclusions in the dimples of the fracture surface and in the necked region near the fracture surface indicate a rotational deformation mode during necking down.

8. The degree of inclusion-matrix interface separation observed in the polished reduced sections of the test bars of the Fe-0.05%Si master alloy increases with increasing strain.

9. SiO_2 inclusions in the Fe-0.05%Si alloy coarsen measurably in the solid state after 12, 24, and 48 hours at $1400^{\circ}C$ due to Ostwald ripening.

APPENDIX A. CHEMICAL ANALYSES (All Iron Base)

MATERIALS	SiO$_2$	Si	O$_2$	Mn	S	C	P	Ni	Cr	Mo	V	W	Co
Ferrovac "E"		0.01		0.001	0.005	0.003	0.003	0.034	0.01	0.02	0.004	0.02	0.01
Electrolytic Nickel								99.95					
440C Alloy		0.49		0.31		1.04		0.32	17.23	0.47			0.05
4330 Alloy		0.27		0.86		0.31		1.83	0.95	0.44	0.08		
Fe-4.3%C "C" Alloy						4.3							
Fe-0.05%Si	0.034	0.012											
Fe-0.07%O			0.037										
Fe-Mn-S Alloy			0.0059	2.07	1.22	0.077							
Fe-25%Ni High Purity								25.0					
Fe-25%Ni- 0.05%Si	0.014	0.008						26.1					

APPENDIX B.   COOLING RATES DURING LIQUID QUENCHING

Newton's Law of cooling for a spherical droplet with "h controlled" heat transfer is written:

$$h \, A \, (T - T_o) = C_p \, d \, V \, dT/dt \qquad (1)$$

where T_o = quenching medium temperature

T = quenching temperature

A = area of the specimen quenched

V = volume of the specimen quenched

d = density of the specimen quenched

C_p = specific heat of the specimen quenched

h = heat transfer coefficient

dT/dt = cooling rate at temperature T

Using the above expression, a value for the heat transfer coefficient during quenching into a liquid may be calculated from the measured cooling rates of Bigot and Faivre[1] . Using an oscilloscope to record the output of a thermocouple embedded in a cylindrical nickel quenching specimen, they measured a maximum cooling rate in the high temperature range (800° - 600°C) of 50°C/sec. during quenching from 800°C into oil. Since 800°C is above the decomposition temperature of quenching oil, no difference in the heat transfer coefficient is expected for quenching from 800°C (Bigot and Faivre) and quenching from 1550°C (this work).

Using expression 1 for Bigot and Faivre's work results in a calculated value of h of 0.00885 cal./cm^2sec. $^{\circ}$C. For a one gram spherical charge of iron in the levitation furnace quenched into oil

from 1550°C:

$$hd/k = 0.0025$$

where d = quenching specimen diameter

k = quenching specimen thermal conductivity.

Therefore, the heat transfer in liquid quenching is "h controlled", since hd/k is much less than one. Again using the calculated value of the heat transfer coefficient and expression 1 for oil quenching of a spherical one gram levitation melted iron charge quenched from 1550°C, a cooling rate of 140°C/sec. is calculated.

REFERENCE

1. R. Bigot and R. Faivre, "Application de l'oscillographe cathodique a l'enregistrement des courbes temperature-temps au cours de la trempe rapide des metaux", Revue de Metallurgie, LIII, No. 2, 1956, pp. 131-138.

APPENDIX C

Bergh and Lindberg[23] have devised a method for converting a measured apparent sphere diameter size distribution on a polished surface to the true size distribution. The probability that a sphere of given diameter will appear as a circle of a given diameter on the plane of polish is calculated for various sphere and circle sizes. A table is then constructed of these values over the range of the size distribution measured. It is then assumed that the largest circle on the plane of polish is very nearly as large as the diameter of the sphere it represents. The number of spheres of this diameter that will appear as this and smaller diameter circles is then calculated from the probability table and subtracted from the measured values for given circle sizes, giving a corrected number of the smaller sized circles. This process is repeated for each smaller size circle diameter until the entire size distribution is converted. Probability tables and a demonstration of the conversion technique are given in Bergh and Lindberg's article. The true converted size distribution is compared with the measured size distribution of FeO inclusions in Figure C-1 for the Fe-0.07%C master alloy.
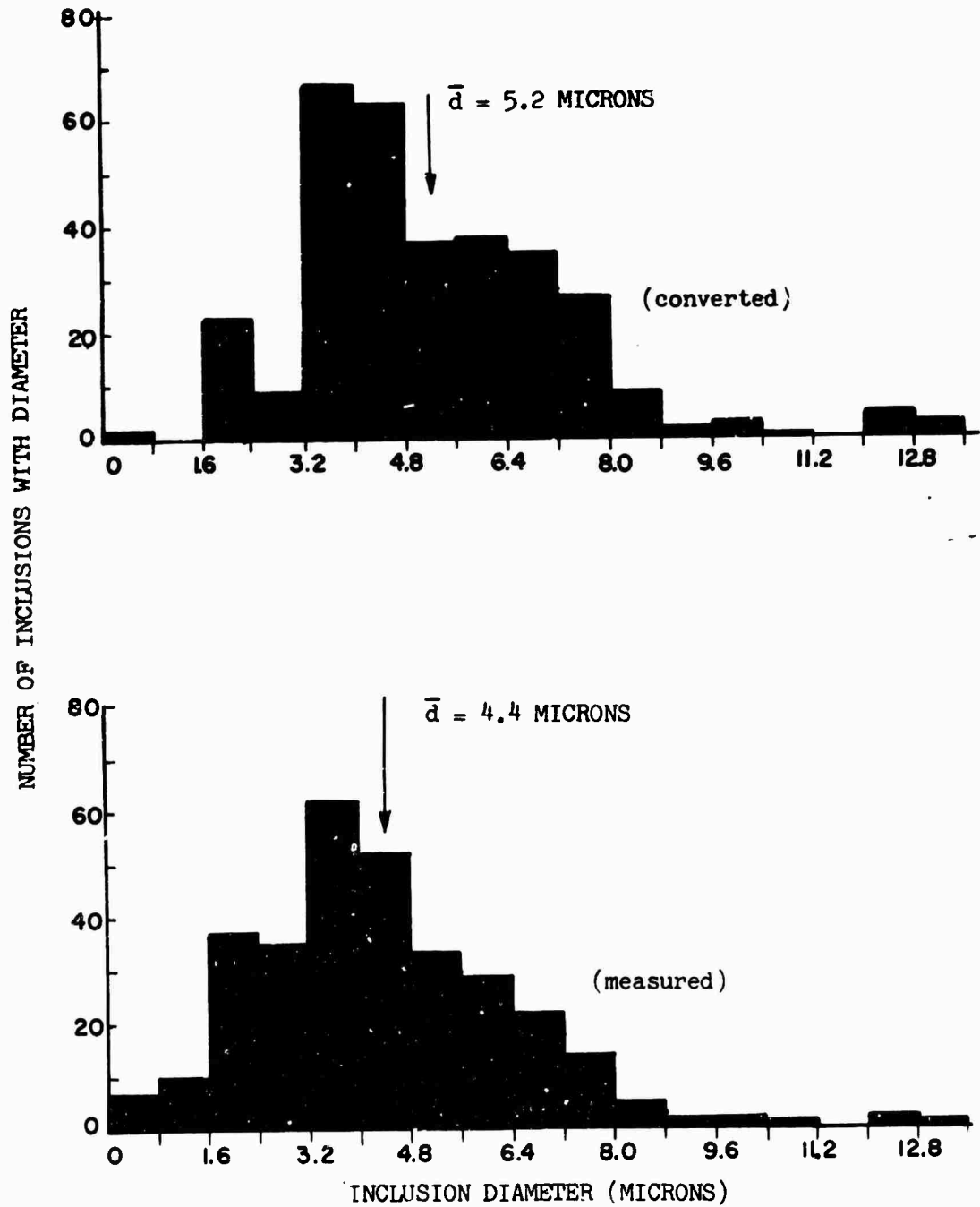
Figure C-1. Size distribution conversion for FeO inclusions in
Fe-0.07%O master alloy.
Top: Three dimensional converted size distribution.
Bottom: Measured planer size distribution.

APPENDIX D. MECHANICAL PROPERTIES

Small flat 1/2 inch gage length by approximately 1/8 inch
thick tensile bars were machined from the master alloys in the vacuum
induction furnace. Tensile testing was carried out on an Instron
machine at 0.05 inches/minute strain rate using a 1/2 inch gage length
extensometer. Results of the tension tests are shown in Table D-1.
The base material, Ferrovac "E", was tested in the as received condition.
Comparisons were made with the measured properties of Ferrovac "E"
iron: 36,500 psi yield strength, 44,500 psi ultimate, and 26.2%
elongation for 1/2 inch gage length bars. The results of the tension
tests on the 1/2 inch gage length test bars of the Fe-0.05%Si alloy,
mean SiO_2 diameter = 3.4 , indicate the presence of SiO_2 inclusions
slightly lowers the strength and the ductility of the iron. Similarly
for the Fe-0.07%O master alloy, mean FeO diameter = 5.4 , the strength
is lowered, and the ductility is reduced. Since reduction in area in
most cases is 100% (necking to a point), this parameter was not considered
meaningful.

Observations on the scanning electron microscope of the as cast
inclusion bearing master alloys indicate that microcracks associated with
the FeO inclusions in the Fe-0.07%O alloy may cause poorer ductility as
compared to the Fe-0.05%Si alloy, where no microcracks are associated with
the SiO_2 inclusions in the as cast microstructure. Although the results
of the properties measurements on the two alloys are not directly comparable
due to the substantial difference in yield strengths, one would expect
somewhat lower ductility for the FeO inclusion bearing alloy as compared
to the SiO_2 inclusion bearing alloy, as was observed.

TABLE D-1

MECHANICAL PROPERTY DATA

(1/2" Gage Length Test Bars)

TEST BAR	YIELD STRENGTH (psi)	ULTIMATE TENSILE STRENGTH (psi)	ELONGATION IN 1/2" (%)	CONDITIONS OF TEST
Ferrovac "E"	40,300	48,700	24.5	To Fracture
" "	33,200	40,200	28.0	"
SiO_2 Master	24,400	27,600	25.3	"
"	26,300	30,300	22.8	"
"	20,700	24,000		To Necking
"	24,000			To 0.5% e
"	19,600			To 5.0% e
FeO Master	34,900	44,300	10.0	To Fracture
"	30,600	38,200	13.0	"

DOCUMENT CONTROL DATA · R&D

(Security classification of title, body of abstract and indexing annotation must be entered when the overall report is classified)

1. ORIGINATING ACTIVITY (Corporate author)	2a. REPORT SECURITY CLASSIFICATION
Massachusetts Institute of Technology Cambridge, Massachusetts 02139	Unclassified
	2b. GROUP

3. REPORT TITLE

SOLIDIFICATION OF IRON BASE ALLOYS AT LARGE DEGREES OF UNDERCOOLING

4. DESCRIPTIVE NOTES (Type of report and inclusive dates)

Interim Report January 1968 - January 1969

5. AUTHOR(S) (Last name, first name, initial)

Brower, W. E. Jr. and Flemings, M. C.

6. REPORT DATE	7a. TOTAL NO. OF PAGES	7b. NO. OF REFS
July 15, 1969	100	41

8a. CONTRACT OR GRANT NO. DA-46-68-C-0044	9a. ORIGINATOR'S REPORT NUMBER(S)
b. PROJECT NO. D/A 1C02401A328	AMMRC CR 69-14/1
c. A,C,S Code No. 5025.11.294	9b. OTHER REPORT NO(S) (Any other numbers that may be assigned this report)
d.	

10. AVAILABILITY/LIMITATION NOTICES

This document has been approved for public release and sale; its distribution is unlimited.

11. SUPPLEMENTARY NOTES	12. SPONSORING MILITARY ACTIVITY
	U. S. Army Materials and Mechanics Center Watertown, Massachusetts 02172

13. ABSTRACT

A levitation melting and splat cooling apparatus modified to permit chill casting and liquid quenching was utilized to investigate the effect of increased cooling rate on solidification structure and mechanical behavior. The degree of microstructural refinement of dendrites, inclusions, and lamellar eutectic with increased cooling rate was determined quantitatively and qualitatively over the range of cooling rates available, 1°C/second to 10^6°C/second for several iron base alloys. SiO_2 inclusions in Fe-0.05% Si alloy were observed to be measurably coarsened after isothermal solid state heat treatment at 1400°C. The fracture behavior of inclusion bearing pure iron, in one alloy containing SiO_2 inclusions, and in the other alloy containing FeO inclusions, was investigated for various size ranges of inclusions by means of the scanning electron microscope. For both inclusion bearing alloys, the ductile fracture surface revealed dimples containing spherical inclusions. Extreme inclusion-matrix interface separation giving a "ball in a trough" appearance resulted from a rotational deformation mode during necking down of the test bar. Dimples immediately associated with the inclusions were smaller the smaller the inclusion. Although the fracture surfaces of the two alloys were similar, microcracks associated with FeO inclusions in the Fe-0.07% O alloy were observed in the as-cast structure, while no microcracks associated with the SiO_2 inclusions in the Fe-0.05% Si alloy were observed in the as-cast structure.

(Authors)

DD ᶠᵒʳᵐ **1473** ₁ ⱼₐₙ ₆₄

14. KEY WORDS	LINK A		LINK B		LINK C	
	ROLE	WT	ROLE	WT	ROLE	WT
Undercooling						
Splat Cooling						
Inclusions						
Solidification						
Fracture						
Steel						

INSTRUCTIONS

1. ORIGINATING ACTIVITY: Enter the name and address of the contractor, subcontractor, grantee, Department of Defense activity or other organization (corporate author) issuing the report.

2a. REPORT SECURITY CLASSIFICATION: Enter the overall security classification of the report. Indicate whether "Restricted Data" is included. Marking is to be in accordance with appropriate security regulations.

2b. GROUP: Automatic downgrading is specified in DoD Directive 5200.10 and Armed Forces Industrial Manual. Enter the group number. Also, when applicable, show that optional markings have been used for Group 3 and Group 4 as authorized.

3. REPORT TITLE: Enter the complete report title in all capital letters. Titles in all cases should be unclassified. If a meaningful title cannot be selected without classification, show title classification in all capitals in parenthesis immediately following the title.

4. DESCRIPTIVE NOTES: If appropriate, enter the type of report, e.g., interim, progress, summary, annual, or final. Give the inclusive dates when a specific reporting period is covered.

5. AUTHOR(S): Enter the name(s) of author(s) as shown on or in the report. Enter last name, first name, middle initial. If military, show rank and branch of service. The name of the principal author is an absolute minimum requirement.

6. REPORT DATE: Enter the date of the report as day, month, year; or month, year. If more than one date appears on the report, use date of publication.

7a. TOTAL NUMBER OF PAGES: The total page count should follow normal pagination procedures, i.e., enter the number of pages containing information.

7b. NUMBER OF REFERENCES: Enter the total number of references cited in the report.

8a. CONTRACT OR GRANT NUMBER: If appropriate, enter the applicable number of the contract or grant under which the report was written.

8b, 8c, & 8d. PROJECT NUMBER: Enter the appropriate military department identification, such as project number, subproject number, system numbers, task number, etc.

9a. ORIGINATOR'S REPORT NUMBER(S): Enter the official report number by which the document will be identified and controlled by the originating activity. This number must be unique to this report.

9b. OTHER REPORT NUMBER(S): If the report has been assigned any other report numbers (either by the originator or by the sponsor), also enter this number(s).

10. AVAILABILITY/LIMITATION NOTICES: Enter any limitations on further dissemination of the report, other than those imposed by security classification, using standard statements such as:

  (1) "Qualified requesters may obtain copies of this report from DDC."

  (2) "Foreign announcement and dissemination of this report by DDC is not authorized."

  (3) "U. S. Government agencies may obtain copies of this report directly from DDC. Other qualified DDC users shall request through

  _____."

  (4) "U. S. military agencies may obtain copies of this report directly from DDC. Other qualified users shall request through

  _____."

  (5) "All distribution of this report is controlled. Qualified DDC users shall request through

  _____."

If the report has been furnished to the Office of Technical Services, Department of Commerce, for sale to the public, indicate this fact and enter the price, if known.

11. SUPPLEMENTARY NOTES: Use for additional explanatory notes.

12. SPONSORING MILITARY ACTIVITY: Enter the name of the departmental project office or laboratory sponsoring (paying for) the research and development. Include address.

13. ABSTRACT: Enter an abstract giving a brief and factual summary of the document indicative of the report, even though it may also appear elsewhere in the body of the technical report. If additional space is required, a continuation sheet shall be attached.

It is highly desirable that the abstract of classified reports be unclassified. Each paragraph of the abstract shall end with an indication of the military security classification of the information in the paragraph, represented as (TS), (S), (C), or (U).

There is no limitation on the length of the abstract. However, the suggested length is from 150 to 225 words.

14. KEY WORDS: Key words are technically meaningful terms or short phrases that characterize a report and may be used as index entries for cataloging the report. Key words must be selected so that no security classification is required. Identifiers, such as equipment model designation, trade name, military project code name, geographic location, may be used as key words but will be followed by an indication of technical context. The assignment of links, rules, and weights is optional.